POLITECNICO DI MILANO

Facoltà di Ingegneria Industriale e dell'Informazione

Corso di Laurea Magistrale in
Ingegneria Energetica

POLITECNICO
MILANO 1863

Hierarchical titanium-nitride scaffolds for Direct Methanol Fuel Cell anodes

Relatore: Andrea Casalegno
Correlatori: Fabio di Fonzo
Andrea Perego

Tesi di laurea di
Giorgio Giuffredi
Matricola 820084

Anno Accademico 2015/2016

Ringraziamenti

Dopo il tanto tempo trascorso in questa università, mentre sto per chiudere questo percorso con un classico “That’s all, folks!”, è il momento di ringraziare e rendere onore a tutte le persone che mi hanno aiutato, in un modo o nell’altro, ad arrivare fin qui.

Grazie innanzitutto ai miei genitori, che hanno sempre creduto in me, anche quando non ci credevo più io. Una dedica non basta a rendere l’idea di quello che hanno fatto per il loro unicogenito.
Grazie alla mia famiglia, che non ha mai fatto mancare supporto, affetto e orgoglio per me.

Grazie ad Andrea Casalegno e a Fabio di Fonzo, per avermi dato la possibilità di lavorare a questa tesi.

Grazie ai tre moschettieri Gian Maria, Mattia e Patrick per tutti i momenti – belli, brutti, imbarazzanti, disagevoli e meravigliosamente assurdi – passati insieme. Grazie ai Guglielmo Bros (uno Jaeger è per sempre) e a Giulia – 13 anni e ancora si spettegola e si esporta aristocratico disprezzo come il primo giorno.

Grazie a Pietro e Matsor, avete reso Milano è più bella. Tranne quando bisogna connettersi a Rift.
E grazie a Feffa, a Valla e a Claudia, le “mie donne”: mi avete sempre supportato e ci siete sempre state per me, da voi ho lasciato un pezzo di cuore. Vi voglio bene.

Grazie a Mauro, Manfredi, Martina, Marie, Frigo, Elena, Clelia e tutti i nerdsailors (siete troppi), per avermi aperto un modo. Vi sarò sempre grato.

Grazie a Albi, Peppe, Fabri, Marco, Giulio, Stefanone, Flavio e Sandro, immortali e disperati compagni in questi anni al Politecnico.

Grazie a Mez, Eugenio, Patateo, Ciccio, Andrea (che si becca anche un bonus per l’aiuto insostituibile che mi ha sempre dato), Dario, Francesco e Giorgio, e ai compagni del CNST per avermi accolto, sopportato, svezzato e per aver reso fenomenali – nonostante gli alti e bassi – i mesi in laboratorio.

If friends come and go like the waves of the ocean, I hope you all stay like an octopus on my face.

Riassunto Esteso

Il maggior problema che ostacola la diffusione delle celle a combustibile a metanolo (Direct Methanol Fuel Cells, DMFC) è l'elevato costo del catalizzatore a base platino/rutenio. Per questo motivo, la ricerca è focalizzata sulla riduzione del carico catalitico totale, in modo da abbattere i costi. Ad oggi, il carbonio mesoporoso rappresenta lo stato dell'arte per quanto riguarda i supporti catalitici per DMFC: presenta alta conduttività elettrica, ma soffre di problemi di stabilità, specialmente quando soggetto a funzionamento per lungo periodo. Come è mostrato in diversi studi, il nitruro di titanio (TiN) ha una conduttività comparabile ai metalli e, insieme, un'eccezionale stabilità chimica, rendendolo un possibile candidato per sostituire il carbonio.

Questo lavoro di tesi è focalizzato sulla fabbricazione di un catalizzatore di platino per DMFC, supportato su nanostrutture *self-assembled*, gerarchiche e mesoporose di nitruro di titanio, depositate tramite *Pulsed Laser Deposition* (PLD). L'obiettivo della tesi è creare un *proof of concept* di tale catalizzatore, in modo da gettare le basi per uno studio fisico ed elettrochimico sistematico ed estensivo di questo materiale, affinché in futuro il nitruro di titanio possa sostituire il carbonio come supporto per DMFC sia all'anodo che al catodo, grazie rispettivamente alla sua capacità di oxofilia e – se drogato – di fotogenerare corrente per migliorare l'efficienza dell'ossidazione del metanolo, e alla sua migliore stabilità chimica.

Il lavoro è quindi strutturato in tre parti: fabbricazione tramite PLD, ottimizzazione e caratterizzazione del supporto di TiN, implementazione ed ottimizzazione di un metodo efficiente per la deposizione del catalizzatore di Pt sulla nanostruttura, e infine test e analisi della stabilità dell'insieme supporto + catalizzatore ottenuto.

L'obiettivo finale che si vuole raggiungere durante la fase di fabbricazione e caratterizzazione del supporto in TiN è trovare delle condizioni di deposizione che garantiscano due caratteristiche:

- Elevata area superficiale e alta porosità: si vuole massimizzare il contatto tra supporto ed elettrolita, in modo che la successiva deposizione del catalizzatore di Pt sia più efficace. In altre parole, si vuole ottenere una dispersione omogenea del catalizzatore sul supporto, per ottenere un'elevata area catalitica attiva (ECSA, Electro-Chemical Surface Area);
- Buona stabilità meccanica e chimica: si vuole ottenere un film stabile in ambiente acido su un ampio intervallo di potenziale, e che abbia una resistenza meccanica alla manipolazione accettabile.

Per trovare le condizioni di deposizioni che soddisfino i due requisiti, viene condotto uno scan di varie pressioni di deposizione; è anche indagata l'influenza di trattamenti termici sulle proprietà fisiche del supporto. I film sono cotti a 500°C per 4 ore in vuoto, per innescare la cristallizzazione del TiN (inizialmente amorfo), e si confrontano qualitativamente – tramite analisi SEM – i cambiamenti nella morfologia della nanostruttura.

I risultati ottenuti in questa fase sono i seguenti:

- La cottura dei film innesca la cristallizzazione del materiale, con un cambiamento nella struttura e un aumento medio di porosità: il trattamento termico, infatti, fa sì che la struttura amorfa del film depositato si addensi, incrementando porosità e area superficiale e al contempo la resistenza meccanica del materiale. Questo trend è osservato per tutti i film depositati e analizzati;
- I supporti di TiN depositati a 30 Pa e 40 Pa N_2 hanno buona stabilità meccanica ma sono troppo compatti: questa caratteristica è un problema, perché rende difficoltoso il trasporto dei reagenti ai siti catalitici, rendendolo un supporto catalitico inefficiente;
- Il supporto depositato a 80 Pa N_2 presenta elevata area superficiale e ottima porosità, tuttavia la resistenza meccanica è minima e il film si delamina quando viene manipolato;
- I film depositati a 50 Pa e 60 Pa N_2 soddisfano entrambe le condizioni: hanno buona resistenza meccanica e presentano nanostrutture molto porose. Inoltre hanno un rapporto lunghezza/spessore favorevole, pari a circa 7, che consente di approssimarle a strutture quasi 1D. Sulla base di questa considerazione, questi due film vengono studiati più approfonditamente a livello fisico ed elettrochimico.

L'analisi fisica dei supporti di TiN depositati a 50 e 60 Pa si rivela inconcludente per via di un difetto legato alla fabbricazione: una disuniformità nello spot del laser, unita ai contaminanti presenti nel target di TiN e nel gas di processo, fa sì che si depositino sul film dei cluster di ossido di titanio cristallini che non permettono l'analisi del supporto tramite XRD e Raman e che diminuiscono l'area superficiale del film. L'analisi elettrochimica dei supporti è condotta tramite voltammetria ciclica in 0.5 M H_2SO_4 e porta a due conclusioni:

- I film *as deposited* non sono stabili in condizioni acide: all'aumentare degli scan di potenziali la corrente registrata diminuisce, inoltre a bassi potenziali avviene una reazione con l'idrogeno presente nell'elettrolita che modifica la composizione del film di TiN e ne va a diminuire la conduttività ad alti potenziali. Per questo fenomeno sono avanzate tre ipotesi: idrurazione del titanio e formazione di idruro, formazione di idrossido di titanio, oppure effetto elettro-cromico con de-intercalazione irreversibile degli ioni di idrogeno. Data tale instabilità, è impossibile implementarli come supporti per catalizzatore in una cella a combustibile.
- I film *annealed* sono invece stabili quando testati elettrochimicamente, con un comportamento simile a quello di un condensatore con alta carica di *double-layer* ed elevata resistenza chimica anche ad alti potenziali, che li rende interessanti anche per future applicazioni come catodo di fuel cell. Durante il trattamento termico, tuttavia, viene introdotta una contaminazione indesiderata di carbonio, parzialmente responsabile del comportamento da condensatore.

Un test elettrochimico finale effettuato con elettrolita contenente metanolo conferma le due considerazioni precedenti, e mostra come il supporto di TiN sia inattivo verso l'ossidazione del metanolo. La conclusione di questa fase è che i film *annealed* di TiN depositati a 50 e 60 Pa saranno usati come supporto per la deposizione del catalizzatore di platino.

La funzionalizzazione del supporto di TiN avviene tramite elettrodeposizione del catalizzatore di platino, dopo un primo tentativo fallito di *sputtering* di una lega di platino e rutenio. Il processo di elettrodeposizione si basa su un metodo galvanostatico – che impiega impulsi di corrente – trovato in letteratura, da ottimizzare per la nanostruttura sviluppata. Dopo le prove preliminari per dimostrare la replicabilità del processo indicato, l'implementazione dell'elettrodeposizione si snoda attraverso i seguenti passi:

- Ottimizzazione della carica totale – cioè, della massa di catalizzatore – depositata sul supporto: si vuole massimizzare l'ECSA e al contempo mantenere un carico catalitico paragonabile con lo stato dell'arte, che non superi gli 0,3-0,4 mg/cm^2. Il risultato di questo passo d'ottimizzazione è che 32 C/cm^2 è la carica che garantisce l'ECSA migliore, perché oltre si ha un effetto di saturazione del supporto, a causa del quale le particelle di platino si agglomerano e diminuiscono la propria area superficiale.
- Dopo aver determinato con precisione l'efficienza faraidica dell'elettrodeposizione – per legare alla carica trasferita durante il processo l'effettiva massa di platino depositata – si indaga l'influenza della pressione con cui il supporto è stato depositato sull'ECSA totale. Per questo, a pari massa di platino, il supporto di TiN depositato a 50 Pa viene confrontato con quello depositato a 60 Pa. Il risultato è che aumentare la pressione del supporto da 50 a 60 Pa porta a un'ECSA maggiore: in questo caso l'area attiva è più del doppio (da 2,5 m^2/g$_{Pt}$ a 6 m^2/g$_{Pt}$), fenomeno spiegato dalla maggior porosità del TiN 60 Pa e dalla presenza, per il TiN 50 Pa, di un picco in ossidazione che nasconde la vera corrente di double layer e che riduce l'ECSA effettiva.
- Infine, si ottimizza la durata dell'impulso di corrente: poiché questo parametro è legato al diametro medio delle nanoparticelle depositate, si vuole investigare l'influenza che questo ha sull'ECSA del catalizzatore. Due diverse durate d'impulso (50 ms e 100 ms) sono testate, e l'ECSA dei catalizzatori viene confrontata: sebbene i due valori numerici siano molto simili, pari a circa 6 m^2/g$_{Pt}$, l'impulso di 50 ms garantisce un valore di ECSA mediamente maggiore e per questo viene scelto all'interno della ricetta definitiva per l'elettrodeposizione del platino.

Ottimizzato sia il supporto che il metodo di deposizione del catalizzatore, il materiale è testato elettrochimicamente in 0.5 M H_2SO_4 e in 0.5 M H_2SO_4 + 1 M CH_3OH per valutare la sua area attiva, la sua performance rispetto l'ossidazione del metanolo, e come il testing elettrochimico influenzi le prestazioni del materiale.

Il catalizzatore in condizioni pristine presenta un'ECSA migliore dei precedenti, pari a circa 11 m^2/g$_{Pt}$, e un'ottima attività verso l'ossidazione del metanolo: considerando i parametri di confronto scelti, cioè il ΔE tra il picco d'ossidazione nello scan d'andata e quello nello scan di ritorno – legato alla cinetica del catalizzatore, si vuole sia il più basso possibile – e l'I_{ratio}, cioè il rapporto tra i due picchi di ossidazione – legato alla capacità di eliminare gli intermedi di reazione, si vuole il più alto possibile – il catalizzatore ha dei valori, rispettivamente, di 145 mV e ∼2,2, che superano quelli di un catalizzatore Pt/C – per il quale i due parametri valgono 200 mV e 1,04.

Dopo la prova in metanolo, il catalizzatore viene nuovamente testato per capire come gli scan precedenti influenzino l'ECSA: si dimostra che il materiale presenta una buona resistenza in ambiente acido e sotto l'azione delle voltammetrie cicliche, poiché la sua ECSA rimane paragonabile alla situazione pristina, pari a circa 14 m^2/g_{Pt}. Questo comportamento è attribuito alla diminuita carica di double layer e alla minor presenza di impurezze nel catalizzatore a seguito degli scan precedenti.

Infine, l'ultimo test sul catalizzatore è effettuato in una soluzione contenente metanolo, per verificare come i test precedenti abbiano modificato le prestazioni del materiale. Si dimostra che, nonostante i numerosi scan, il catalizzatore presenta ancora un'ottima performance verso l'ossidazione del metanolo, con un ΔE pari a 134 mV e un I_{ratio} di 1,71, valori migliori dei catalizzatori Pt/C e di alcuni catalizzatori Pt/TiN trovati in letteratura.

I buoni risultati ottenuti indicano che il catalizzatore presenta una performance degna di nota verso l'ossidazione del metanolo, superando le prestazioni dei catalizzatori di puro Pt e avvicinandosi a quelle dei catalizzatori a base PtRu; da ciò si può ipotizzare che la presenza del TiN renda il catalizzatore più attivo verso l'ossidazione degli intermedi della reazione di elettro-ossidazione del metanolo, rendendo il TiN un plausibile candidato per diminuire il carico catalitico di rutenio e, quindi, diminuire i costi e i problemi a esso legati.

Nonostante questi risultati, vi sono aspetti che richiedono un ulteriore studio e delle criticità da risolvere: innanzitutto, ulteriori studi sono necessari per comprendere il cambio di morfologia delle nanostrutture di TiN durante l'elettrodeposizione e, una volta risolti i problemi legati alla fabbricazione e all'ablazione anomala del target da parte del laser, la precisa composizione fisica e chimica del film stesso. È inoltre necessario eliminare tutte le possibili contaminazioni provocate da agenti esterni (carbonio e, per quanto possibile, ossigeno).

I risultati ottenuti mostrano come la PLD possa essere un metodo efficiente per ottenere catalizzatori per fuel cell, mentre l'unione tra le proprietà fotocatalitiche di nitruro e ossinitruro di titanio e della forma a nanoalberi del supporto, con elevata capacità di *light harvesting*, potrebbe condurre in futuro alla creazione di fotocatalizzatori ad alta efficienza.

Abstract

To overcome the high cost of the catalyst in Direct Methanol Fuel Cell (DMFC) technology, research is moving towards the reduction in the Pt-Ru loading in the electrodes by increasing the electrochemical surface area. To date, the state of the art of catalyst supports is dominated by mesoporous carbon. It shows high conductivity but suffer from stability issues especially on long-term operation. As shown in various works in the literature, titanium nitride (TiN) has a metal-like conductivity with an outstanding chemical stability, making it a possible candidate to replace carbon.

In this work, we report about Pt catalyst supported by self-assembled, hierarchical mesoporous titanium nitride nanostructure, grown by Pulsed Laser Deposition. Platinum nanoparticles are deposited on these tree-like structures by means of pulsed electrodeposition. Electrochemical characterization of such catalysts is performed, showing it is possible to reach high value of the ECSA while controlling the porosity and the morphology of the material down to the nanoscale. Moreover, we show how for MOR, the TiN scaffold could be active towards the removal of contaminants from the platinum surface, suggesting it could be a possible candidate for replacing, or at least reducing the ruthenium content.

Keywords: DMFC, titanium nitride, Methanol Oxidation Reaction, Pulsed Laser Deposition

Sommario

Per superare il problema dell'elevato costo del catalizzatore nelle celle a combustibile a metanolo (Direct Methanol Fuel Cells, DMFC), la ricerca è focalizzata sulla riduzione del carico totale del catalizzatore di platino/rutenio. Ad oggi, il carbonio mesoporoso rappresenta lo stato dell'arte per quanto riguarda i supporti catalitici per DMFC: presenta alta conduttività elettrica, ma soffre di problemi di stabilità, specialmente quando soggetto a funzionamento per lungo periodo. Come è mostrato in diversi studi, il nitruro di titanio (TiN) ha una conduttività comparabile ai metalli e, insieme, un'eccezionale stabilità chimica, rendendolo un possibile candidato per sostituire il carbonio mesoporoso.

In questo lavoro, si presenta un catalizzatore di platino per DMFC supportato su nanostrutture *self-assembled,* gerarchiche e mesoporose di nitruro di titanio, fabbricate tramite *Pulsed Laser Deposition*. Le nanoparticelle di platino sono depositate su queste nanostrutture di forma alberosa con una tecnica di elettrodeposizione pulsata. Il comportamento elettrochimico del catalizzatore è caratterizzato, e viene mostrato come sia possibile raggiungere valori elevati di area catalitica (Electro-Chemical Surface Area, ECSA) e insieme controllare la morfologia e la porosità del materiale fino al nanometro.

Viene inoltre mostrato come per la reazione di elettro-ossidazione del metanolo (Methanol Oxidation Reaction, MOR), il supporto di TiN potrebbe presentare attività nella rimozione di contaminanti dalla superficie del catalizzatore di platino; ciò suggerisce che il TiN potrebbe essere un possibile candidato per rimpiazzare il rutenio, o almeno ridurne il carico catalitico.

Parole chiave: DMFC, nitruro di titanio, elettro-ossidazione del metanolo, Pulsed Laser Deposition

Table of Contents

Ringraziamenti ... 2

Riassunto Esteso ... 3

Abstract ... 7

Sommario ... 8

Table of Contents ... 10

Introduction ... 13

Introduction to Direct Methanol Fuel Cells (DMFCs) Technology, Electrochemistry and Electrode Materials ... 15

1.1. Fuel Cells ... 16

1.2. DMFC ... 17

1.3. Electrochemistry and Kinetics ... 20

1.3.1. Introduction and Overview of Electrode Processes ... 20

1.3.2. Mass-Transfer Controlled Reactions ... 22

1.3.3. Reaction Kinetics & Arrhenius Equation ... 23

1.3.4. Butler-Volmer Equation ... 24

1.3.5. Exchange Current & Approximate Forms of the Butler-Volmer Equation ... 26

1.3.6. Tafel Plots ... 29

1.4. Losses in DMFC ... 29

1.5. Electro-Oxidation of Methanol ... 30

1.6. Carbon-Based Anodic Supports for DMFC ... 31

1.7. Alternative Supports for DMFCs ... 33

1.7.1. Metal-Oxide Based Supports for Low Temperature Fuel Cells ... 33

1.7.2. Titanium Dioxide ... 34

1.7.3. Titanium Nitride ... 36

1.8. Goals of the Work ... 37

Fabrication Systems & Analysis Methods ... 39

2.1. Fabrication & Depositions Methods ... 40

2.1.1. Pulsed Laser Deposition ... 40

2.1.2. The PLD Physical Process ... 41

2.1.3. PLD Application for Support Deposition ... 42

2.1.4. DC Sputtering ... 44

2.1.5. Catalyst Deposition Through D.C. Sputtering ... 45

2.1.6. Electrodeposition ... 46
2.2. Electrochemical Measurements ... 48
2.2.1. Electrochemical Experimental Setup ... 48
2.2.2. Linear Sweep Voltammetry ... 48
2.2.3. Cyclic Voltammetry ... 49
2.2.4. Electro-Chemical Surface Area ... 52
2.3. Crystallography and Raman Spectroscopy ... 53
2.3.1. X-Ray Crystallography ... 53
2.3.2. Raman Spectroscopy ... 55
Fabrication and Characterization of TiN Scaffold ... 57
3.1. TiN Scaffold Fabrication via Pulsed Laser Deposition ... 58
3.2. Process Gas Pressure Scan for TiN Deposition ... 59
3.2.1. As Deposited TiN Films ... 59
3.2.2. Annealed TiN films ... 61
3.3. Physical Characterization of TiN50 and TiN60 ... 63
3.4. Electrochemical Characterization of TiN50 & TiN60 ... 67
3.5. Effect of Electrochemical Testing on TiN Films ... 72
Deposition of Pt Catalyst on TiN Support ... 75
4.1. Electrochemical References ... 76
4.2. TiN/PtRu Multilayer Catalyst ... 77
4.3. Platinum Electrodeposition ... 80
4.4. Platinum Electrodeposition – TiN Stability Evaluation ... 83
4.5. Platinum Electrodeposition – Deposited Charge Optimization ... 85
4.6. Platinum electrodeposition – Faradaic Efficiency Determination ... 91
4.7. Platinum Electrodeposition – Support Optimization ... 92
4.8. Platinum Electrodeposition – Current On-Time Optimization ... 95
Final Testing of the TiN-Supported Pt Catalyst ... 99
5.1. Testing Protocol for the TiN/Pt Catalyst ... 100
5.2. Morphological Analysis of the Pristine Catalyst ... 101
5.3. Electrochemical Characterization of the Pristine Catalyst ... 103
5.4. Morphological Analysis After the First Cycling ... 106
5.5. Stability Analysis for AN-TiN60/Pt32-50 Catalyst ... 107
Conclusions ... 113
Table of figures ... 115

Appendix 118
A.1 - Instruments & Materials 118
A.2 - ECSA Calculation Method 118
A.3 - Lattice Strain Calculation Method 118
Legend and Acronyms 120
References 121

Introduction

Direct methanol fuel cells (DMFCs) are specially optimized polymeric fuel cells that can be fed with liquid methanol, which is oxidized at the anodic side on a platinum-based catalyst, supported on carbon, without any pre-reforming. Employing a liquid fuel feed, DMFCs offer two peculiar features among PEMFCs: the liquid fuel - a mixture of methanol and water - permits a higher energy density than hydrogen, and storage of a liquid fuel is safer than for a gaseous one. This is particularly interesting in integrating DMFCs into portable, lightweight devices. Despite these features, DMFCs suffer from specific and critical disadvantages, apart from the typical PEMFCs drawbacks: high anodic overpotential due to the slow, sluggish kinetic of the methanol oxidation reaction, which reduces the output power and the overall efficiency. Moreover, methanol crossover from anode to cathode causes parasitic cathodic reaction, as well as fuel waste. At last, higher degradation rate of the cathode is caused by the migration of Ru-catalyst particles from the anode side, leading to a less efficient operation. These drawbacks lead to a high specific cost (in €/kW) for the energy produced by a DMFC, which hinders its large-scale diffusion.

The scope of the work is to fabricate and characterize a novel anode catalyst for methanol oxidation. Such a catalyst should achieve performances comparable, if not superior, to the state of the art electrodes, in terms of platinum dispersion and utilization, low metal loading and stability. To obtain these results, a novel TiN nanostructured scaffold is considered, since the material's hybrid metal/ceramic nature allows a good chemical stability while maintaining a metal-like conductivity.

Catalysts will be fabricated by a PVD-based technology, namely (Pulsed Laser Deposition PLD) in order to control the morphology and the porosity of the thin film at the nanoscale. Metal loading will be implemented by either DC sputtering and pulsed electrodeposition, in order to compare the two methods and optimize a solid and efficient deposition method for the application. Characterization will evaluate both the physical aspects, using XRD, SEM and Raman techniques, and electrochemical aspects with voltammeric analysis in a three electrode cell configuration.

The present work has been carried out using Istituto Italiano di Tecnologia, Center for Nano Science and Technology@Polimi facilities for the fabrication, physical and electrochemical characterizations of the samples.

The work is articulated into five chapters, shown here below:

Ch.1: Introduction to electrochemistry, overview of DMFC support materials and of the problems affecting the technology, literature review of catalytic supports for DMFCs, and definition of the scope of this thesis work.

Ch.2: Description of the deposition methods employed for the fabrication of the TiN/Pt catalyst (PLD, DC Sputtering, electrodeposition) and of the electrochemical (CV, LSV) and physical (XRD, SEM, Raman) analysis procedures.

Ch.3: Fabrication of the TiN nanostructured scaffold, optimization of the process gas pressure during PLD, and electrochemical and physical characterization of the chosen TiN supports.

Ch.4: Deposition of the metal catalyst by DC sputtering, implementation of a pulsed electrodeposition technique for fabricating the Pt catalyst to obtain a working TiN/Pt catalyst, and optimization of the fabrication system to maximize the activity of the catalyst.

Ch.5: Electrochemical and physical characterization of the TiN/Pt catalyst and evaluation of its activity and MOR performance, assessment of the effect of extensive cyclic voltammetry testing on its stability, and comparison to reference catalysts for DMFCs.

Chapter 1

Introduction to Direct Methanol Fuel Cells (DMFCs) Technology, Electrochemistry and Electrode Materials

1.1. Fuel Cells

Fuel cells are devices that convert chemical energy in fuels directly into electrical energy, through oxidation-reduction electrochemical reactions. Since the chemical energy/electrical energy conversion is direct, without losses due to combustion, these devices can obtain higher efficiencies than traditional thermodynamic cycles. In particular, they are not bound to the maximum efficiency that heat engines can achieve, i.e. the Carnot efficiency.

$$\eta_{Carnot} = 1 - \frac{T_C}{T_H} \tag{1.1}$$

In addition, because combustion is avoided during their operation, fuel cells produce electrical energy with minimal, negligible amount of pollutants compared with traditional technologies. Thanks to these features, fuel cells are extensively studied.

Fuel cells are classified according to the operating temperature and choice of the electrolyte. PEMFCs (*Polymer Electrolyte Membrane Fuel Cells*) are the most diffused and most studied low temperature fuel cells; their distinguishing feature is the use of a proton conductive polymeric membrane as electrolyte.

In the figure below, a diagram of a PEMFC is presented:

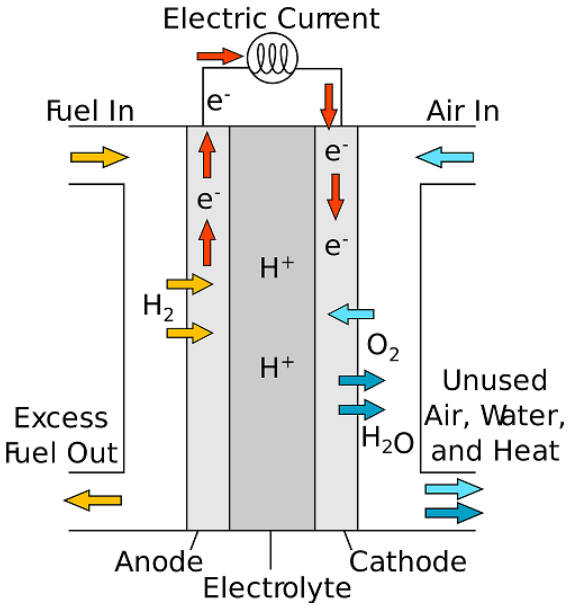

Figure 1: Schematics of a PEMFC

In fuel cells' electrodes, hydrogen combustion is split into two electrochemical redox rections. The electron exchange through the external circuit produces a net current, and therefore electrical power.

PEMFCs have many interesting characteristics that make them an attractive device for energy production, in particular for mobile and portable applications:

- High efficiency, high power density and flexibility;
- Low emissions, low operating temperature and fast start-up;
- Quick response to load variations.

Despite these advantages, PEMFCs suffer from important technical and economical issues that limit their large-scale diffusion:

- Material costs for PEMFCs are high, in particular the platinum-based catalyst, which is necessary due to the low operating temperature. This factor limits the utilization of PEMFC to application niches, because due to these high costs fuel cells aren't as advantageous as traditional technologies for widespread applications;
- The platinum-based catalyst suffers from CO poisoning: if carbon monoxide concentration is more than 20 ppm it's able to inhibit the catalytic activity of platinum;
- PEMFC suffer from severe material degradation, due to the instability of the platinum/carbon based catalysts in the harsh environments found in the electrodes;
- Water management is another serious issue: to guarantee good protonic conductivity the membrane needs to be wet; therefore, reactants need to be humidified. This leads to the concrete possibility of flooding or condensation;
- Operating at atmospheric pressure, operating temperature must be below water evaporation temperature. This leads to the need of a complex cooling system and to a useless waste heat, that is its temperature is too low to be efficiently recycled.

1.2. DMFC

Among PEMFCs, there are specially optimized cells that can be fed with methanol: they are called DMFCs (*Direct Methanol Fuel Cells*) and they can conceptually lead to a promising and efficient energy device for portable applications. Apart from the typical PEMFC advantages, DMFC offer two peculiar features: they are fed with a liquid fuel – a mix of methanol and water – that permits a higher energy density than hydrogen, up to 230%. Being fed with a liquid fuel, DMFC can achieve good performances even without the need for humidification.

	p [bar]	T [°C]	LHV [kWh/l]
H_2	1	25	0,003
H_2	200	25	0,542
H_2	700	25	1,897
CH_3OH	1	25	4,333

Table 1: Specific energy comparison for methanol and hydrogen

Furthermore, storage for a liquid fuel is safer than for a gaseous, highly-pressurized one like hydrogen.

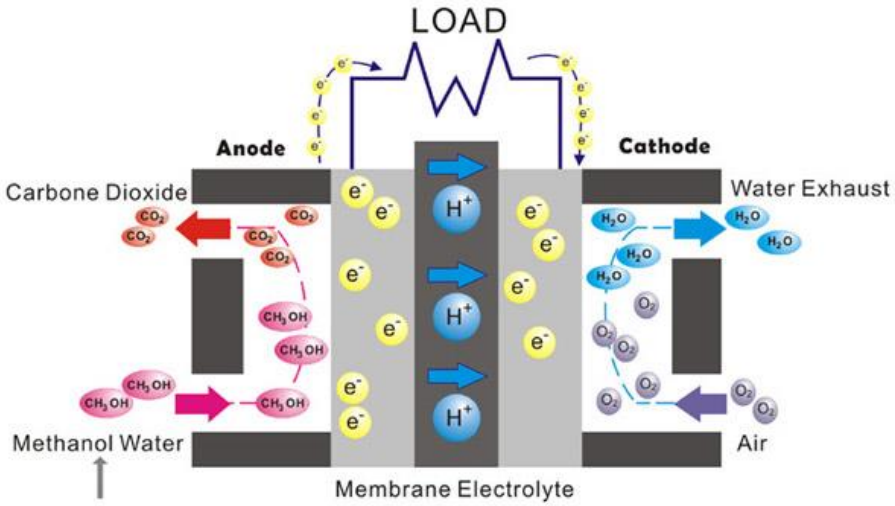

Figure 2: Schematics of a DMFC

However, DMFCs suffer not only from the typical PEMFCs problems, but also from other disadvantages:

- Voltage – and therefore power and efficiency – losses at the anode (**anodic overpotential**) caused by the slow, sluggish kinetic of the methanol oxidation reaction;
- Voltage losses at the cathode (**cathodic overpotential**) due to the high methanol crossover through the polymeric electrolyte membrane. Methanol is affine to water – and therefore to the Nafion membrane – and migrates through the electrolyte to the cathode, where it is oxidized by air. This phenomenon generates at the cathodic side a mixed potential, an average between the oxygen reduction reaction potential and the methanol combustion potential;
- **Severe CO poisoning**: one of the intermediate products of the methanol oxidation reaction is carbon monoxide, which poisons the platinum catalyst. Consequently, in order to limit the voltage losses, a high platinum load, almost ten times higher than hydrogen PEMFCs, is necessary, while a bimetallic catalyst – often a platinum-ruthenium one – is needed to slow down the poisoning process.

Because of these issues, DMFC achieve lower power density and maximum efficiency than PEMFC, as is shown in figure 3.

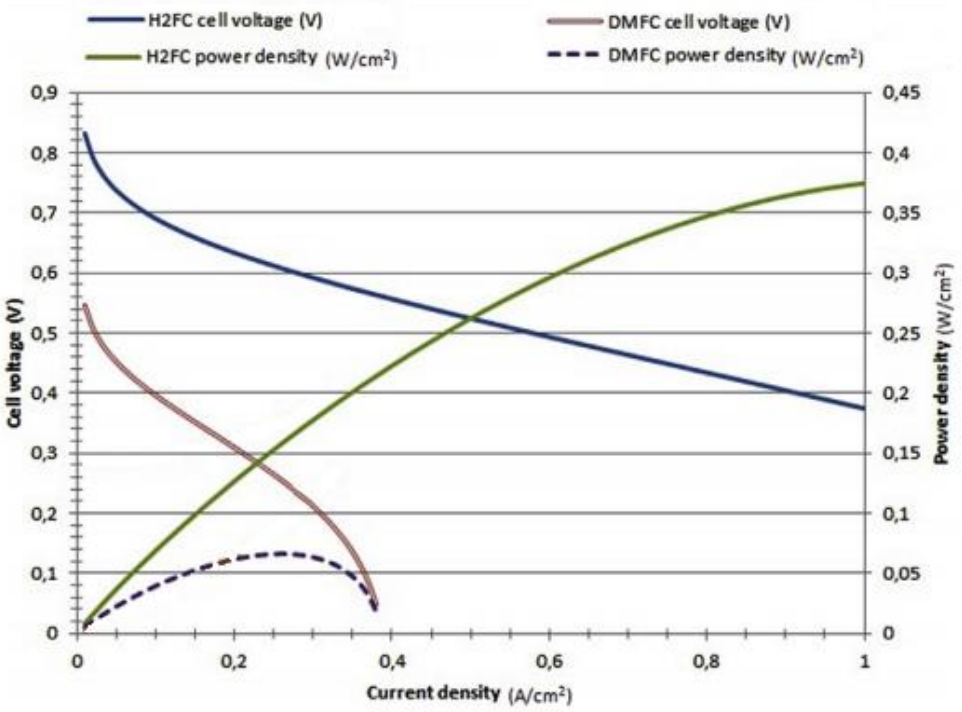

Figure 3: PEMFC and DMFC polarization & power density curves. Modified image. Original from [1]

The two redox reactions that take place at the DMFC electrodes are:

$$CH_3OH + H_2O \rightarrow CO_2 + 6H^+ + 6e^- \qquad E_0 = 0{,}046\,V \; - anodic\; reaction \qquad (1.2)$$

$$6H^+ + 6e^- + \frac{3}{2}O_2 \rightarrow 3H_2O \qquad E_0 = 1{,}23\,V \; - cathodic\; reaction \qquad (1.3)$$

Adding up the two half-reactions leads to the overall reaction that takes place in the cell:

$$CH_3OH + \frac{3}{2}O_2 \rightarrow CO_2 + 3H_2O \quad E_0 = 1{,}18\,V \qquad (1.4)$$

Where E_0 is the standard, thermodynamic cell potential.

It is known that the maximum electrical work that can be done through an electrochemical reaction is:

$$\Delta G = -nFE \qquad (1.5)$$

Where ΔG is the Gibbs free energy of the electrochemical reaction, which for a general reaction A → B is obtained by the following equation:

$$\Delta G = \Delta G^0 + RT \ln \frac{[B]}{[A]} \qquad (1.6)$$

In equation (1.6) ΔG_0 represents the standard free energy, [B] the activity of the product B and [A] the activity of the reactant A at equilibrium. The cell potential is obtained through the following equation:

$$E = E^0 + \frac{RT}{nF} \ln \frac{[B]}{[A]} \tag{1.7}$$

Which is known as Nernst equation.

It is usually more convenient to deal with activities than activities, since the latter are usually unknown. To deal with this problem, we introduce the *formal potential* E_0': it is the measured potential of the electrode when the concentrations of oxidized and reduced species are such that the ratio $C_{Ox}^{\nu_{Ox}} / C_{Red}^{\nu_{Red}}$ is unity.

1.3. Electrochemistry and Kinetics

1.3.1. Introduction and Overview of Electrode Processes

In an electrochemical system, and therefore in fuel cells, two different processes occur at electrodes:

- *Faradaic processes*: this kind of processes are governed by Faraday's law i.e., the amount of chemical reaction caused by the current flow is proportional to the amount of electricity passed;
- *Non-faradaic processes*.

An electrode at which no charge transfer across the electrode/solution interface can occur, regardless of the imposed potential, is called *ideal polarized electrode* (IPE): while no real electrode behaves like an IPE, some electrode/solution systems approach the IPE model in limited potential ranges.

Since charge can't cross the IPE/solution interface even when the potential across it is changed, the interface exhibits a capacitor-like behavior: when a potential is applied to a capacitor, charge accumulates on its plates. For the interfacial region thus charge accumulates on the metal electrode and in the solution, with respect to the condition:

$$q^{electrode} = -q^{solution} \tag{1.8}$$

Or, dividing by the electrode area:

$$\sigma^{electrode} = -\sigma^{solution} \tag{1.9}$$

Usually given in $\mu C/cm^2$.

The whole array of charged species and oriented dipoles at the electrode/solution interface is called *electrical double layer* – although its structure loosely resembles two charged layers. In particular, the solution side of the double layer is composed of several layers:

- The **inner layer**, the one closest to the electrode, containing solvent molecules and ions that are *specifically adsorbed*. This layer is also called compact, Helmholtz, or Stern layer.

The locus of the electrical centers of these ions is called *inner Helmholtz plane* (IHP), and their total charge density is σ^i;

- Solvated ions can approach the electrode only to a greater distance, and the locus of their electrical center is called *outer Helmholtz plane* (OHP); since the interaction between electrode and solvated ions involves only long-range electrostatic forces, it is independent of the chemical properties of the ions. Their total charge density is σ^d. The solvated ions are *nonspecifically adsorbed*, and are distributed in a region called **diffuse layer**, extending from the OHP to the solution bulk.

Introducing the double layer, from equation (1.9) follows:

$$\sigma^{electrode} = \sigma^i + \sigma^d = -\sigma^{solution} \tag{1.10}$$

The structure of the double layer is important for an electrochemical system, because it can affect the rates of the electrode processes. Being heterogeneous reactions, the rate of the electrode processes depends also on mass transfer to the electrode and on surface effects, in addition to the usual kinetic variables; its interpretation is consequently complex.

Due to their heterogeneous nature, reaction rates for electrode processes are described in units of mol/s per unit area:

$$r\left[\frac{mol}{s\ cm^2}\right] = \frac{i}{nFA} = \frac{j}{nF} \tag{1.11}$$

Where j is the current density (A/cm^2).

Determining current as a function of potential is a way to obtain information about electrode reactions.

The departure of the electrode potential from its equilibrium value, i.e. the one calculated with the Nernst equation, upon the passage of faradaic current is called *polarization*, and its extent is measured by the *overpotential* η:

$$\eta = E - E_{eq} \tag{1.12}$$

For electrode processes, the general relationship between applied voltage and flowing current is given by the following equation:

$$E_{applied} = E + i \cdot R_s = E_{eq} + \eta + i \cdot R_s \tag{1.13}$$

The applied voltage must overcome the overpotential (E_{eq}+η) needed to support the electrochemical reaction rate corresponding to the current and the ohmic drop (iR_s) required to drive the ionic current in solution.

When a steady-state current is obtained, the rates of all reaction steps of the electrode process are the same and each value of current density is driven by a certain overpotential; this overpotential can be considered as the sum of term associated with different reaction steps: η_{mt} (mass-transfer overpotential), η_{ct} (charge-transfer overpotential), η_{rxn} (the overpotential associated with a preceding reaction). The whole process can then be represented by a series of impedances representing the various steps: R_{mt}, R_{ct}, R_{rxn}.

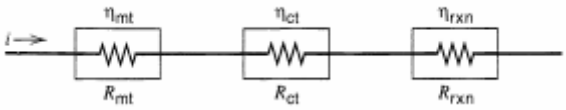

Figure 4: Impedances model for reaction overpotentials. From [2]

1.3.2. Mass-Transfer Controlled Reactions

For very simple electrode processes, in which the homogeneous reactions can be regarded as being at equilibrium and the surface concentration of reactants are related to the potential by an equation of the Nernst form, we can express the net rate of the electrode reaction r_{rxn} as a function solely of the rate at which the reactants are brought to the surface by mass transfer r_{mt}. It follows:

$$r_{rxn} = r_{mt} = \frac{i}{nFA} \tag{1.14}$$

Such reactions are called *reversible* or *Nernstian*.

Since mass transfer plays an important role in electrochemical dynamics, a brief review of its three modes is presented. They are:

I. *Migration*: the movement of a charged body under the influence of an electric field;
II. *Diffusion*: the movement of species under the influence of a concentration gradient;
III. *Convection*: its contribution is negligible for electrochemical systems and won't be considered.

Mass transfer to an electrode is governed by the Nernst-Planck equation, whose form for a 1-dimensional geometry is:

$$\dot{N}_i''(x) = -D_i \frac{\partial C_i(x)}{\partial x} - \frac{z_i F}{RT} D_i C_i \frac{\partial \phi(x)}{\partial x} + C_i u(x) \tag{1.15}$$

Where $\dot{N}_i''$ is the flux of species i (mol/s·cm^2), D_i is the diffusion coefficient, ∂Ci/∂x is the concentration gradient, z_i and C_i are the charge and concentration of species i, and u is the velocity with which a volume element in solution moves.

The three terms on the right hand side represent the diffusion, migration, and convection contributions of mass transfer.

If convection and migration are negligible, i.e. if the solution is calm at the electrode surface and if there is an excess of supporting electrolyte, the rate of mass transfer is proportional to the concentration gradient at the electrode surface and for a *Ox + ne$^-$ → Red* reaction we obtain, with a few passages:

$$r_{rxn} = \frac{i}{nFA} = m_{Ox}[C_{Ox}^{bulk} - C_{Ox}^{electrode}] = m_{Red}[C_{Red}^{electrode} - C_{Red}^{bulk}] \tag{1.16}$$

Where the proportionality constant m is the *mass-transfer coefficient* in [cm/s].

When $C_{Ox}^{bulk} - C_{Ox}^{electrode} \approx C_{Ox}^{bulk}$ we have the largest rate of mass transfer and thus the higher current. The value of the current under these conditions is called *limiting current*, i_l:

$$i_l = nFAm_{Ox}C_{Ox}^{bulk} \tag{1.17}$$

When the limiting current is flowing, the electrode process is occurring at the maximum possible rate.

1.3.3. Reaction Kinetics & Arrhenius Equation

Let us consider two substances, A and B, linked by the elementary reaction:

$$A \overset{k_f,k_b}{\Longleftrightarrow} B \tag{1.18}$$

Where k_f and k_b represents the rate constants of the forward and backwards reaction, respectively.
Both reactions are active at all times, and their rates are:

$$\begin{matrix} r_f = k_f C_A & for\ the\ forward\ reaction \\ r_b = k_b C_B & for\ the\ backwards\ reaction \end{matrix} \tag{1.19}$$

Consequently the net conversion rate of A to B is:

$$r_{net} = r_f - r_b = k_f C_A - k_b C_B \tag{1.20}$$

At equilibrium, where the net conversion rate is zero, the following equations hold:

$$\frac{k_f}{k_b} = K = \frac{C_B}{C_A} \tag{1.21}$$

$$r_f = r_b = r_0 \neq 0 \tag{1.22}$$

Where the term r_0 is called *exchange velocity* of the reaction.

According to the Arrhenius kinetic model, the relationship between rate constants and temperature is expressed in the form:

$$k = A \exp\left(-\frac{E_A}{RT}\right) \tag{1.23}$$

Where E_A is known as *activation energy.*

The exponential factor represents the probability of using thermal energy to surmount the energy barrier E_A, while the pre-exponential term A is the *frequency factor*, that is, the frequency of attempts on surpassing the activation energy barrier.

With this idea, we can picture reaction paths in terms of potential energy along a reaction coordinate: the reaction starts from the “reactant” configuration and progresses to the final “product” configuration. Both configurations occupy a minimum on the energy surface, since

they are the only arrangements possessing a non-negligible lifetime. As the reaction progresses, the coordinates change from those of the reactant to those of the product, along a path that – connecting two minima – must have a maximum, whose height is identified with E_A.

In another notation, E_A represents the change in standard internal energy in going from one of the minima to the maximum – which is called *transition state* or *activated complex* – and can be designated as the *standard internal energy of activation* ΔE^*.

By applying the definition of enthalpy, and since the pV term is usually negligible in a condensed-phase reaction, we obtain:

$$\Delta H^* = \Delta E^* + \Delta(pV)^* \approx \Delta E^* = E_A \tag{1.24}$$

We can now express the pre-exponential term in another way:

$$k = A \exp\left(-\frac{\Delta H^*}{RT}\right) = A' \exp\left(-\frac{\Delta H^* - T\Delta S^*}{RT}\right) = A' \exp\left(-\frac{\Delta G^*}{RT}\right) \tag{1.25}$$

Equation (1.25) holds because the exponential involving the term ΔS^* - called *standard entropy of activation* – is a dimensionless constant.

ΔG^* is the *standard free energy of activation*, the required free energy to go from the reactants (or products, if we consider the backwards reaction) to the activated complex, which can itself evolve into reactants or products. By applying the equilibrium constraint to the activated complex evolution reaction, after a few mathematical passages – and with some statistical mechanics – we obtain a new expression for the rate constants. The theoretical background for the following equations can be found at [2]:

$$\begin{aligned} k_f &= \frac{\kappa_T \kappa_B T}{h} \exp\left(-\frac{\Delta G_f^*}{RT}\right) \\ k_b &= \frac{\kappa_T \kappa_B T}{h} \exp\left(-\frac{\Delta G_b^*}{RT}\right) \\ k = k_f - k_b &= \frac{\kappa_T \kappa_B T}{h} \exp\left(-\frac{\Delta G^*}{RT}\right) \end{aligned} \tag{1.26}$$

Where κ_T is the transmission coefficient, which can take a value from 0 to 1, and κ_B and h are the Boltzmann and Planck constant respectively.

1.3.4. Butler-Volmer Equation

A general electrode reaction $Ox + ne^- \overset{k_f, k_b}{\Longleftrightarrow} Red$ has a forward path and a backward path, proceeding at their rates:

$$r_f = k_f C_{Ox}(x = 0, t) = \frac{i_{cathodic}}{nFA} \tag{1.27}$$

$$r_b = k_b C_{Red}(x=0,t) = \frac{i_{anodic}}{nFA} \tag{1.28}$$

Where x represents the distance from the surface of the electrode. Thus, the net reaction rate can be expressed as:

$$r_{net} = r_f - r_b = k_f C_{Ox}(0,t) - k_b C_{Red}(0,t) = \frac{i}{nFA} \tag{1.29}$$

By rearranging equation (1.29), we obtain an expression for the current i:

$$i = i_{cathodic} - i_{anodic} = nFA\left[k_f C_{Ox}(0,t) - k_b C_{Red}(0,t)\right] \tag{1.30}$$

Experience demonstrates that the reaction kinetics for electrodes are strongly influenced by the applied potential: we want to be able to predict the precise dependence of k_f and k_b on the potential.

Considering a general, one-electron electrode reaction $Ox + e^- \overset{k_f,k_b}{\Longleftrightarrow} Red$ we obtain:

$$k_{Ox} = f(E) \rightarrow k_{Ox} = k'' \exp\left(-\frac{\Delta G^*_{Ox}(E)}{RT}\right) \tag{1.31}$$

$$k_{Red} = f(E) \rightarrow k_{Red} = k'' \exp\left(-\frac{\Delta G^*_{Red}(E)}{RT}\right) \tag{1.32}$$

Where

$$k'' = \frac{\kappa_T \kappa_B T}{h} \tag{1.33}$$

When we change the applied potential, we shift – upwards or downwards – the activation energy curve. This concept, and its influence on the reaction kinetics, is thoroughly explained in [2]. Here we will report only a simple mathematical model of the theory.

Firstly, we linearize the $\Delta G^*(E)$ function via 1st-order Taylor series approximation around the standard potential E_0. We have:

$$\Delta G_{Ox}(E) = \Delta G_{Ox}(E_0') + \alpha F(E - E_0') \tag{1.34}$$

$$\Delta G_{Red}(E) = \Delta G_{Red}(E_0') - \beta F(E - E_0') \tag{1.35}$$

Where α and β represent:

$$\alpha = \frac{1}{\mathrm{F}} \frac{dG_{Ox}(E)}{dE}_{|E_0'} \tag{1.36}$$

$$\beta = -\frac{1}{\mathrm{F}} \frac{dG_{Red}(E)}{dE}_{|E_0'} \tag{1.37}$$

We now substitute into equations (1.31) and (1.32) the expressions for ΔG_{Ox} and ΔG_{Red}:

$$k_{Ox} = k'' \cdot \exp\left[-\frac{\Delta G_{Ox}(E_0')}{RT}\right] \cdot \exp\left[-\frac{\alpha F(E - E_0')}{RT}\right] \tag{1.38}$$

$$k_{Red} = k'' \cdot \exp\left[-\frac{\Delta G_{Red}(E_0')}{RT}\right] \cdot \exp\left[\frac{\beta F(E - E_0')}{RT}\right] \qquad (1.39)$$

The first two terms at the right hand side of equations (1.38) and (1.39) represent the *standard rate constant* k_0, i.e. the rate constant of the reaction at equilibrium, whose value doesn't depend on the applied potential. Furthermore, it holds the equivalence β=1- α [2].

By inserting relations (1.38) and (1.39) into (1.30), we obtain the current-potential relation, which is known as **Butler-Volmer equation***:*

$$i = FAk_0\left[C_{Ox}(0,t)\exp\left(-\frac{\alpha F(E - E_0')}{RT}\right) - C_{Red}(0,t)\exp\left(\frac{(1-\alpha)F(E - E_0')}{RT}\right)\right] \qquad (1.33)$$

The term k_0 represents not only the standard rate constant, but also the kinetic facility of the redox couple: if k_0 is large, the system will achieve equilibrium on a short time scale, otherwise if k_0 is small it will be sluggish. The term α, instead, is the *transfer coefficient* and is a measure of the symmetry of the activation energy barrier.

1.3.5. Exchange Current & Approximate Forms of the Butler-Volmer Equation

At equilibrium, the net current is zero and the value of the electrode potential is dictated by the Nernst equation. From equation (1.33), by applying the equilibrium constraint, we obtain:

$$FAk_0C_{Ox}(0,t)\exp\left(-\frac{\alpha F\left(E_{eq} - E_0'\right)}{RT}\right) = FAk_0C_{Red}(0,t)\exp\left(\frac{(1-\alpha)F\left(E_{eq} - E_0'\right)}{RT}\right) \qquad (1.34)$$

Since equilibrium applies, the surface concentrations of Ox and Red are the same as the bulk concentrations. Hence:

$$\frac{C_{Ox}^{bulk}}{C_{Red}^{bulk}} = \exp\left(\frac{F\left(E_{eq} - E_0'\right)}{RT}\right) \qquad (1.35)$$

Which is the exponential form of the Nernst equation. In fact, rearranging (1.35) leads to:

$$E_{eq} = E_0' + \frac{RT}{F}\ln\frac{C_{Ox}^{bulk}}{C_{Red}^{bulk}} \qquad (1.36)$$

Another consequence of the equilibrium is that the faradaic activity is balanced: we can express this in terms of *exchange current*, i_0, whose magnitude is equal to the backwards and forward reactions current. After a few mathematical passages [2], we obtain:

$$i_0 = FAk_0C \qquad (1.37)$$

Where $C = C_{0x}^{bulk} = C_{Red}^{bulk}$. For heterogeneous reactions, the exchange current is normalized to unit area to obtain the *exchange current density* j_0.

With the introduction of i_0 we can re-express the current in terms of overpotential, the deviation from the equilibrium potential, rather than the formal potential, obtaining the following equation:

$$i = i_0 \left[\frac{C_{Ox}(0,t)}{C_{Ox}^{bulk}} \exp\left(-\frac{\alpha F \eta}{RT}\right) - \frac{C_{Red}(0,t)}{C_{Red}^{bulk}} \exp\left(\frac{(1-\alpha) F \eta}{RT}\right) \right] \tag{1.38}$$

Equation (1.38) is also known as current-overpotential equation; the behavior it predicts is depicted in the following figure:

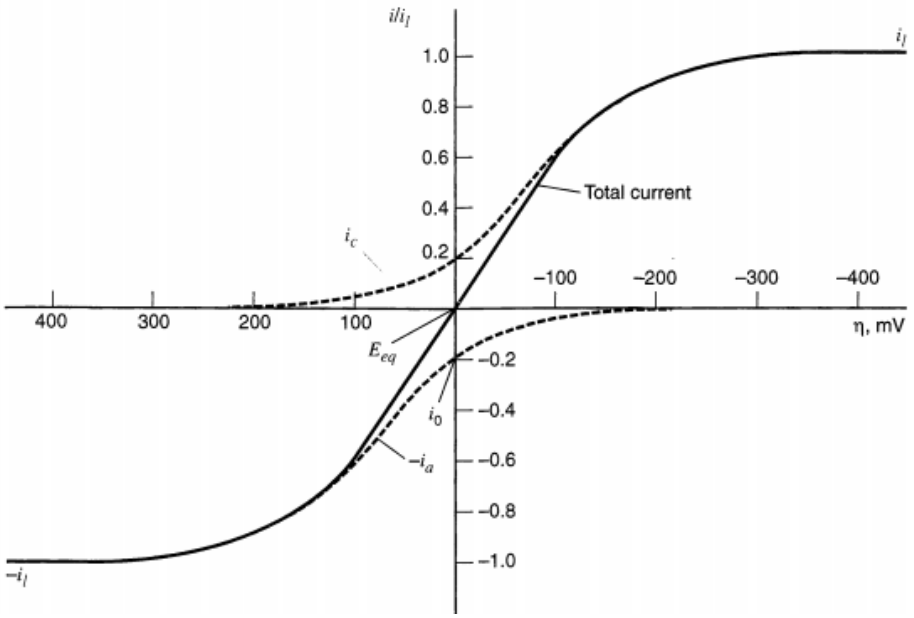

Figure 5: Current-overpotential equation

We can point out 3 approximate forms of the current-overpotential equation:

I. **No mass-transfer effects**: if the surface concentrations are the same as the bulk values, equation (1.38) can be simplified to

$$i = i_0 \left[\exp\left(-\frac{\alpha F \eta}{RT}\right) - \exp\left(\frac{(1-\alpha) F \eta}{RT}\right) \right] \tag{1.39}$$

This approximation holds until i is less than 10% of the smaller limiting current.

If the exchange current i_0 is very large, the system supplies large currents (even the mass transfer limited one) with small overpotentials. In this case, the observed overpotential is caused by the changing surface concentration of oxidized and reduced species and is called *concentration overpotential*: it can be seen as the activation energy required to "push" mass transfer to the rate required to support the current. If i_0 is small, on the other hand, the system supplies non-negligible current only is the overpotential is very high.

We can, in conclusion, see the exchange current as a "idle current" for charge exchange across the surface, and its value measures the system's ability to deliver a net current without a significant energy loss due to activation.

II. **Small overpotentials and linear characteristics**: the exponential form e^x can be approximated as 1+x if the value of x is small enough. Hence, if the overpotential is small enough, equation (1.38) becomes:

$$i = -\frac{i_0 F}{RT}\eta \qquad (1.40)$$

Equation (1.40) shows that, in a narrow potential range near E_{eq}, the net current is linearly related to the overpotential. The ration –η/I has units of resistance and is called *charge-transfer resistance*, R_{ct}:

$$R_{ct} = -\frac{\eta}{i} = \frac{RT}{F i_0} \qquad (1.40)$$

R_{ct} is the negative reciprocal slope of the current/overpotential curve near the origin.

III. **Large overpotentials and Tafel behavior**: if the overpotential – either negative or positive – is large enough, one of the exponential terms in equation (1.39) becomes negligible. If $\eta \rightarrow -\infty$, the second exponential is negligible and we obtain:

$$i \sim i_0 \exp\left(-\frac{\alpha F \eta}{RT}\right) \qquad (1.41)$$

By rearranging equation (1.41), we obtain:

$$\eta = \frac{RT}{\alpha F}\ln i_0 - \frac{RT}{\alpha F}\ln i \qquad (1.42)$$

Which is another form of the **Tafel equation**, originally given in 1905 as

$$\eta = a + b\,\mathrm{Log}\, i \qquad (1.43)$$

Constants a and b, which are empirically determined in the original form of the equation, can be identified as:

$$a = \frac{2{,}3RT}{\alpha F} Log\ i_0 \ \ and \ \ b = -\frac{2{,}3RT}{\alpha F} \qquad (1.44)$$

The approximation, and thus Tafel equation, holds whenever the back reaction's contribute is less than 1% of the current, i.e. when exp (Fη/RT) ≤ 0,01: this is possible as long as |η| > 0,118 V at room temperature.

1.3.6. Tafel Plots

Plots of log i vs. η are known as *Tafel plots* and are used to evaluate kinetic parameters. In general they are composed of an anodic branch with slope (1-α)F/2,3RT and a cathodic branch with slope -αF/2,3RT. We can distinguish three regions in a Tafel plot:

- A central part where the relationship between overpotential and log i is linear, as predicted by the Tafel equation;
- At very large overpotentials, even if the value of η increases, log i remains constant: this is the *mass-transfer limited* region;
- As the overpotential approaches zero, the plot deviates sharply from the linear behavior because the back reaction is no longer negligible.

1.4. Losses in DMFC

During normal operation for DMFC what is measured is not the standard potential but the open circuit voltage, i.e. the cell voltage while current is not flowing. From this point on, the open circuit voltage will be called OCP (*open circuit potential)*. The relationship between standard potential and OCP is:

$$OCP = E_0 - E_{crossover} - E_{parasitic} \qquad (1.45)$$

While an ideal cell would work at a voltage equal to the OCP independently of the flowing current, the real-cell voltage is not only always lower than the ideal OCP, but it also decreases when the flowing current increases: this behavior is known as polarization losses, and it is represented by the so-called polarization curve, the voltage/current intensity curve. A typical DMFC polarization curve is reported here in the figure:

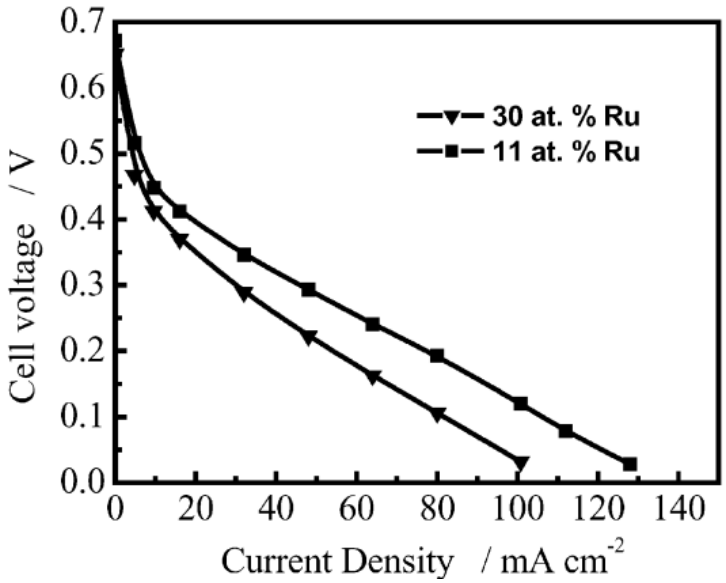

Figure 6: Polarization curve for a DMFC. The influence of different catalyst composition is compared. From [3]

The polarization curve reflects the different limiting mechanisms during DMFC operation:

- At low operating current density, the voltage is mainly influenced by **activation losses**, caused by kinetic limitations: in order to overcome the half-reaction activation energy you have to spend (and therefore lose) a certain amount of voltage;
- At high operating current density, predominant losses are **concentration losses**: if the current density is high, half-reactions take place at high rate and consume many reactants. In this case mass transport is unable to provide reactants to the electrodes' surface – where the half-reactions take place – and voltage is lost;
- In between the curve has a linear decreasing trend, where voltage is influence by **ohmic losses** due to the electrolyte membrane resistance to the flux of ions.

While cathode and membrane overpotentials are similar to PEMFCs, because cathodic half-reaction and electrolyte are the same for both DMFCs and PEMFCs, anodic activation losses in DMFCs are much more important because the methanol oxidation reaction rate is very slow, many orders of magnitude slower than hydrogen oxidation reaction rate.

1.5. Electro-Oxidation of Methanol

As introduced in the previous paragraph, anodic overpotentials for a DMFC are very high because of the slow methanol oxidation reaction rate: methanol molecules are more complex than hydrogen, therefore the catalytic electro-oxidation of this molecule is more complicated and consists in several reaction steps, each of which has its own activation energy.

The complete methanol oxidation reaction mechanism, although it has been studied for years, is not completely known as of today. However, a simplified reaction scheme for methanol oxidation is [4]:

$$CH_3OH \rightarrow (CH_3OH)_{ads} \qquad Methanol\ adsorbtion \qquad (1.46)$$

$$(CH_3OH)_{ads} \rightarrow (CO)_{ads} + 4H^+ + 4e^- \qquad C-H\ bond\ dissociation \qquad (1.47)$$

$$(CO)_{ads} + H_2O \rightarrow CO_2 + 2H^+ + 2e^- \qquad CO\ oxidation \qquad (1.48)$$

The 3 reaction steps require a platinum-based catalyst, because platinum is the most efficient material in promoting the C-H bond dissociation. With a platinum catalyst, methanol oxidation takes place via two processes occurring in separate potential (or, which is the same, energy activation) regions:

- The first process is the adsorbtion of methanol molecules. This step requires several neighboring active sites, and can begin only if the potential is high enough to free from adsorbed H ions the Pt active sites, because methanol alone cannot force them out. This process therefore begins at 0,2 V *vs RHE* (i.e. Versus the *reference hydrogen electrode*,

which is the standard reference electrode in electrochemistry). From here on the suffix *vs RHE* while always be implied and won't be repeated;

- The second process is CO oxidation: this step takes place only after water is dissociated, because water is the molecule giving away the oxygen atoms required by the oxidation reaction. On a pure platinum catalyst, water begins to dissociate at 0,45 V, however the adsorbate layer is not reactive enough if the potential is below 0,7 V [5].

Iwasita [5] identifies the second process as the rate-determining step for potentials between 0,5 V and 0,7 V, while at higher potentials methanol adsorption becomes the rate-determining step.

Since these potentials are high (in comparison with typical values for a fuel cell), during normal operating conditions platinum is unable to generate enough oxygen to effectively oxidize CO and the catalyst suffers from severe CO poisoning: carbon monoxide occupies the free active sites before water dissociation can take place and the catalyst is unable to oxidize it.

In order to solve this problem, platinum is often coupled with another metal able to dissociate water and produce oxygen: in literature many bimetallic catalysts, where platinum is coupled with gold, molybdenum, tungsten, cobalt, are suggested. However as of today there is a general consensus that platinum/ruthenium offers the best results, i.e. exhibits the lowest onset potential for CO oxidation. Ruthenium enhances the performance of the catalyst towards CO oxidation thanks to three factors: Ru generates oxygen-containing species at potentials as low as 0,3 V, it modifies the electronic properties of Pt by the PtRu orbital overlap and promotes CO migration towards ruthenium active sites, where it is oxidized preferentially [6].

Consequently, CO oxidation on a platinum/ruthenium catalyst can be simplified with this mechanism [4]:

$$Pt + CH_3OH \rightarrow Pt(CO)_{ads} + 4H^+ + 4e^- \qquad CO\ \ adsorbtion \qquad (1.49)$$

$$Ru + H_2O \rightarrow Ru(OH)_{ads} + H^+ + e^- \qquad OH\ adsorbtion \qquad (1.50)$$

$$Pt(CO)_{ads} + Ru(OH)_{ads} \rightarrow CO_2 + Pt + Ru + H^+ + e^- \qquad CO\ oxidation \qquad (1.51)$$

1.6. Carbon-Based Anodic Supports for DMFC

In order to achieve good performance at the anodic side, the catalytic layer should present the following features: high electric and protonic conductivity, so that it can promote electron and ion transport, high active surface area, so that it can guarantee a fine dispersion and high utilization of the catalyst, and high porosity, in order to help the reactants' diffusion onto the active sites and to help establishing an efficient contact between catalytic layer, electrode and electrolyte membrane.

Consequently, the electrode is composed of a catalyst – in the form of nanoparticles – and a support. The state-of-the-art support for DMFC is made up of carbon: it has relatively high

stability in both acidic and basic media, good electric conductivity, high specific surface area and good porosity.

The support heavily influences the catalyst performance, therefore its optimization is a very important aspect while developing DMFC. Many works have in recent years focused on this aspect, understanding the effects of supports and exploring new carbon supports:

In DMFCs three carbon-based supports are frequently used:

- **Carbon black**: it's the most commonly used support for DMFC anode catalysts. It's usually manufactured by pyrolyzing hydrocarbons such as natural gas or oil fractions taken from refinery processing. It shows high specific surface area ((~250 m^2/g for *Vulcan XC-72*) and good porosity, leading to a good contact between catalyst particles and electrolyte membrane [7];
- **Nanostructured carbon**: the family of carbon nanotubes (*CNTs*) is the most well-known nanostructured carbon. CNTs-supported catalysts lead to a higher cell voltage and twice the power density than carbon black-supported platinum. However, CNTs production processes are still extremely costly and not yet developed for industrial large-scale applications [7];
- **Mesoporous carbon**: this carbon support has tuneable pore sizes in the range 2-50 nm, which would provide an excellent contact between catalyst, electrolyte membrane and electrode. Moreover it has the potential to enhance the utilization of the catalyst and the reactants transport to the catalytic sites [7].

Nonetheless, carbon is prone to *carbon corrosion* when subject to the acidic, harsh environment found in low temperature fuel cells. Carbon corrosion is an electro-chemical oxidation which reduces the active surface area of the support and accelerates platinum sintering, decreasing the cell power output and its efficiency.

Carbon corrosion reaction is actually unfavorable at low potentials and low temperatures (it doesn't happen if the potential is below 1,1 V), but takes place nevertheless due to the presence of platinum, which catalyzes the reaction when the potential is 0,55 V. The corrosion reaction can be split up in two processes; the first is carbon monoxide formation on the support surface, while the second is CO to CO_2 conversion.

$$C + H_2O \rightarrow (CO)_{ads} + 2H^+ + 2e^- \tag{1.52}$$

$$(CO)_{ads} + H_2O \rightarrow CO_2 + 2H^+ + 2e^- \tag{1.53}$$

The global reaction is therefore

$$C + H_2O \leftrightarrow CO_2 + 4H^+ + 4e^- \quad E_0 = 0{,}207\,V \tag{1.54}$$

Additionally, the carbon support degradation accelerates Pt sintering, leading to a further decrease in electrochemical, active surface area and in output power. The platinum catalyst deterioration occurs with two mechanism:

- **Migration and coalescence**: the catalyst particles migrate on the support surface and coalesce;
- **Dissolution and redeposition**: the catalyst particles are dissolved, then diffuse through the electrolyte and redeposit in larger particles.

1.7. Alternative Supports for DMFCs

1.7.1. Metal-Oxide Based Supports for Low Temperature Fuel Cells

Since the commercialization and diffusion of fuel cells is hindered by the high costs of the materials, in particular the costs of the platinum catalyst and the membrane, many studies have suggested the use of new materials to modify or replace the existing ones.

Metal oxides have abundant sources, generally low price, high chemical and electrochemical stability, abundant hydroxyl group on the surface (which are very reactive), and strong interaction with metal nanoparticles: this class of materials is therefore a promising candidate to reduce the present problems of DMFCs and PEMFCs.

In the last few years many researchers have focused on metal oxide materials; apart from their wide applications in various fields, they have important characteristics that make them a suitable candidate as a PEMFC and DMFC material, both as a catalyst and as a support:

- Higher corrosion resistance in electrochemical environment of PEMFCs and DMFCs compared with carbon. Being metal oxides, they exist as a high oxidative state and aren't oxidized furtherly;
- As supports, they often have strong interaction with the metal catalyst particles: this phenomenon, known as *strong metal-support interaction* (SMSI), could prevent the sintering of the metal particles and could produce an electronic effect that modifies the catalytic property of the catalyst;
- The abundance of hydroxyl group on their surfaces could promote their role from 'mere' supports to co-catalysts, based on a bifunctional mechanism [8].

Among the many metal oxides, some of the most promising materials for DMFC cathodes are:

- **Manganese oxides**. Manganese is not only inexpensive and earth-abundant, but it also changes it oxidation states from +2,+3 to +4 near the equilibrium potential of the oxygen reduction reaction (ORR): due to these features, many researchers have studied its activity for the ORR. MnO_2 nanowires, used as a support for a Ni nanoparticles catalyst, shows an excellent activity and a quasi-4 electron transfer process for the ORR [9]; moreover Mn_3O_4, both as a Pt catalyst support and as a non-noble metal catalyst itself, exhibits high specific activity for the ORR and high limiting current;

- **Cerium oxide**. CeO_2 is known to switch between Ce^{4+} and Ce^{3+} oxidation states depending on whether it is in presence in an oxidizing or a reducing atmosphere; it also contains many oxygen vacancies within its structure, leading to high oxygen mobility. Xu et al. [10] modified a commercial Pt/C catalyst with CeO_2 and found that the introduction of cerium oxide enhances the ORR activity, due to a proposed mechanism in which CeO_2 is firstly reduced and then oxidized by an ORR intermediate to its original state, promoting the reaction and the fuel cell performance. It was also discovered [11] that CeO_2 improves the performance of Pt/C catalyst for MOR and the resistance ability to CO poisoning.

For the DMFC anode instead two interesting materials are:

- **Tungsten oxides**. Tungsten oxides (WO_x) are stable in acidic solution, and react with active hydrogen adsorbed on Pt to form a very resistant "pseudo-metallic" conductor compound named *hydrogen tungsten bronzes* [12]. WO_3 has been used as a support for Pt and PtRu catalyst and has shown an enhanced activity in the electro-oxidation of methanol [13] and a superior resistance to poisoning than the bare catalyst.
  This enhancement has been mainly attributed to the *hydrogen spillover effect*: the formation of hydrogen tungsten bronze enhances the efficiency of Pt active sites as dehydrogenation catalysts and fastens the desorption of poisonous reaction intermediates. Furthermore, WO_3 itself is strongly resistant to CO poisoning and eases the formation of OH_{ads}, the intermediate which oxidizes carbon monoxide;
- **Titanium oxides**. Titanium oxides have been widely applied in photoelectric fields and have been studied as PEMFCs and DMFCs materials: they are cheap, non-toxic, and have a strong interaction with metal nanoparticles, changing their electronic properties. Sub-stoichiometric oxides have high electronic conductivity (for Magnéli Phase oxides, with a general formula Ti_nO_{2n-1}, is comparable to carbon) and highly resistant to oxidation and corrosion, while stoichiometric oxide (TiO_2) have many interesting features and are discussed in the following paragraph.

Among these alternative materials, titanium-based oxides and compounds are the most studied and most promising ones, because they have good physical and chemical properties and are generally economical.

1.7.2. Titanium Dioxide

Titanium dioxide (TiO_2) or titania is a metal oxide that comes in several polymorphic forms, among which the most commercialized are *rutile* and *anatase.* Titania has been studied for many energy-related applications because of its unique properties: it is an effective UV absorber, making it suitable as a photocatalyst, it has a high strength-to-weight ratio, is corrosion-resistant and exhibits high surface area when nanostructured.

In fuel cells application, TiO_2 is able to improve the overall cell performance either as a catalyst support or as membrane material. Many examples of successful applications of TiO_2 in DMFC can be found in literature:

- Baglio et al. developed a composite Nafion/TiO_2 membrane showing good properties for operation at high temperature (145°C), with an improvement in performance as the particle size of TiO_2 decreased [14];
- Yang et al. presented a composite membrane of polyvinyl alcohol/TiO_2 nanotubes/polystyrene sulfonic acid with low methanol permeability and better performance than Nafion 117 [15];
- As a support, Kolla and Smirnova fabricated a hybrid catalyst, incorporating TiO_2 into a PtRu/C commercial catalyst. The fabricated material showed higher methanol oxidation activity, higher CO tolerance, lower CO oxidation onset potential and better chemical stability [16];
- Drew et al. developed a TiO_2-supported PtRu catalyst, which showed an improved surface area, a diminished poisoning effect and enhanced performance in comparison with a non-supported catalyst [17];
- Arulmani et al. studied a PrRu catalyst supported by TiO_2 and carbon and found under UV illumination a 5-fold enhancement in the peak current generated by the methanol oxidation reaction, compared to the non-irradiated case [18].

Despite its advantages, TiO_2 has drawbacks limiting its effective application in fuel cell technology: being an oxide, it has low electric conductivity, many orders of magnitude smaller than carbon. Furthermore its polymorphic forms have a wide band gap – 3 eV for rutile and 3,2 eV for anatase – therefore they show photocatalytic activity only when irradiated by UV light (with wavelengths smaller than 380 nm). Since only 8% of the solar spectrum falls in the UV region, photocatalytic activity under solar illumination would be very limited and inefficient.

In order to overcome these drawbacks, different strategies have been pursued. One of the most investigated is the modification of the TiO_2 lattice structure by doping the material.

Narrowing the band gap of TiO_2 can be achieved through thermal doping, inserting into the TiO_2 crystalline structure non-metallic atoms like nitrogen, carbon or sulphur. Some researchers have developed efficient methods for doping anatase nanotubes, via thermal annealing under CO flow [19] or via flame annealing [20], obtaining materials with band gap of, respectively, 2,22 eV and 2,84 eV able to absorb and generate photocurrent also in the visible spectrum. Others [21] modified the crystalline structure of TiO_2 nanoparticles, hydrogenating and doping their surface, obtaining a band gap of 1,54 eV, extending the photoactivity of the material to the visible spectrum.

1.7.3. Titanium Nitride

The use of transition metal nitrides as catalysts for hydronitrogenation in industrial processes [22] has inspired the study of their applicability as electrocatalytic materials, thanks to their stability in extreme-pH condition and under high applied electrochemical biases.

Among transition metal nitrides, some researchers are beginning to study titanium nitride (TiN) as a promising catalyst support material for low-temperature fuel cells. Already investigated as material for super capacitors, TiN not only shares the same features of other nitrides, but has also very high electrical conductivity, is biocompatible, and has outstanding oxidation and acid corrosion resistance. Furthermore, researchers have discovered a peculiarity in its electronic structure, i.e. the transfer of part of s- and d-valency electrons of the Ti atoms – responsible for the covalent bonding of Ti with foreign atoms – to the 2p-states of N atoms, which makes TiN a great electron acceptor [23].

Despite its peculiar features, TiN has not been extensively studied as material for PEMFCs and its applications as catalyst support are still limited.

The use of TiN as support for Pt catalyst for MOR has been reported in [24]. Although TiN is inactive towards methanol oxidation, when coupled with the catalyst it enhances its resistance to CO poisoning and the reaction rate for the MOR. Furthermore, during cyclic voltammograms performed in a H_2SO_4 and methanol-containing solution, the surface density of OH^- groups increases: this effect is believed to be caused by the surface oxidation of TiN, and the formation of –OH groups improves the removal efficiency of the CO adsorbed by the Pt catalyst.

B. Avasarala et al. [23] confirmed the previous hypothesis with XPS analysis of a TiN-nanoparticles-supported Pt catalyst. During cyclic voltammograms, TiN is electrochemically oxidized, with the formation of a oxide/oxynitride film with a few nanometers thickness. This core-shell structure has high conductivity, because the oxynitride layer – until the percentage of oxygen is below 40% - behaves like a Magnéli Phase oxide with metal-like properties. However, after an accelerated durability test consisting in repeated potential cyclic under simulated PEMFC conditions, ECSA decreases after few hours of operation. This trend is explained with the the dissolution of the oxynitride layer and the creation of a surface hydroxide layer which prevents the TiN support to conduct electrons from the Pt catalyst, resulting in a near-zero ECSA. They conclude that this phenomenon is strongly influenced by concentration and type of acid media, and that through reduction of surface hydrolysis – with various coatings, for example – TiN can become a durable catalyst support for PEMFCs and replace carbon.

Other studies have investigated the role of TiN as catalyst support for DMFCs: Yang [25] fabricated a mesoporous TiN support for a Pt catalyst, and confirmed the chemically inert and stable nature of TiN through CV analysis. Furtermore, it is shown that the TiN/Pt catalyst shows a higher ECSA than commercial Pt/C, thanks to the small Pt nanoparticles obtained, and an enhanced activity: TiN-supported Pt shows a lower onset potential for MOR, a higher oxidation peak current density, and an outstanding activity. It is suggested that the cause of this increased

performance is the metal-like conductivity of TiN (395 S/cm), that combined with its chemical stability makes it an interesting support material for DMFCs.

Finally, in [26] and [27], TiN-supported Pt catalysts are tested for DMFCs and PEMFCs applications, respectively. In the former application, the titanium nitride-supported catalyst shows a high value for the ratio between the two oxidation peaks observed during cyclic voltammograms performed in a methanol-containing solution – indicating, according to the authors, a better efficiency – and a higher activity than a standard PtRu/C catalyst; this superior performance is attributed to the formation on TiN of a surface –OH layer which increases the oxidation rate of CO produced as intermediate of the MOR, fastening the regeneration of the Pt catalyst. In the latter application, it is shown that the TiN/Pt catalyst shares the same CV behavior of commercial Pt/CB and Pt/GCB, and a higher ECSA after extensive potential step cycling: this feature – that hints to a superior stability of the TiN/Pt catalyst in comparison to the commercial Pt/CB – is due to the *strong metal-support interaction* that slows down the catalyst sintering, and to the removal of a sub-nanometric layer of TiO_2 covering the Pt particles.

1.8. Goals of the Work

Having examined the literature and the state-of-the-art solutions for DMFCs, the main objective of this thesis work is the fabrication, optimization and characterization of a titanium nitride based support for DMFCs, to understand which could overcome the drawbacks of carbon and replace it as standard support material for the catalyst.

This work is part of a bigger project with the final aim of obtaining a photo-electrocatalytic material for DMFCs, and in order to achieve this final objective TiN has been chosen has a promising starting point towards the development of a N-doped titanium dioxide support able to photogenerate current. More precisely, TiN shows beneficial properties that make its implementation as a support material for DMFC interesting:

- As **anodic support**, titanium nitride and particularly its oxide, titanium oxynitride (TiON), is able to photogenerate current, holding promises for the future fabrication of a photoelectrocatalytic material with enhanced efficiency and performance towards MOR. Furthermore, its oxophylicity could probably help in reducing the ruthenium catalyst loading, since this property could fasten the removal and the conversion of MOR intermediates from the Pt catalyst sites;
- As **cathodic support**, since many studies have shown that the ceramic/metallic hybrid nature of TiN leads to a high chemical stability in acidic media and under high applied potential bias, titanium nitride could be implemented as cathode support material, where carbon exhibits stability problems due to the harsh environment.

The TiN support will be fabricated through a PVD-based system, Pulsed Laser Deposition (PLD): this system allows the control of the morphology and the composition of the material – and

thus its properties – up to the molecular and atomic scale. For the purpose of this work, the TiN support will be nanostructured into quasi-1D, hierarchical and mesoporous supports with very high surface area, in order to maximize the catalyst dispersion and utilization.

The obtained material will be structurally characterized via SEM, XRD and Raman analysis, and electrochemically tested via half-cell measurements.

The catalyst will be deposited onto the support with DC Sputtering and electrodeposition techniques, and finally the complete material (support and catalyst) will be tested structurally and electrochemically.

Chapter 2

Fabrication Systems & Analysis Methods

2.1. Fabrication & Depositions Methods

2.1.1. Pulsed Laser Deposition

Pulsed Laser Deposition (PLD) is a physical vapor deposition (PVD) technique where high power laser pulses are used to evaporate and ionize material from the surface of a target. During this process, known as *ablation*, a plasma plume – composed of the vaporized target material – is created, expanding rapidly away from the target in vacuum (or in a background gas). The laser-produced plasma plume, containing neutrals, ions, electrons etc., is then collected on a substrate, upon which it condenses and a thin film grows.

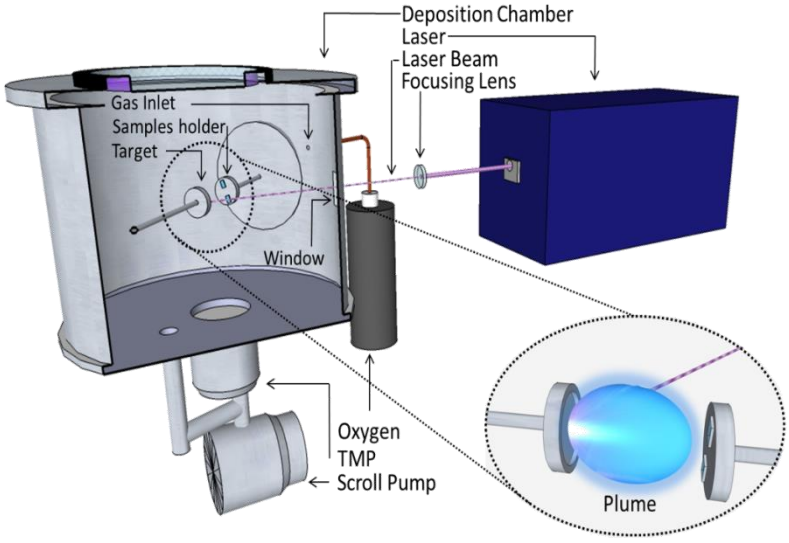

Figure 7: Illustration of a typical PLD vacuum chamber [28]

Despite being a simple technique, the whole physical process underlying PLD is very complicated: it depends on various parameters, which strongly affect the properties and the growth of the film, and the totality of processes happening during the ablation is not fully understood.

In comparison with other PVD deposition techniques, PLD has some significant benefits:

- In theory, it is capable of a stoichiometric transfer of material from target to substrate [29], i.e. it can reproduce in the deposited film the exact chemical composition of complex materials (like YBCO, yttrium barium copper oxide);
- The deposition rate can be relatively high (up to 0.1 nm per pulse) [29];
- The morphology of the film – and therefore its structural properties – can be fine-tuned by modifying some process parameters;
- Using the laser as an external energy source, the process is clean, thus the deposition can occur in vacuum or in the presence of both inert and reactive background gases, giving the user the possibility of easily growing different kinds of films;

- The pulsed nature of PLD gives the possibility of precisely controlling the number of particles arriving at the substrate: this means that layer-by-layer growth can be achieved by adjusting simple parameters of the laser [30].

However, it has also some drawbacks:

- PLD suffers from the so-called "hydrodynamic sputtering" [29]: along with atoms and ions, some undesired droplets of target material are also deposited on the substrate due to the pulsed laser illumination. This process cannot be completely avoided;
- The focused pulsed laser beam produces a distribution of ablated material that is strongly peaked in the forward direction: therefore, uniformity in the film thickness can be achieved only in a narrow angular range [31].

2.1.2. The PLD Physical Process

The full PLD process can be described by 5 stages [30], which will be briefly discussed below. The stages of ablation are actually more complicated, but a meticulous description falls outside of the objectives of this work:

I. **Light absorption**: the electrons of the solid initially absorb the laser energy and, after a few picoseconds, convert it as heat. During this phase the heating rate is very high (~10^{12} K/s), and the electrons and the atoms equilibrate at high temperature. The high heating rate of the target surface is wat ensures that all target components – irrespective of their partial binding energies, negligible when considering the concentrated laser pulse – evaporate at the same time;
II. **Initial plume expansion***: t*he strong energy deposition leads to the explosive evaporation of ions, electrons and neutral atoms: they form a high-temperature plasma plume, which absorbs and is ionized by part of the laser light;
III. **"Free" plume expansion**: the plume expands adiabatically in vacuum, and eventually its particles perform a free motion. If a background is present, the free expansion will take place until the plume pressure has decreased. Up until this stage, the composition of the plume is more or less the same as the target;
IV. **Slowing down of the plume**: if a background gas is present, it slows down the plume, while the atoms diffuse out of the plume and migrate to the substrate. The slowing down leads to a shock-wave behavior at the contact front between the plume and the gas, and the angular distribution of the plume atoms is influenced by the pressure and molecular weight of the background gas. During this final diffusion the flow behaves strongly non-stoichiometric;
V. **Growth of the film on the substrate**: the atoms arriving from the plasma plume hit the collecting substrate, and have typically sufficient kinetic energy to diffuse some distance on the surface until they find an energetically favorable bond with other atoms (of the film or of the substrate) and grow.

During PLD, by modifying the kinetic energy of the ablated particles it is possible to influence the film properties. This effect can be obtained changing many experimental parameters:

- *Background gas pressure*: it is possible to tune the kinetic energy of the deposited particles by modifying the background gas pressure. If the background gas pressure is high enough, the plasma expansion leads to a shock front between the plume and the gas, which slows down the plasma particles and decreases their kinetic energy. An increase in the gas pressure leads also to an increased scattering of the ablated ions during their flight towards the substrate;
- *Substrate/target distance:* a variation of this parameter leads to the same outcome obtained when modifying the background gas pressure. The bigger the substrate/target distance, the more the kinetic energy of the ablated particle decreases and the more porous is the deposited film.
- *Substrate nature*: the type of substrate upon which the film is deposited plays a non-negligible role in the film growth, because the substrate roughness influences the distribution of energetically favorable nucleation sites and can therefore strongly influence the morphology of the resulting film.

If the PLD system is seen as a "black box", the variation of these three parameters leads to the same outcome: the variation of the film morphology and of its porosity, related to the kinetic energy of the deposited particles. High kinetic energy means a more compact film, while lower energies lead to the formation of a more porous structure.

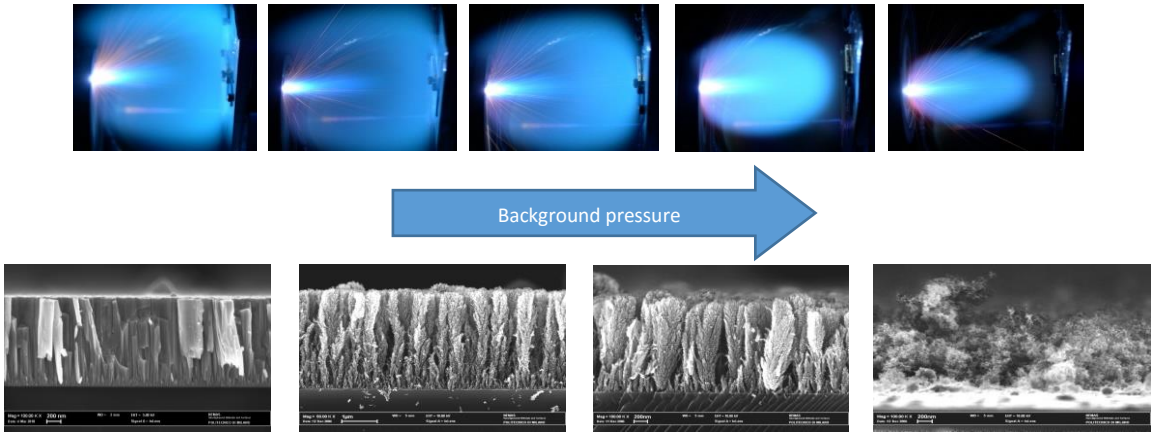

Figure 8: Pressure/morphology relationship for PLD films [28]

2.1.3. PLD Application for Support Deposition

Among the many deposition techniques, Pulsed Laser Deposition was used to fabricate the TiN supports: as previously stated, thanks to the peculiarities of PLD it is possible to control the morphology and the composition of the fabricated film – and thus its properties – up to the molecular and atomic scale. An essential feature for a low-temperature fuel cell catalytic support is a high surface area, in order to optimize the Pt catalyst dispersion and utilization. Therefore, the fabrication process was focused on obtaining a nanostructured film that could

represent the best trade-off between porosity/high-surface area – which corresponds to a high background gas pressure – and mechanical resistance – which corresponds to a lower background gas pressure.

The films were deposited on two substrates:

- FTO (fluorine-doped tin oxide): FTO is a type of *transparent conductive films* (TCOs), which is, an electrically conductive film deposited on glass. FTO was initially chosen as substrate because of its wide use in photovoltaics and water splitting, and to obtain some preliminary data for a future, oxygen-doped TiN film with photoelectrochemical features;
- GC (glassy carbon): glassy carbon has been chosen as substrate for the depositions because of its widespread use as electrode material in electrochemistry, and because carbon is the state-of-the-art material for DMFCs.

A photo of the Pulsed Laser Deposition process is reported in the figure below, where:

- "A" represents the TiN target, whose material is ablated by the laser pulses;
- "B" is the sample holder, where the substrates on which the TiN molecules land after the ablation are arranged. The sample holder rotates during the deposition, in order to maximize the thickness uniformity of the deposited film;
- "C" is the plasma plume during its expansion: since the background gas pressure is high for the PLD process, the gas slows down the ablated particles plasma and confines the plume, which assumes a spherical-like shape.

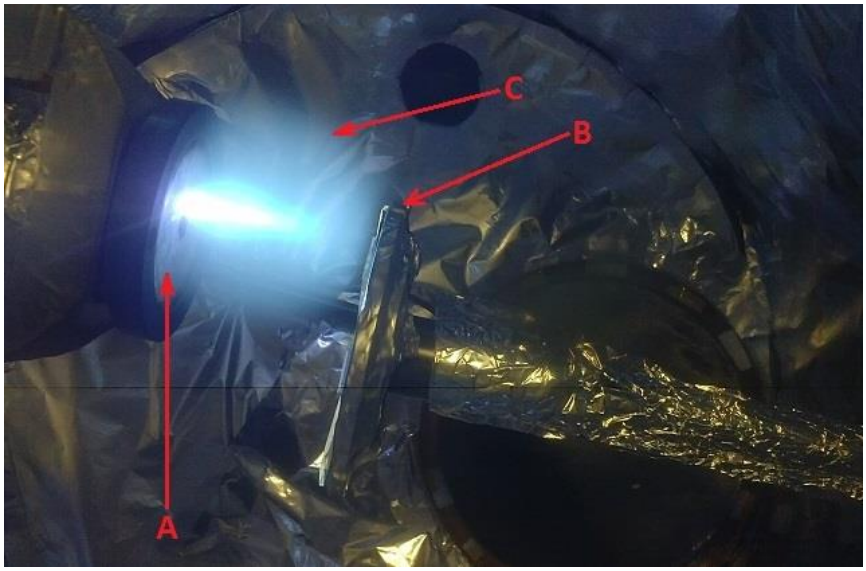

Figure 9: Pulsed Laser Deposition of the TiN scaffold

Due to the physical nature of ablation process, the TiN films deposited via PLD exhibit an amorphous nature [32]. In order to obtain an as-deposited, crystalline film with PLD it is necessary to heat the substrate while deposition is ongoing.

2.1.4. DC Sputtering

Sputtering is a PVD process in which the material is removed from a solid surface – the target – because of the momentum transfer between energetic particles (ions) and the atoms on the surface. The momentum transfer, and the removal of material, is generally obtained by a gas discharge in a confined space between two electrodes.

When ions interact with the surface, different phenomena can occur, as pictured in figure 10:

- **Reflection**: the ion is reflected and neutralized. This process is the basis of ion scattering spectroscopy;
- **Electron ejection**: the ion ejects an electron (named secondary electron) from the target;
- **Ion penetration**: this process, known as implantation, is used for selective doping of materials;
- **Structural deformation**: the ion causes structural changes in the target structure and defects in the lattice, altering the material composition;
- **Sputtering**: the ion impact originates a series of collision among the target atoms, leading to the ejection of one of those.

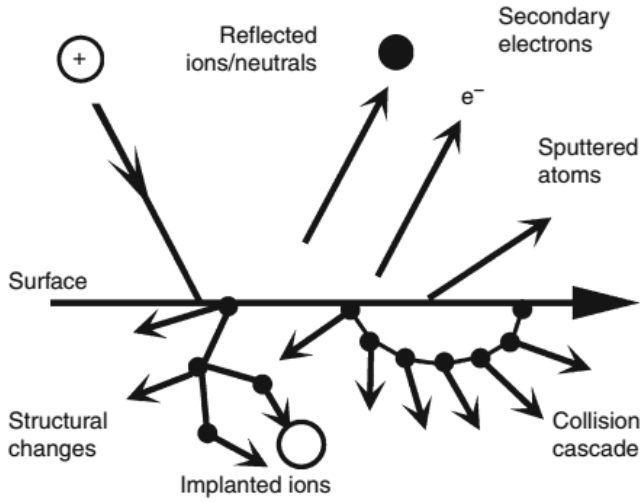

Figure 10: Phenomena occurring on a target subjected to ion bombardment [33]

The ion generation is usually obtained by applying a voltage between two electrodes, in the presence of a low-pressure gas (usually argon) in a vacuum chamber. If the voltage is delivered by continuous current, between the electrodes an electric field is formed and an electric current in the gas is generated.

The material to be sputtered is located at the target, the cathode of the electric circuit, while the substrate on which the film will be deposited is mounted on the anode, which is grounded, at a certain distance. The applied voltage determines the maximum energy that a particle escaping from the target has, while the pressure of the gas admitted into the vacuum chamber determines – along with the anode distance – how many collision can occur between the particles during their flight: these parameters influence porosity, crystalline structure and

texture of the obtained film. A schematic of a DC magnetron sputtering system is reported in figure 11.

The film formation mechanism is similar to PLD: the target material hits the substrate (in atomic or molecular form) and its atoms diffuse through the surface. The diffusing atoms can re-evaporate or find an adsorption site: in the latter case, they combine with other atoms, forming clusters acting as nucleation sites for the film.

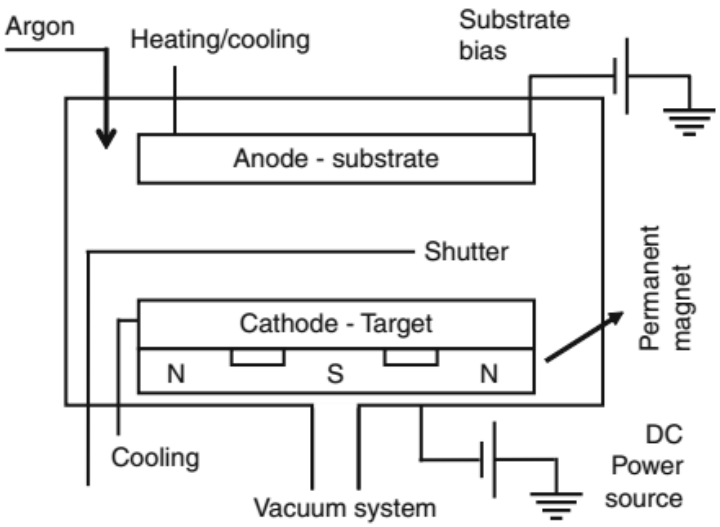

Figure 11: DC magnetron sputtering system

2.1.5. Catalyst Deposition Through D.C. Sputtering

Since D.C. Sputtering is a method that allows a precise control over the film thickness and properties, we have implemented a DC magnetron sputtering for the deposition of a Pt/Ru alloy catalyst, both without support and with the TiN support, to obtain a pure catalytic film and a multilayered TiN-Pt/Ru catalyst.

Figure 12: DC magnetron sputtering deposition.

In figure 12, a photo of a thin film deposition via DC magnetron sputtering is shown. The violet plasma of the sputtered material can be clearly seen.

2.1.6. Electrodeposition

Electrodeposition is a technique used for depositing metals on a surface, in order to form a film. It consists of an electrolyte, which contains metal ions, a substrate upon which the metal is going to be deposited and a counter electrode.

When a current flows through the electrolyte, the metal ions move towards the electrodes: the cations toward the cathode, and the anions toward the anode. The metal ions approach the Helmholtz plane of the electrode and, after a charge transfer reaction, they deposit as a metal film on the electrode. Since the deposition takes place through an electrochemical process, the total deposited mass can be linked to the quantity of electrical charge, as stated by Faraday's law.

$$m_{deposited} = \frac{Q_{deposited}}{F \cdot EPI} \cdot MM_{metal} \cdot \eta_{faradaic} \tag{2.1}$$

Equation 2.1. is used to calculate the total deposited mass. Here:

- $Q_{deposited}$, in [C], is the total charge transferred to the electrolyte;
- F is the Faraday constant, in [$C/mol_{electron}$];
- EPI is the *electron-per-ion* ratio, i.e. the number of electrons that the metal ion has to gain (or lose) in order to become a neutral atom;
- MM_{metal}, in [g/mol] is the molecular mass of the deposited material;
- $\eta_{faradaic}$ is the faradaic efficiency of the process, i.e. the portion of the total charge that is effectively used to deposit the material. This is a fundamental parameter for an electrodeposition, because part of the current is wasted in parasitic reactions, however determining it before the process is extremely difficult because of its dependence from many electrochemical parameters that the user can't control.

Electrodeposition has some advantages, which make it an efficient deposition method for metal catalysts: by simply adjusting electrochemical parameters, it's possible to control the catalyst loading and its morphology. Furthermore, it requires just the electrolyte solution, a power source and the electrodes, without any expensive equipment.

Electrodeposition techniques are categorized according to the nature of the electric field applied to the electrolyte:

- **Potentiostatic deposition**: in which the controlled parameter during the deposition is the applied potential;
- **Galvanostatic deposition**: in which the controlled parameter is the current intensity.

Even though it is possible to deposit at constant potential/current, the more common techniques in literature and in fuel cell catalyst fabrication are *pulsed*, where the potential or

current is alternated between two values, therefore the discussion will be focused on pulsed techniques.

In pulsed methods the overall potential/current signal is a series of pulses of equal amplitude and duration, separated by zero current, each one consisting of an *on-time* – during which the potential/current is applied – and an *off-time*. A typical waveform is shown in the figure below.

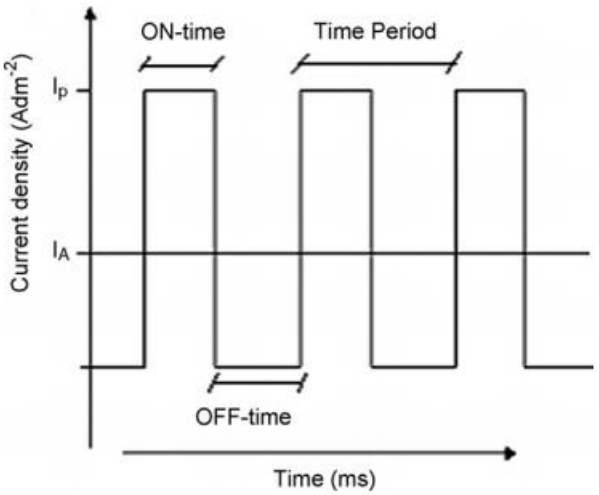

Figure 13: Waveform for a pulsed electrodeposition technique

Pulsed electrodeposition techniques have some benefits that make them fit to deposit catalyst nanoparticles:

- By modifying pulse parameters, deposits with desired composition, structure and porosity can be obtained. For catalyst nanoparticles, the on-time is generally associated with the mean diameter of the nanoparticles and the catalyst clusters: the longer the on-time, the bigger the deposited particle diameter;
- The pulsed signal allows the discharge of the negative layer formed around the cathode during the off-time of the deposition process, making the passage through it easier for the ions;
- Nucleation and crystallization of the deposited particles can be controlled by tuning the features of the on-signal and the off-signal. [34]

In this work, electrodeposition has been implemented as method for depositing the Pt catalyst nanoparticles on the TiN support film, and the influence of the total transferred charge and of the on-time signal on the performance of the electrode has been investigated.

Because of the aforementioned difficulties in evaluating the faradaic efficiency of electrodeposition, we have referred to a galvanostatic electrodeposition process reported in the literature [35], applied the method for only platinum, and different deposited charges.

2.2. Electrochemical Measurements

2.2.1. Electrochemical Experimental Setup

Experimental studies in electrochemistry deal with bulk properties of electrolytes, equilibrium and non-equilibrium electrode potentials, and the nature, kinetics and mechanism of electrochemical reactions. This latter aspect is the one of interest in this work.

Electrochemical measurements usually concern not the whole galvanic cell but one of the electrodes, the *working electrode* (WE): this is the electrode system of interested. The WE is coupled with an electrode of known potential that approaches ideal nonpolarizability, called *reference electrode* (RE), in a configuration named two-electrode cell. If the measurement involves a current flow so high that the voltage required to overcome the ohmic drop is not negligible (i.e. is more than 1-2 mV), a *counter electrode* (CE) is additionally needed, obtaining a three-electrode configuration. In this arrangement, the current is passed between the working electrode and the counter electrode.

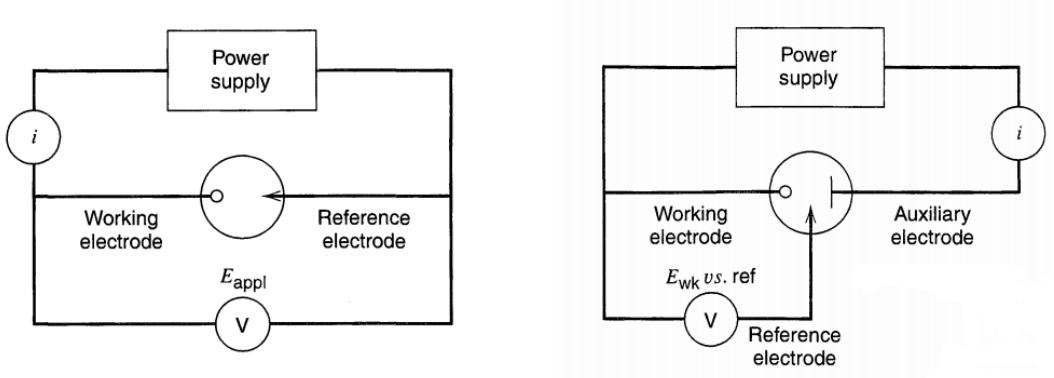

Figure 14 Two-electrode (left) and three-electrode (right) cell [2]

It is therefore necessary an electric current and/or voltage source to power the electrochemical system: this source is called *potentiostat*.

In an electrochemical experiment, you can measure the output of a cell – current or voltage – and its variation with time as a response of an excitation signal. By plotting different parameters in different ways, numerous information on the system can be obtained and many experiments can be performed.

2.2.2. Linear Sweep Voltammetry

In Linear Sweep Voltammetry (LSV) the electrode potential is varied, from a lower limit to an upper limit, at a fixed *scan rate* – that is, the speed at which the potential is varied during the experiment – and the current response of the system is plotted as a function of voltage.

LSV are performed to investigate the features of an electrochemical reaction whose equilibrium potential lies inside the voltage scan range. In figure 15, a LSV for the methanol oxidation reaction is shown.

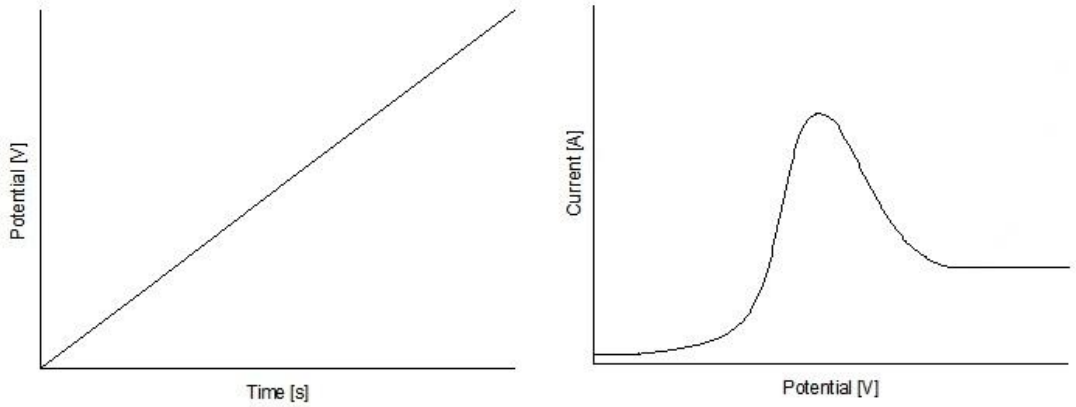

Figure 15: Potential sweep (left) & resulting current/potential curve (right) during a LSV experiment

When the scan begins from the left hand side, no current flows i.e. no reaction occurs. However, as the potential is swept to the right, current flows, it reaches a peaks and then drops. What happens is that, as the potential is swept from the initial to the final value, the equilibrium of the MOR shifts from no conversion (at the initial value) to full conversion (at the final value): as long as the electrode potential is below the equilibrium potential of the MOR, methanol is not oxidized and no current flows. As soon as the potential is above the equilibrium value oxidation takes place, with a reaction rate that grows higher as the applied potential gets bigger, and current increases steeply until the peak is reached. At this point the reaction is so fast that the flux of reactants is not fast enough to satisfy that required by the Nernst equation, and the current begins to drop.

During LSV, as well as during other sweep experiments, the potential scan rate is a very important parameter: if the scan is slow, the diffusion layer has more time to grow, the flux of reactants to the electrode is slower and the current is smaller than at faster rates.

In this work, LSV have been performed to check the activity of the fabricated materials towards the MOR: the fabricated materials were tested in a 0.5 M H_2SO_4 + 1 M CH_3OH solution and the potential was swept in order to include the potential at which MOR takes place on a Pt catalyst. Various scan rate were implemented, in particular 10 mV/s, 5 mV/s and 1 mV/s: these slow rates were chosen so that the electrode could reach an equilibrium situation and a more precise measure could be possible. For these tests, a three-electrode cell was used: as counter electrode a Pt wire was used, while as reference electrode an Ag/AgCl electrode was used.

2.2.3. Cyclic Voltammetry

Cyclic voltammetry (CV) is one of the most useful and used techniques in electrochemistry, able to rapidly provide qualitative information about electrochemical systems, from thermodynamics to kinetics.

During a CV experiment, the electrode potential is scanned linearly from an initial to a vertex value, and then the scan is reversed; the result is the electrochemical response – in terms of a potential/current plot – of the analyzed system. A typical CV scan is reported in the figure below.

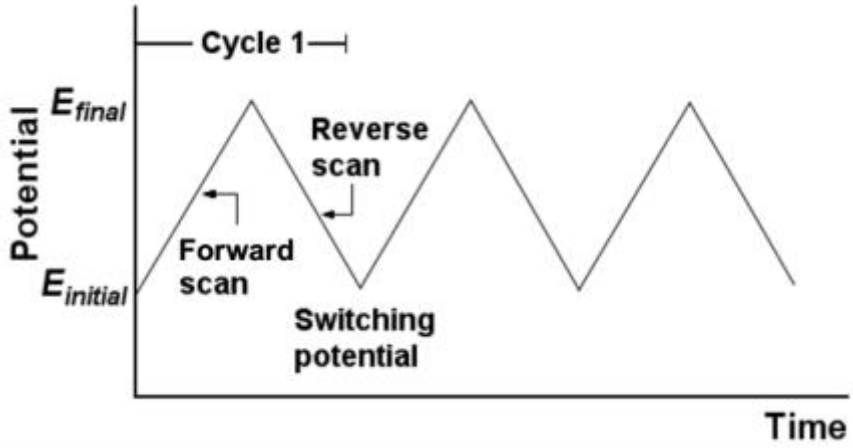

Figure 16: Potential-time signal for a CV experiment [36]

A single CV experiment has limited usefulness in characterizing the whole electrode system, while multiple CV can give lots of information, like reversible/irreversible behavior of a redox couple, rate constants, reaction mechanisms, or diffusion coefficients.

Despite its many qualities, CV have some limitations and downsides [37]:

- The underlying assumption of CV – and in general of potential sweep techniques – is that the electron transfer occurring at the interface is fast and has a negligible influence on the observed current and reactant concentration. This assumption may not always apply;
- With reactions involving adsorbed chemical intermediates, whose concentration is potential dependent, like methanol oxidation, it is still unclear how the kinetics of the elementary reaction steps involving radical intermediates relates to the sweep rate.

An archetypal potential sweep curve for a redox couple in solution is reported in the figure below and is very useful to explain the major features of a CV plot: as the potential of the working electrode is increased towards the final value, eventually a potential is reached where the current starts to increase. This means that, in the redox couple example, the potential of the redox couple has been reached, and the measured current is a function of the reaction rate and the reactants concentration, as in the previous case of the LSV. As the potential reaches the final value and ramps back again, towards the initial value, the sign of the current tends to become the opposite and the reverse current peak of the redox couple is reached.

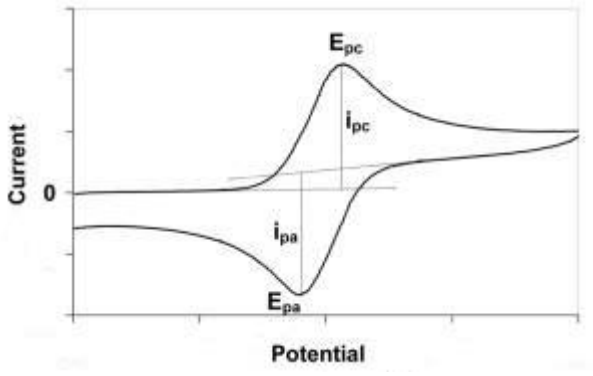

Figure 17: Typical form of a CV scan for a redox couple

CV was extensively used as analysis method during this work, because by utilizing this technique with different electrolyte solutions important information can be obtained. When the electrolyte was a 0.5 M H_2SO_4 solution, CVs have been used to:

- Test the chemical stability of the support in acid environment: a stable support doesn't exhibit any significant current peak inside the potential scan range;
- Evaluate the ECSA (Electro-Chemical Surface Area) of the deposited Pt catalyst: Pt shows peculiar features in acid environment – shown in figure 18 – that can be used to calculate the total area of the catalyst that effectively is in contact with the electrolyte solution and is therefore active.

On the other hand, when the electrolyte used was a 0.5 M H_2SO_4 + 1M CH_3OH solution, with CVs we were able to determine:

- The activity of the tested material towards the MOR;
- The resistance of the material towards CO poisoning and the kinetics of the reaction, as will be discussed further on.

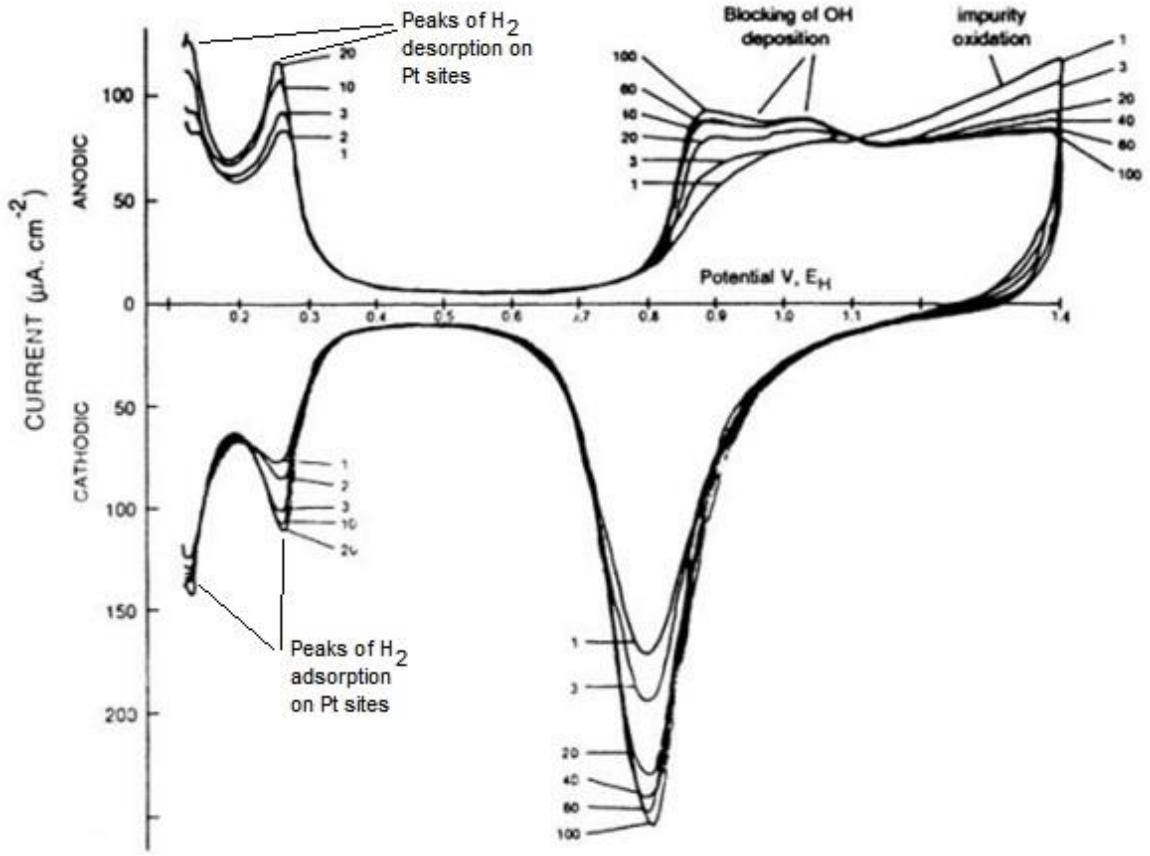

Figure 18: Typical CV plot for a Pt electrode in H2SO4 [37]. The effect of repeated scans (increasing numbers for the plots) is highlighted.

2.2.4. Electro-Chemical Surface Area

In an electrochemical reaction, the exchange current density and the Tafel slope together define the activity of a catalyst. However, since their determination for technical electrodes is difficult and affected by uncertainties, there are alternative ways of defining catalyst activity: among these, the *electro-chemical surface area* (ECSA) is a widely used parameter, because it can be derived from a simple CV experiment.

ECSA physically represents the effective surface area of the catalyst that is in contact – and therefore promotes the reaction – with the electrolyte solution, in the case of experiments with the single electrode, or with the gas-diffusion layer and the Nafion® membrane in the case of a full cell. The value obtained with the two configuration for the same catalyst is usually different, because in the full cell the three-phase contact between gas-diffusion layer, catalyst and Nafion® is not perfect and not all the catalyst is in contact with the fuel feed; other phenomena determine this difference, like re-crystallization of the catalyst during electrode testing [38], but their influence is smaller.

ECSA for a Pt catalyst can be determined using hydrogen stripping in a cyclic voltammetry, integrating the current intensity/potential curve in the hydrogen desorption region, the one

highlighted in the figure below. Operatively, from the plotted overall current density the double-layer current must be subtracted, because that is generated by a different electrochemical phenomenon.

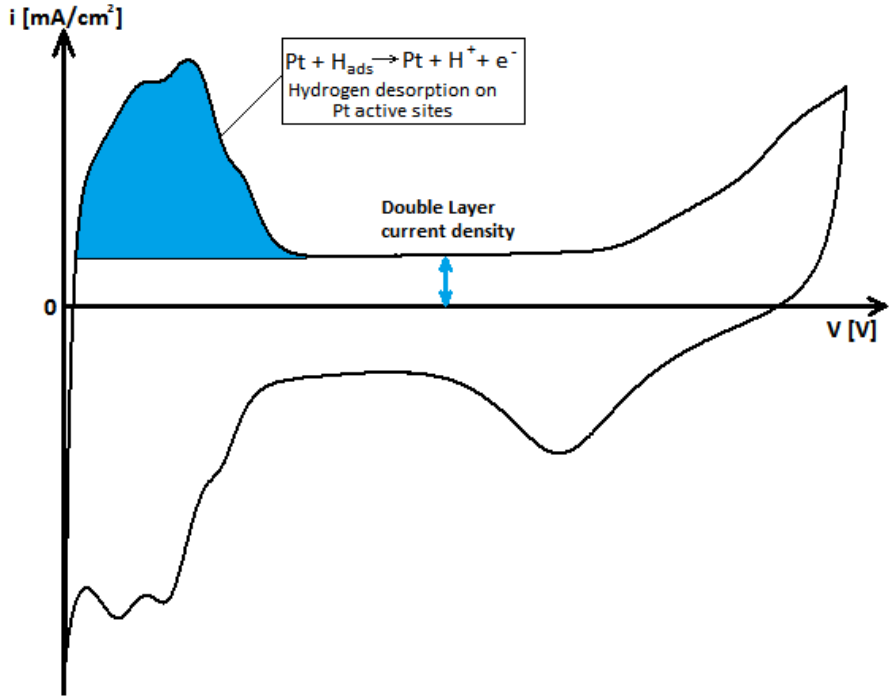

Figure 19: CV in H_2SO_4 for a Pt catalyst. The hydrogen desorption area for ECSA calculation is highlighted in cyan

ECSA can also be determined referring not the hydrogen desorption region, but the platinum oxide reduction peak in the CV scan.

The formula used for the numerical calculation using the hydrogen desorption area is as follows:

$$ECSA = \frac{Q_H}{q_h \cdot m_{Pt}} \tag{2.2}$$

Q_H is the total charge associated to the hydrogen desorption, q_h has a value of $2{,}10 \cdot 10^{-4}$ C/cm^2 and represents the total charge needed to desorb a monolayer of hydrogen from a Pt catalyst, while m_{Pt} is the total catalyst loading of the electrode.

2.3. Crystallography and Raman Spectroscopy

2.3.1. X-Ray Crystallography

X-Ray crystallography, also known as X-Ray Diffraction (XRD), is an analysis method used for identifying the molecular structure and the lattice configuration of crystal, thanks to the ability of crystalline structures to diffract x-rays into specific direction. XRD is based on Bragg's Law:

$$n\lambda = 2d \sin\theta \qquad (2.3)$$

Where θ is the diffraction angle, d is the distance between atomic layers in a crystal, λ is the wavelength of the incident x-ray and n is an integer.

XRD is widely used for many purposes: measuring the average spacing between layers of atoms, determining the orientation of a single crystal/grain, and measuring the size and shape of a crystalline region. A simplified XRD experimental setup is reported in figure 20 and consists of an x-ray source (a x-ray tube, usually) able to vary its angle θ, a sample stage and a detector. The x-ray is focused on the sample at an angle θ and the detector reads the intensity of the diffracted x-ray, received at 2θ from the source path. The incident angle is then increased over time, and the diffraction peaks at different 2θ values are recorded.

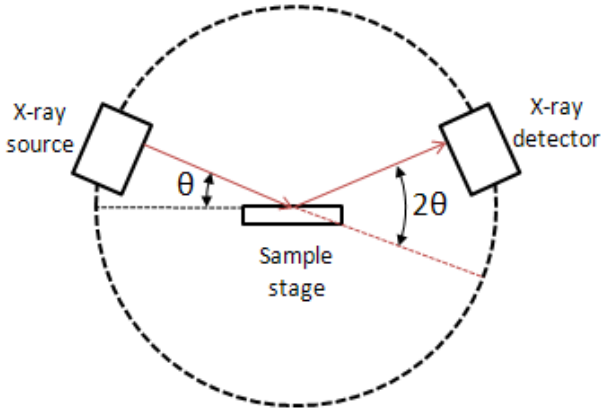

Figure 20: schematics of an XRD experimental setup

In the analysis of a XRD spectrum, three parameters give extensive information on the crystal:

- **Peak position**: the 2θ position of the peak is used to determine the molecular composition of the crystal, i.e. the material it is composed of. Moreover, a peak shifted to different angles – with respect to the "reference" position – can be a sign of a uniform strain in the lattice;
- **Peak width**: the peak width at half maximum is used to measure the crystalline grain size;
- **Peak intensity**: the peak intensity is related to the crystalline grain size.

During our study, XRD was employed to identify the crystalline structure of the fabricated materials and to investigate potential phase transformations due to thermal annealing or electrochemical testing. In particular, XRD was used to:

- Determine the crystalline structure and the molecular composition of the TiN scaffold right after the deposition and analyze the changes after thermal annealing;
- Determine the structure of the TiN/Pt catalyst right after the electrodeposition process, and determine how electrochemical testing influences the morphology of the catalyst.

In order to determine the crystalline size of the analyzed materials, the Scherrer equation – which relates the size of sub-micrometer crystals to the geometric features of peaks of an x-ray diffraction pattern – is used [39]:

$$D = \frac{K\lambda}{\beta \cos\theta} \tag{2.4}$$

Where:

- D is the mean crystalline size, which may be smaller or equal to the actual grain size;
- K is the dimensionless *crystallite shape factor*, whose value ranges from ~0,84 to 1;
- λ is the incident x-ray wavelength;
- B (in degrees or radians) is the peak width at half the maximum intensity;
- θ (in degrees or radians) is the Bragg angle.

2.3.2. Raman Spectroscopy

Raman spectroscopy is a technique used to identify the molecular composition of non-metallic materials, relying on a form of inelastic photon scattering called anti-Stokes Raman scattering.

The Raman scattering occurs when an electromagnetic radiation interacts with a molecule, exciting the polarizable electron density and, therefore, the bonds of the analyzed molecule. When a photon interacts with the material, it excites its molecules: the single molecule, interacting with the photon, "jumps" from a "standard" vibrational energy state to a so-called *virtual energy state* for a very short period of time, before jumping back to the vibrational energy state – but with different energy in comparison with the original one – and scattering inelastically a photon. For the total energy of the system to remain balanced, the energetic change in the vibrational energy must be balanced and the scattered photon will have a different frequency (i.e. energy) than the incident one:

- If the final vibrational state has more energy than the initial one, the photon will be shifted to a lower frequency. This is called *Stokes shift*;
- If the final state has less energy than the original one, the photon will be shifted to higher frequency creating an *anti-Stokes Raman shift*. Raman spectroscopy uses this anti-Stokes shift to obtain information on materials.

The frequency-shifted scattered photons are collected with a sensor and, according to the magnitude of the shift, different molecular bonds – and therefore different materials – can be identified, because every molecule has a precise Raman fingerprint. Raman shifts are typically reported in wavenumbers, which have units of inverse length, because this value is directly related to energy (being inversely proportional to frequency)

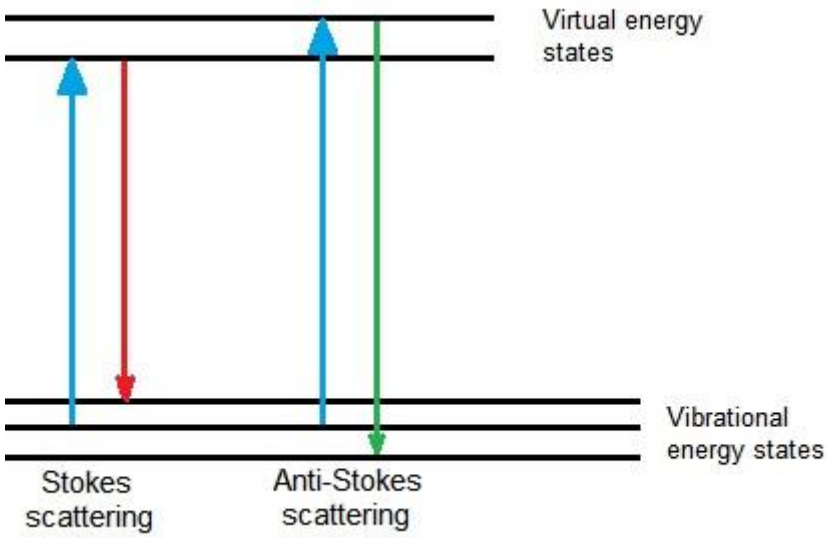

Figure 21: Energy states involved in Raman scattering

It's important to note that Raman analysis shows no result for metals, because for them vibration can't be activated and consequently no shift (Stokes nor anti-Stokes) can be observed.

For this study Raman spectroscopy was used as a tool of quick and qualitative analysis to identify the molecular composition of the TiN support film, as a complementary method to X-ray diffraction. As metals have no Raman signal, it wasn't possible to analyze the TiN/Pt catalyst with this technique.

Chapter 3

Fabrication and Characterization of TiN Scaffold

3.1. TiN Scaffold Fabrication via Pulsed Laser Deposition

The first objective of the work is to fabricate a TiN scaffold via Pulsed Laser Deposition and optimize the deposition parameters in order to obtain a film that guarantees the following features:

- **High specific area** and high porosity, in order to maximize the contact between scaffold and electrolyte. This way the deposition of Pt can be more effective, that is, the catalyst particles can be deposited with homogeneous dispersion on the TiN structure in order to achieve a high catalyst active area;
- **Good** chemical and mechanical **stability**: the TiN film must be stable in acidic environment over a wide potential range and should possess an acceptable mechanical resistance to manipulation.

As discussed in section 2.1.2, by modifying the process gas pressure during deposition it's possible to alter the kinetic energy of the ablated particles and therefore the morphology and properties of the deposited film. Generally, if the process pressure is high more porous, nanotree-like structures with high surface are can be obtained, while for low process pressures the fabricated film is more compact and exhibits a better resistance, even though the porosity and the surface area are lower. Another feature of the PLD is that the as deposited structures exhibit an amorphous structure [32]: in order to obtain a crystalline, as deposited film, it is necessary to heat the substrate at high temperature or to anneal the material after the deposition. The amorphous-crystalline solid transition introduces another factor that modifies the structural properties, i.e. the porosity, surface area and mechanical resistance, of the material.

At this point, a disclaimer is necessary: since different process gas pressures lead to film with different morphology and since the annealing of the material after the deposition introduces another variable that influences the structure of the film, by combining these two parameters – gas pressure and annealing – countless materials with different physical properties can be obtain, with the same atomic composition. Since the time was limited for this work, a systematic study of the whole set of films is not possible and falls outside the goal of this thesis. The objective of this thesis is, instead, finding a PLD process that can be coupled with the electrodeposition of a catalyst, in order to obtain a "proof-of-concept" support+catalyst material to be exhaustively studied and characterized in future works.

Because no deposition procedure is available for TiN nanostructures fabrication through PLD, identifying a promising titanium nitride nanostructure for catalyst support is carried out through a scan of different process pressures.

3.2. Process Gas Pressure Scan for TiN Deposition

TiN films are deposited from a TiN target (99,5%; Testbourne) that is ablated with a KrF excimer laser (wavelength: 248 nm, repetition rate: 20 Hz) within a vacuum chamber (base vacuum in the order of 10^{-3} Pa) filled with N_2 background gas (99,9995%) up to the different working pressures. The films are deposited on different substrates: fluorine-doped tin oxide (FTO) and glassy carbon.

The analyzed pressures during this scan are 30 Pa, 40 Pa, 50 Pa, 60 Pa and 80 Pa: they have been chosen to have a broad indication of the different morphologies that can be obtained with PLD without multiplying excessively the samples. This method has been chosen because for every process gas pressure two configurations are studied: **as deposited** film (indicated by the AD prefix), and **annealed** film (indicated by the AN prefix). The annealing conditions for TiN are kept constant during the whole work, and are:

- Annealing at 500°C, to trigger the crystallization of the amorphous, as deposited TiN film;
- Dwelling for 4 hours, so that the whole structure can reorganize and accommodate possible stresses generated during deposition and thermal treatment;
- Annealing in vacuum (in the order of 10^{-3} Pa) to avoid the exposure of TiN to oxygen and the formation of undesired titanium oxide and oxynitride.

The first analysis for the TiN films is carried out in a qualitative way, using SEM (Scanning Electron Microscope) images: an extensive analysis of the whole set of samples would be too time-consuming, therefore the first study is not in-depth but qualitative, based on previous experience in the field of PLD nanostructures.

3.2.1. As Deposited TiN Films

After the deposition, the pristine TiN films fabricated with different process gas pressures are qualitatively analyzed using SEM top views of the nanostructures. In figure 22, the top views are compared to highlight the influence on morphology of the deposition pressure.

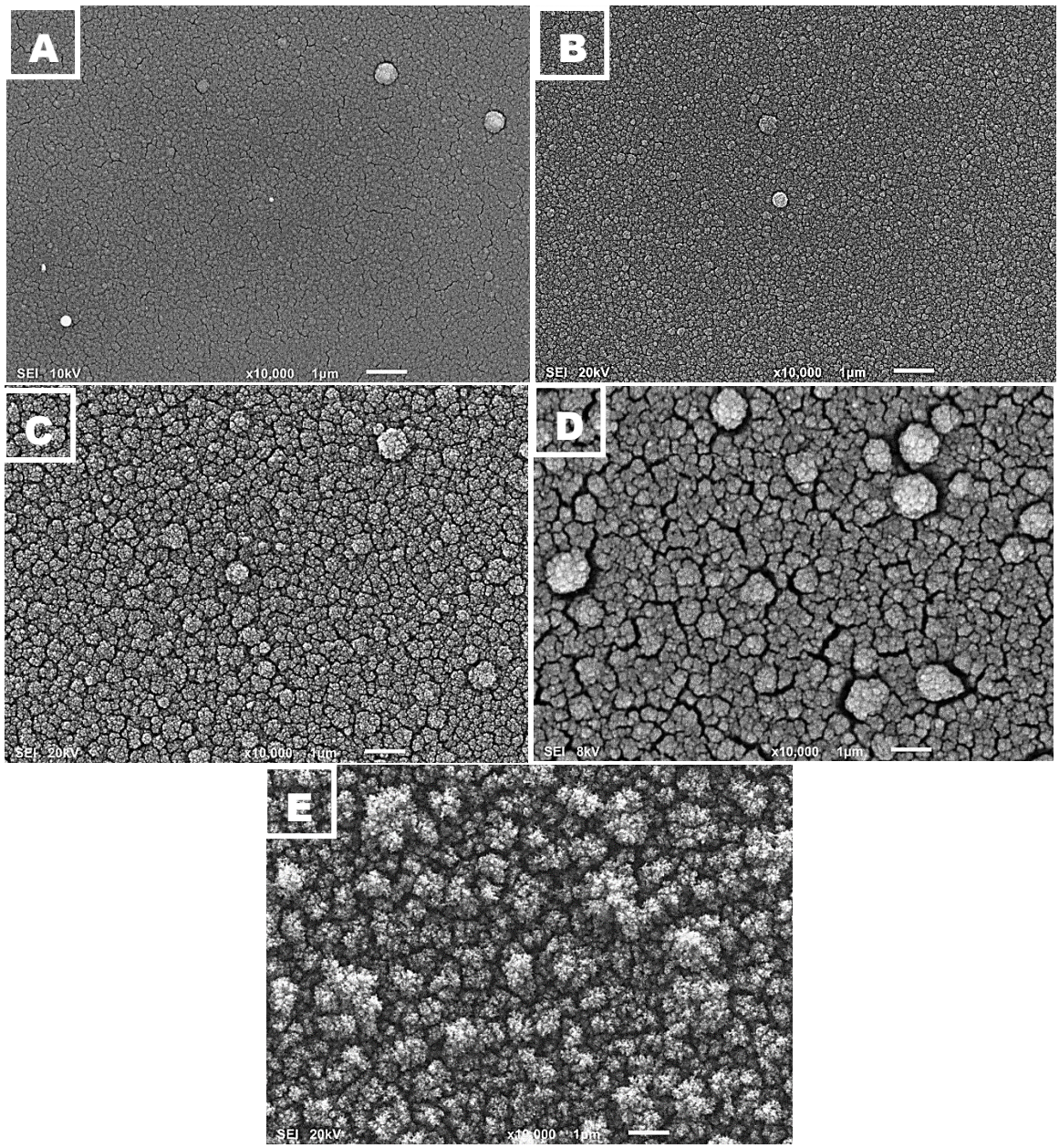

Figure 22: SEM top views for the as deposited TiN samples. A: AD-TiN 30 Pa, B: AD-TiN 40 Pa, C: AD-TiN 50 Pa, D: AD-TiN 60 Pa, E: AD-TiN 80 Pa

Comparing the SEM images a clear trend is spotted: as already mentioned in section 2.1, by increasing the process gas pressure the porosity and surface area of the film increases.

For this scan, we see that AD-TiN30 (the deposition pressure, in Pa, is indicated as a suffix number following "TiN" in the sample nomenclature) and AD-TiN40 exhibit a compact morphology, with the nanostructure organized in assemblies composed of many nanotrees. AD-TiN50 and AD-TiN60, instead, are more porous, with an evident increase in surface area: it is possible to discern, emerging from the nanostructure assembly, the tip of the single nanotrees that are also more spaced, with thicker voids appearing on the film. The same trend applies for AD-TiN80, which displays the highest porosity of all: from the top view, massively

branched nanostructures can be spotted, with higher surface/volume ratio and more voids between the single nanotrees. All these features indicate a very high porosity for AD-TiN80.

3.2.2. Annealed TiN films

The same morphological analysis procedure employed for the as deposited samples is carried out after annealing the films at 500°C. With annealing, a change in the crystalline structure of the material is expected, because the high temperature triggers the crystallization of TiN. Moreover, with annealing, the amorphous structure of the film densifies with an increase in porosity and surface area, as reported in [40] for PLD titanium dioxide films.

The SEM top view images for the annealed TiN films are reported in figure 20, to understand how annealing affects the morphology of the different TiN nanostructures and how the porosity changes.

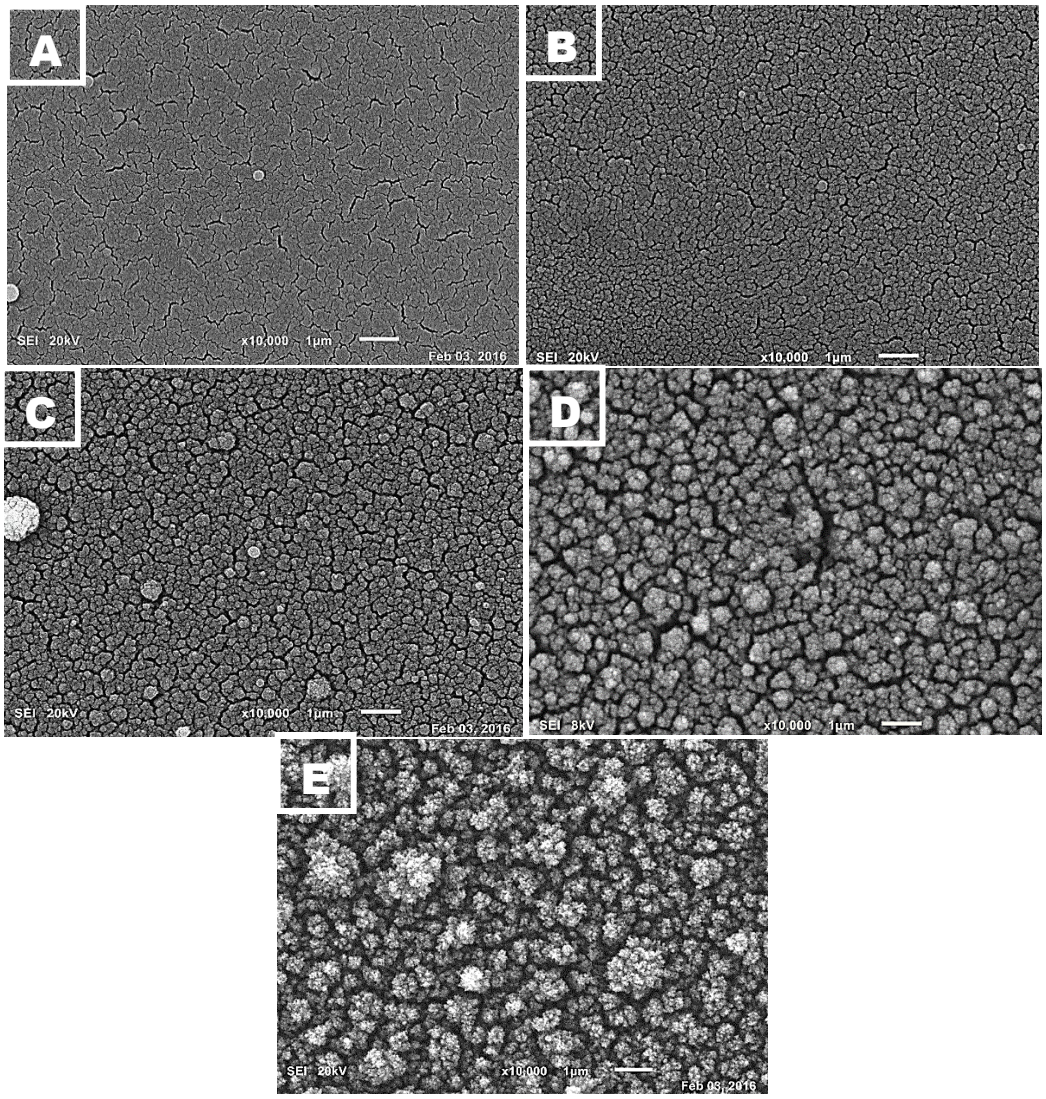

Figure 23: SEM top views for the annealed TiN samples. A: AN-TiN30, B: AN- TiN40, C: AN-TiN50, D: AN-TiN60, E: AN-TiN80

The observed effect is consistent with what is reported in the literature [40], and it is the same for all different deposition pressures: the morphological change takes place, with an increase in the film porosity and surface area, with more voids appearing on the surface and a bigger spacing of the single nanotrees. The effect is more pronounced for the low-pressure films, while for higher pressure like 80 Pa the porosity increase is less prominent.

After the quick morphological analysis of the various films, some considerations can be made: as previously stated, the following considerations are qualitative and non-exhaustive and they don't give indications about all of the structural features of the different nanostructures. However, since the complete physical characterization of the PLD TiN films is not the scope of this thesis work, and since a comprehensive study would be time-consuming, they are accepted under the perspective of demonstrate the possibility of creating a TiN-supported catalyst:

- TiN30 and TiN40, both as deposited and annealed, despite showing a good mechanical resistance to manipulation, have a too compact nanostructure: this would be an obstable for mass transport of reactants to the catalyst active sites, resulting in an inefficient catalyst. Considering this phenomenon, using these nanostructures as supports for electrodeposition and MOR is unfeasible;
- TiN80 shows, from the SEM images, the best surface area and a very high porosity. These two features should lead to a catalyst support with good performance, with high active area for the desired reaction to take place: therefore, TiN80 would be an ideal candidate as support during electrodeposition. However, this film shows no mechanical resistance, both as deposited and annealed, upon manipulation, because it delaminates when handled. For this reason, it is discarded as catalytic support for the electrodeposition of platinum;
- TiN50 and TiN60 seem to satisfy both requirements for an efficient catalyst support: from the SEM images, high porosity can be seen and the mechanical resistance upon manipulation is good. For both supports, TiN nanotrees with a medium tip width of 100-200 nm can be observed and, thanks to the many cracks and voids in the surface, no assembly of TiN nanostructures is observed. These basic observation hints at a porous, high-surface area scaffold with advantageous morphology for a catalytic support. It should be noted that even after thermal treatment, from the SEM top view images the porosity of TiN60 is bigger than the one of TiN50, thanks to the increased spacing between the nanotrees.

Because of these loose consideration about nanostructures and morphology, TiN50 and TiN60 are chosen as catalyst supports during electrodeposition: consequently, they undergo a more precise and specific physical and electrochemical characterization, in order to verify the accuracy of the undetailed analysis performed.

3.3. Physical Characterization of TiN50 and TiN60

Physical characterization for TiN50 and TiN60 is carried out through Raman spectroscopy and XRD analysis: combining the two methods, precise information about the structure (amorphous or crystalline) and the molecular composition of the film can be obtained. Firstly, cross-section SEM images of the two supports, both as deposited and annealed, are presented in figure 24.

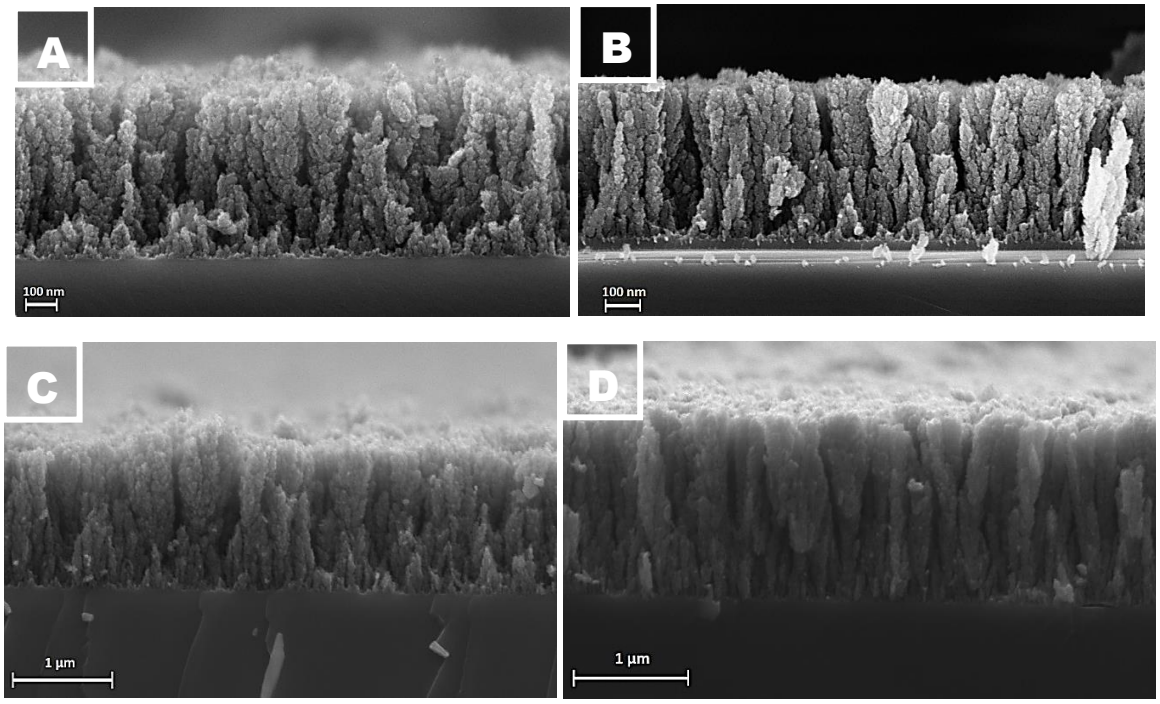

Figure 24: SEM cross-section for A: AD-TiN50, B: AN-TiN50, C: AD-TiN60, D: AN-TiN60

The morphology variation observed from the cross-section images agree with the previous consideration made from the top views: TiN50 and TiN60, both as deposited and annealed, share a similar nanostructure with good surface area, spaced nanotrees and interesting porosity. With annealing a densification and crystallization of the film is observed, as can be seen from the size difference in the grains of the nanostructure; the reorganization of the structure with annealing is confirmed by the change in the film thickness – and consequently in the length/width ratio – with thermal treatment.

AD-TiN50 and AD-TiN60 films are composed of many nanostructures with a tree-like appearance and some small branches that detaches and grow from the “central body” of the structure. After thermal treatment, an increase in the film surface area can be seen, because the tips of the nanotrees are more separated in comparison to the as deposited film. Moreover, the nanotrees change their structure to a more “column-like” one, with fewer branches than before. This change in structure is followed by a growth of the film, with a length increase of approximately 20% for both TiN50 and TiN60, while the width of the nanotrees remains unchanged, due to the previously-mention crystallization of the TiN film. In table 2, the geometrical parameters for the nanostructures are briefly reported.

	AD – L/D ratio	AN – L/D ratio	Length increase
TiN50 & TiN60	~7,5	~6,5	~20%

Table 2: Geometrical parameters for TiN50&TiN60

The high length/width ratio (L/D ratio) makes it possible to approximate the nanotrees to quasi-1D structures, which could be very useful in enhancing the performance of a fuel cell electrode: in a quasi-1D structure, in theory, the electrons move from the catalyst (which harvests them) to the electron-conducting material in a preferential path with high efficiency.

A Raman analysis is then performed on the scaffolds, to determine the molecular composition of the films. The results are reported in the following figures.

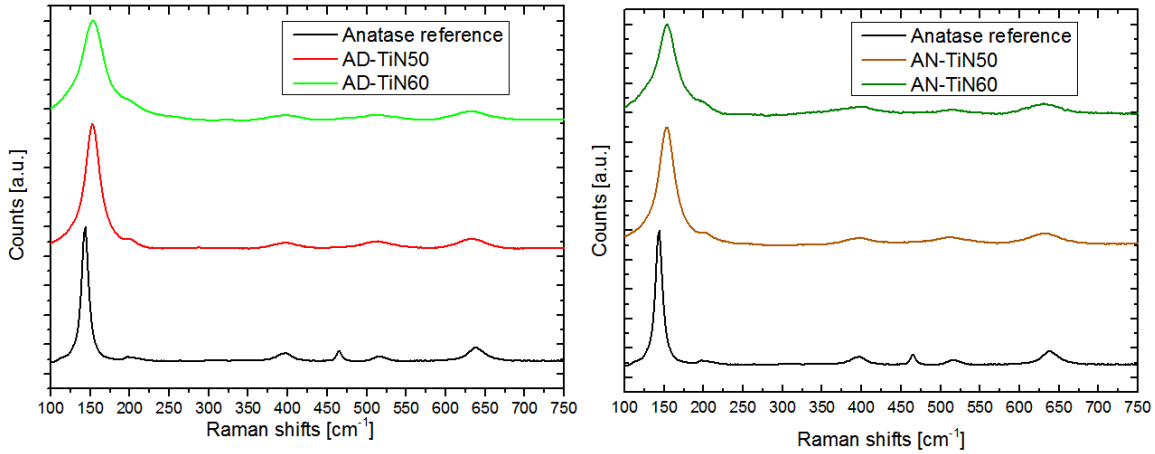

Figure 25: Raman spectra for as deposited (left) and annealed (right) TiN50 & TiN60. Anatase reference plotted

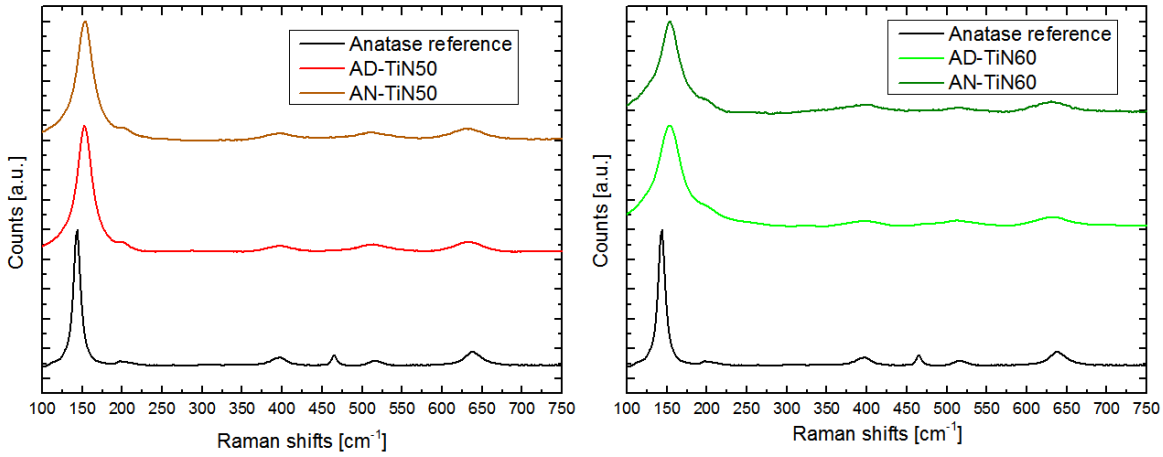

Figure 26: Raman spectra for TiN50 (left) and TiN60 (right). Anatase reference plotted

Figure 25 compares the spectra of the film deposited with different process gas pressures, both before and after annealing, to investigate the influence of process gas pressure on the composition of the film. As expected, modifying the gas pressure during pulsed laser deposition only the morphology of the film changes, while the composition remains constant. Figure 26, on the other hand, is reported to highlight how annealing influences the nanostructure for

TiN50 and TiN60: we expect that with annealing and consequent crystallization the intensity of the various peaks changes, corresponding to changes in the film structure. As another reference, the Raman peaks for TiN and TiON are reported in table 3.

Material	Raman Peaks [cm^{-1}]
TiN	242, 610 [41]
TiON	200, 400, 518, 640 [42]

Table 3:TiN & TiON reference Raman peaks

The analysis of the Raman spectra shows unusual and unexpected behavior for the TiN films:

- The spectra of all samples is almost identical to the anatase TiO_2 reference: no peak can be attributed to TiN, since no feature is observed at 242 cm^{-1} nor at 610 cm^{-1}, while the peaks at ~517 cm^{-1} and ~630 cm^{-1} can be attributed to TiON or TiO_2. These spectra should indicate that the deposited films are not made of TiN but instead of anatase TiO_2, which is an inconclusive result since the films are deposited from a TiN target;
- Annealing the film doesn't change at all its structure: the comparison between as deposited and annealed samples (figure 23) shows that the intensity of the various peaks – related to the quantity of material that diffract the Raman radiation at that precise Raman shift – doesn't change. That is, the film doesn't change its structure with thermal treatment. This conclusion is contradictory with the previous theoretical knowledge and the crystalline reorganization of the TiN film observed with SEM images (figure 24).

Further investigation of this behavior is carried out through XRD analysis, whose results are reported in figure 27. In the upper part of the figure, the influence of the deposition pressure on the crystalline structure is reported, while in the lower part the influence of annealing upon the structure is investigated.

In the XRD spectra, the TiN reference peaks are plotted, while the first peak at 25° is the main anatase peak. This data confirms the presence of anatase titanium dioxide in the TiN film, as was inferred from the Raman analysis. XRD also confirm the unexpected behavior that emerged from the Raman spectra: as previously stated in sections 2.1. and 3.1, PLD films have amorphous structure and, therefore, should have no XRD signal: however, the as deposited TiN films here analyzed show XRD peaks already after deposition, in contrast with the literature. Moreover, with annealing no change in the crystalline structure is observed from the XRD spectra, which is still in contrast with previous literature studies [32].

These considerations make also the XRD analysis of the film inconclusive and inconsistent with previous literature studies, invalidating completely the physical characterization of the TiN films.

This unexpected result is actually due to fabrication problems that affect the film during the deposition: after successive tests, it has been discovered that the laser used for TiN deposition presents a disuniformity in the spot, leading to an anomalous ablation of the target.

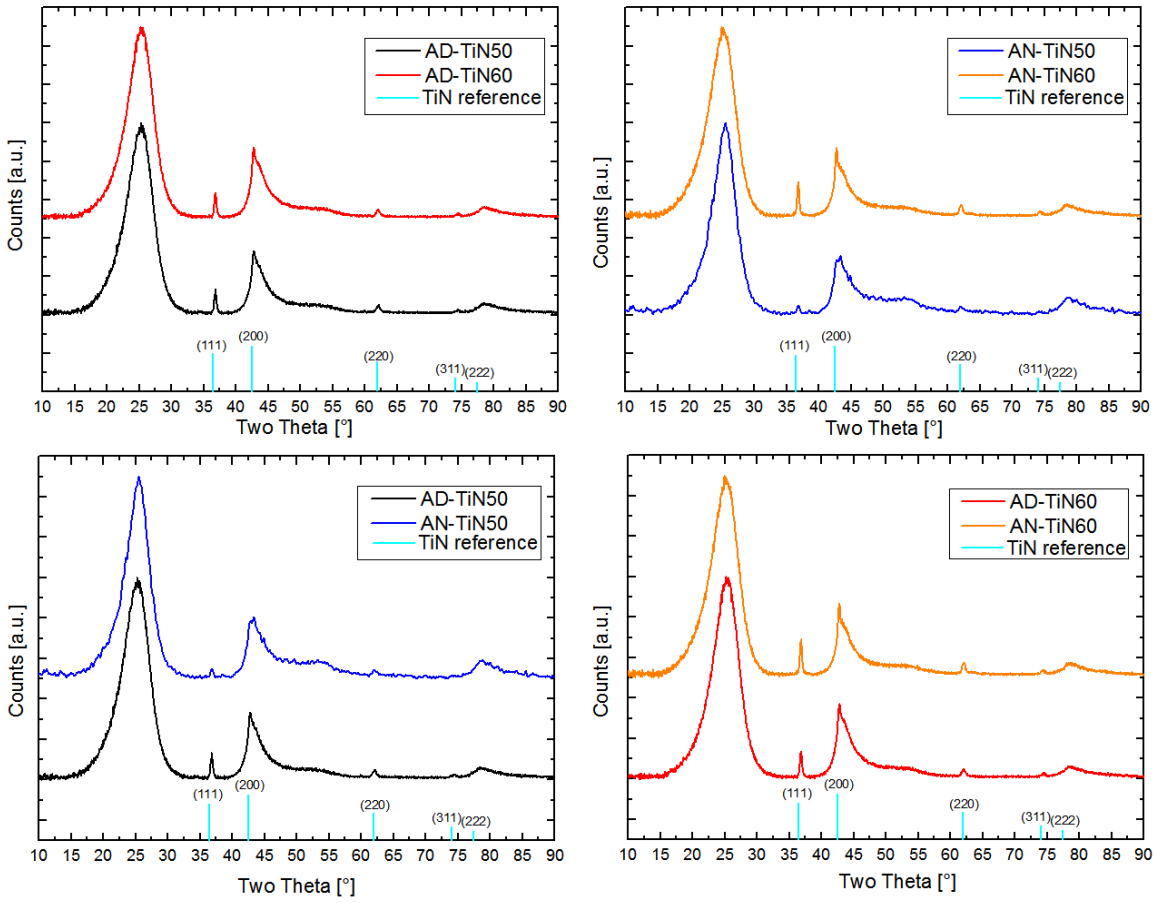

Figure 27: XRD spectra comparison for TiN50 and TiN60. TiN reference XRD peaks are reported

A disuniformity in the laser spot means a disuniformity in the heat profile on the target during the ablation process: where the heat is smaller, the laser pulse is not able to ionize the particles but instead it heats up the target material, which undergoes rapid crystallization. These crystalline molecules are then physically separated from the target without ionizing, and lastly land on the substrate as a crystalline phase. The anatase TiO_2 contamination is probably due to the scarce purity (99,95%) of the TiN target itself. This, combined with the oxygen contaminations that are present in the process gas (N_2 99,9995%) are responsible for the oxidation of the titanium of the target to titanium oxide, a process that probably takes place during the plasma plume expansion: the plume is a highly reactive environment where many radicals, which fastly react with titanium, are present.

This hypothesis is confirmed by SEM investigation of the as deposited TiN films, as shown in figure 28, with a mean droplet diameter of 10-15 µm.

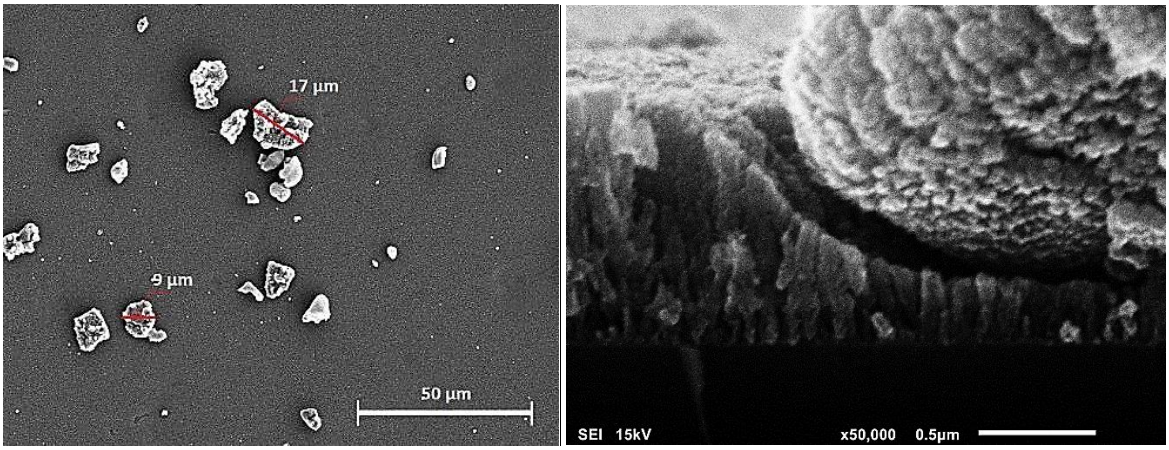

Figure 28 Left: SEM top view of droplets deposited on top of the TiN film. Right: close-up of a droplet crushing the TiN film

The presence of droplets explains the contradictory results obtain with Raman and XRD analysis, particularly regarding the crystalline nature of the amorphous film: during XRD, what is analyzed is not the film itself, but the film and the crystalline droplets.

The presence of these droplets is a big problem for the overall efficiency of the TiN scaffold, because having these micron-sized defects on top of the nanostructures decreases the surface area of the material and blocks the entrance between the nanostructures for the Pt catalyst deposition: the consequence is a non-negligible loss of electrochemical active area, generated current and power.

Various methods are tested to eliminate this problem, from a fine-tuning of the laser spot to a short potential cycling in acidic media as a pre-treatment for the film in hope of eliminating the droplets, but while the number of defects decreases, none of the methods is able to completely eliminate the problem. Therefore, all the films that will be tested from here on will be affected by this problem.

In a future optimization of the TiN film and of the catalyst, other methods will be tested in order to fully eliminate the droplet problem: using a purer TiN target to deposit the TiN film, employing a purer N_2 process gas, analyzing thoroughly the film composition through XPS.

3.4. Electrochemical Characterization of TiN50 & TiN60

Along with the physical characterization of the film, an electrochemical study of the TiN scaffold is performed: since the morphology of the scaffold is potentially favorable for the electrodeposition of the Pt catalyst, this feature is useless if the support itself is not stable in the acid anodic environment of a DMFC. Therefore, extensive cyclic voltammetry test are performed on AD- and AN-TiN50 and TiN60, not only to test the long-time stability after repeated cycles but also the chemical inert nature of the material – that is, no current peaks must be seen.

It is important to stress that from this point on, all of the fabricated films, both annealed and as deposited, will have a fixed, constant length of 1 µm. Since this feature is common to all films, this won't be included in the nomenclature of the samples.

For the electrochemical testing, the following protocol is employed:

- Cyclic voltammograms in 0.5 M H_2SO_4 solution. Three consecutive CV cycles, from 0 V to 1,3 V with a scan rate of 150 mV/s, are performed: the first is composed of 10 scans, while the other two of 50 scans. The potential range is chosen in order to study the behavior of TiN on a wide spectrum. The last scan of each cycle – i.e. the 10th, 60th and 110th scan – is then plotted;
- Cyclic voltammograms in 0.5 M H_2SO_4 + 1 M CH_3OH solution. The same cycles and scan rate are adopted, while the potential range here is narrower, from 0,1 V to 1 V. The last scan of each cycle is then plotted. These voltammograms are performed to confirm the inactivity of the bare TiN support towards methanol oxidation, as reported in [24].

Firstly, the CV plots for the as deposited TiN are reported.

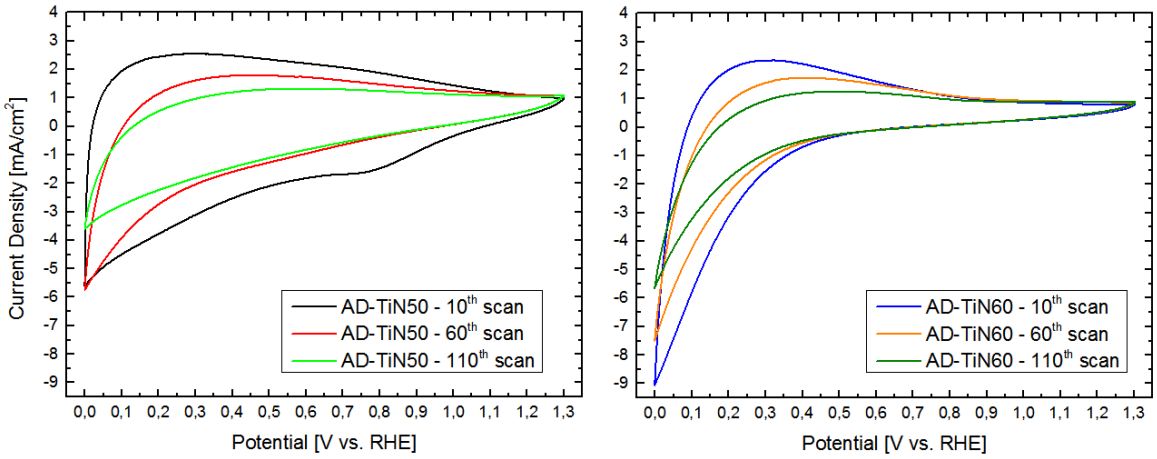

Figure 29: CV comparison for AD-TiN50 (left) and AD-TiN60 (right). Electrolyte: 0.5 M H_2SO_4. Scan rate: 150 mV/s

Both films are not stable in acidic condition: after a steady-state-like situation is reached, i.e. after the 10th cycle, the same behavior can be seen for AD-TiN50 and AD-TiN60. At low potential, the decrease of the reduction current that takes place indicate that a chemical reaction is occurring between the electrolyte and the TiN film. This reaction is due to the transfer of H^+ ions between the electrolyte and the TiN film and it's not caused by the HER (hydrogen evolution reaction) $H_2O \rightarrow \frac{1}{2}O_2 + 2H^+$. If hydrogen was evolved, when reversing the potential from 0 V to higher values, the curve would be much steeper; in this case, apart from the first cycles during which the film is still stabilizing, the slope is instead pronounced, a feature that doesn't belong to the HER. The macroscopic effect of this transfer is still unclear, but three hypotheses are made:

- At low potential the transfer of H^+ ions causes the hydriding of the TiN support: what happens is that hydrogen is adsorbed on the film and, while part is desorbed (reversing the scan from 0,1 V to higher values), other part interacts with TiN to form titanium hydride.

Since this compound is not conductive, applying a voltage to it yields no effect: this would explain the narrowing and the closing of the CV plot at potentials higher than 0,5 V;

- The transfer of H^+ ions causes the hydroxylation of TiN: during the potential sweeping, in the acidic environment TiN forms a basic oxide compound that transforms later into titanium hydroxide. The result is the same as titanium hydride: titanium hydroxide is not conductive and, when a voltage is applied, no effect is recorder and the CV plot becomes narrow;
- H^+ ions intercalate in the TiN film, generating an electro-chromic effect on the TiN film: at low potentials, we see that TiN changes color – from goldish/brown to green – indicating a change in chemical composition caused by the intercalation (corresponding to the reduction peak at ~0 V). The corresponding oxidation peak is attributed to the irreversible de-intercalation of the same ions.

The same testing is repeated for AN-TiN50 and AN-TiN60, and the results are plotted below.

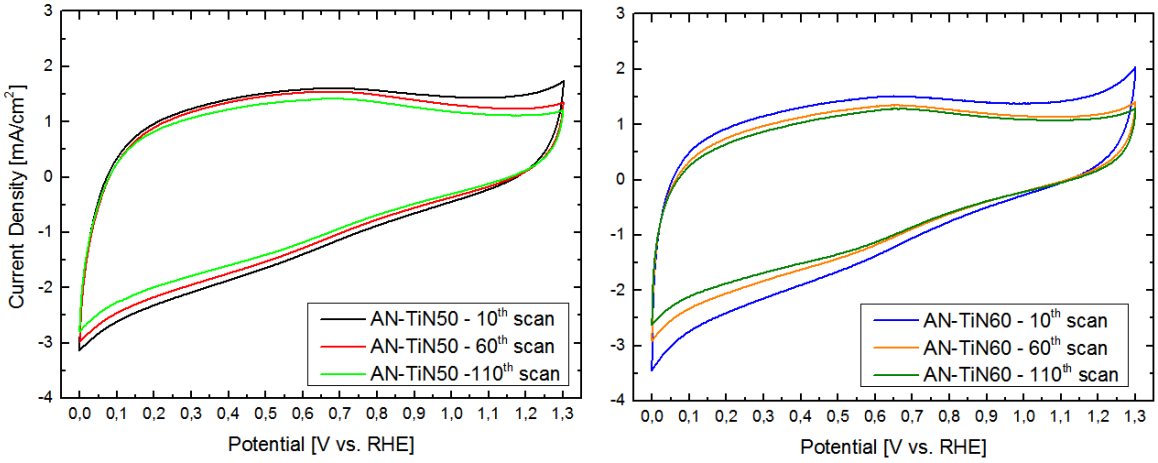

Figure 30: CV comparison for AN-TiN50 (left) and AN-TiN60 (right). Electrolyte: 0.5 M H_2SO_4. Scan rate: 150 mV/s

The difference with the CV scans plotted in figure 29 is evident: with annealing the film exhibits an enhanced stability during cycling over the wide potential range scanned, with no significant decrease in current after 110 CV scans, a sign of an increased stability of the TiN support. At 1,3 V the onset of the ORR can be spotted, since the oxidation current increases, while at 0 V the onset of the HER is present. At 0,6 V a current peak, both in oxidation and reduction regions, is present: this peak is attributed not to TiN but, instead, to a carbon compound, more precisely a quinone compound (characterized by the –C(=O)– bond).

Since this feature is absent in the CV scans for AD-TiN50 and AD-TiN60, we conclude that carbon is a contaminant introduced during annealing.

Since no peaks can be attributed to TiN, the AN-TiN50 and AN-TiN60 sample are chemically inert in acidic environment during potential sweeping. Moreover, the CVs in figure 30 have a rectangular-like shape, with non-negligible double layer current, and a steep change in the current direction when the potential scan is reversed: this behavior resembles that of a capacitor, and the high double layer current is for now attributed to the combined effect of carbon and TiN. It can be further noted that since a high voltage range is chosen for testing the

stability of the TiN film, the annealed titanium nitride shows a good chemical stability at high potential, which is similar to the working potential of a DMFC cathode: this could lead to a future implementation of the TiN films as support for cathode catalyst.

Lastly, the 110th CV scans for as deposited and annealed films are compared, to highlight the different chemical behavior when a stabilized electrochemical condition for the film in acidic media is reached, i.e. when there is no transient effects like oxidation of impurities or other reactions.

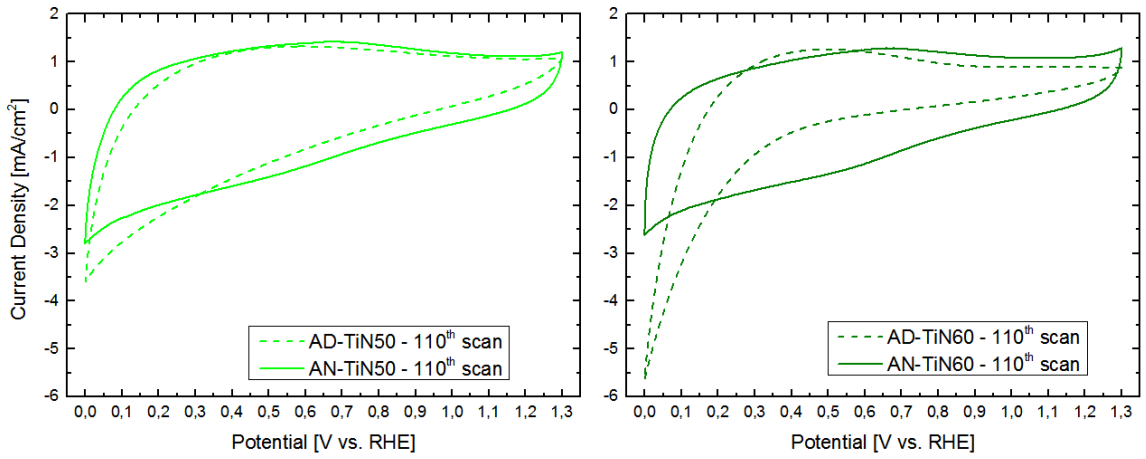

Figure 31: Comparison between as deposited and annealed TiN film. Left: AD-TiN50 vs AN-TiN50. Right: AD-TiN60 vs AN-TiN60. Electrolyte: 0.5 M H_2SO_4. Scan rate: 150 mV/s

Despite the AD-TiN and AN-TiN films exhibit peak oxidation current density of roughly the same magnitude, with this comparison the instability of the AD-TiN films is more evident. Considering a future DMFC application, the chemical reaction taking place on AD-TiN and the loss of conductivity at high voltage are features that hinders its implementation as catalytic support. Moreover, the observed decrease in current density through cycling corresponds to a delamination of the film during testing: after the CVs are performed, part of the film detaches due to the acidic environment.

On the other hand, AN-TiN films exhibit better chemical stability and inert nature through all the swept potential range and throughout the extensive cycling, both beneficial features for a catalyst support: these features are associated with a good mechanical stability of the nanostructure, which does not delaminate or shows macroscopic signs of mechanical failure after electrochemical testing.

Both AD-TiN50 and AN-TiN50 undergo a final cyclic voltammetry in 0.5 M H_2SO_4 + 1 M CH_3OH solution, to verify the inactivity of the material towards MOR. This experiment is performed only on TiN50: since different deposition pressures show no difference in behavior in acidic media, and since both films have the same chemical composition, the obtained results can be extended to TiN60. The CV plots are shown figure 32.

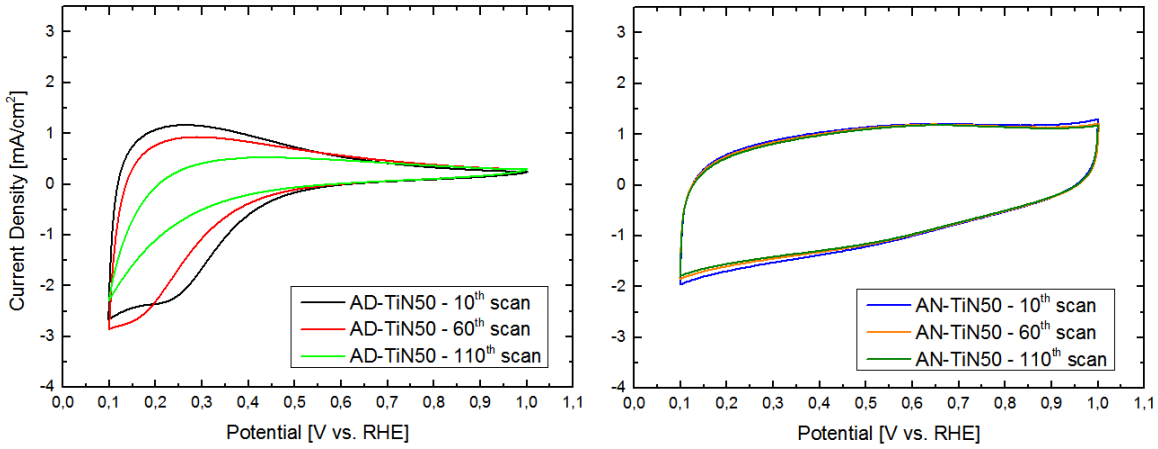

Figure 32: CV plot for AD-TiN50 and AN-TiN50. Scan rate: 150 mV/s. Electrolyte: 0.5 M H_2SO_4+ 1 M CH_3OH

Changing the electrolyte solution doesn't change the electrochemical response of both samples, since no difference in the CV scans from the ones taken in 0.5 M H_2SO_4 can be seen. This information confirms the inactivity of TiN towards MOR, as is already reported in the literature [24]. For AD-TiN50 the trend already reported for the scan in sulfuric acid is seen, with a more relevant decrease in current through cycling. The same considerations done for the previous CVs apply: after the initial scans, the peak current drops and the plot gets narrower, as if the film loses conductivity while cycling. Even for this experiment, after the cycling was over the film was delaminated and damaged by the combined action of acidic environment and applied voltage. AN-TiN50, on the other hand, still exhibits the capacitor-like behavior with better stability, both physical and chemical, and an inert nature.

Considering this chemical behavior, implementing AD-TiN50 or AD-TiN60 in a fuel cell electrode is unlikely: the film is not stable on the long-term period and the situation would be even worse in real cell conditions. However AN-TiN50 and AN-TiN60 show a good stability and will be implemented as support for the electrodeposition of the platinum catalyst in the next section.

Lastly, the influence of the deposition pressure on the electrochemical response of annealed TiN films is investigated by comparing the CV scans for AN-TiN50 and AN-TiN60. The last CV scan – i.e. the 110^{th} – in 0.5 M H_2SO_4 is plotted and compared, in order to have a representation of a stabilized condition for the TiN films.

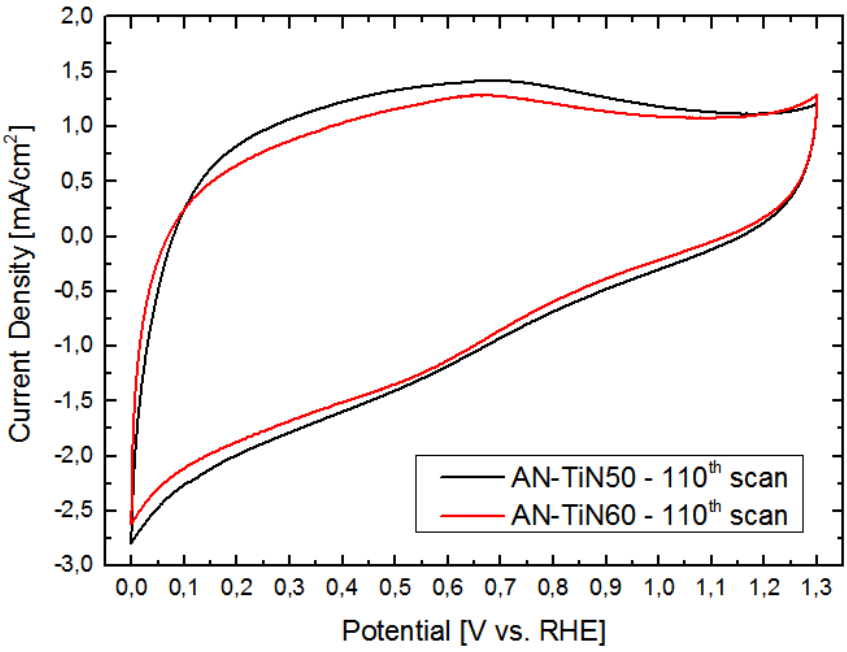

Figure 33: 110th CV scan for AN-TiN50 and AN-TiN60. Scan rate: 150 mV/s. Electrolyte: 0.5 M H_2SO_4

From this plot, we understand that there is no significant difference between the two samples, as previously inferred: the two CV curves share the same trend and the current densities are roughly the same, with just a small different in the peak oxidation current (but that is due to the carbon reaction and not the TiN support).

3.5. Effect of Electrochemical Testing on TiN Films

Lastly, it is interesting to analyze how electrochemical testing influences the morphology of the deposited films: thanks to the following high resolution SEM images presented in figure 34 and 35, we are able to relate the electrochemical behaviour of the TiN film with its nanostructure. The reported images show the effects on AD-TiN50 and AN-TiN50; because of the chemical and morphological similarities already pointed out in sections 3.3 and 3.4, the results that will be obtained can be extended to AD-TiN60 and AN-TiN60.

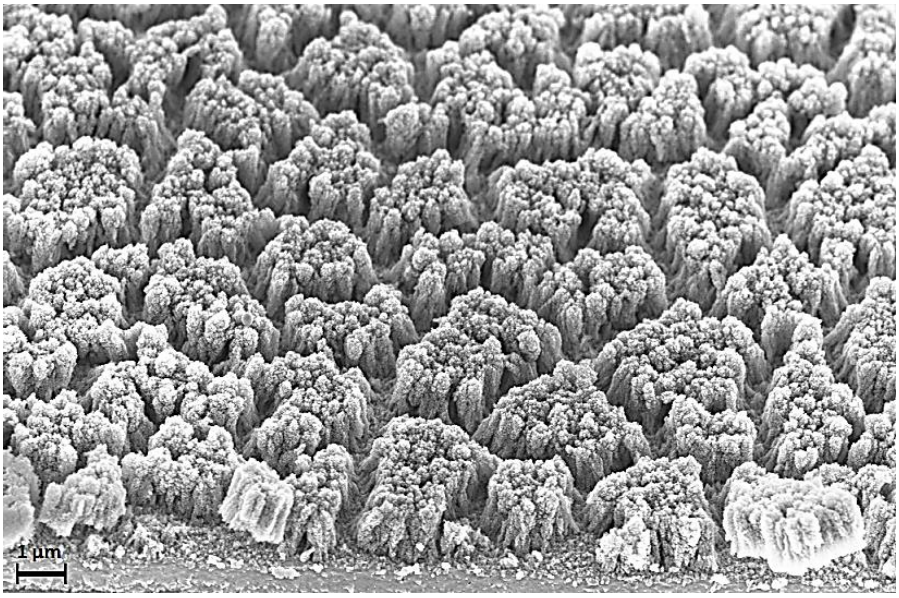

Figure 34: HR-SEM image of AD-TiN50 sample after CV scans in 0.5 M H_2SO_4

While the as deposited TiN 50 Pa sample had, before undergoing cyclic voltammetry testing, a nanostructure composed of many parallel nanotrees with equal and homogeneous spacing, after the scans the structure has completely changed. Part of it is wrecked by the combined action of acid and voltage, and the nanotrees assemble in many "islands" with a mean length of 2 µm separated by void canyons with a width of ~500 nm. This effect has been already reported in [43] for TiO_2 films deposited with PLD: as the background gas pressure increases during the deposition, the porosity of the nanostructure increases but the Young's modulus – and mechanical resistance – decreases, making the nanotrees collapse one on another. These effects lower the surface area of the scaffold, which can explain the significant current drop seen in the CV scans.

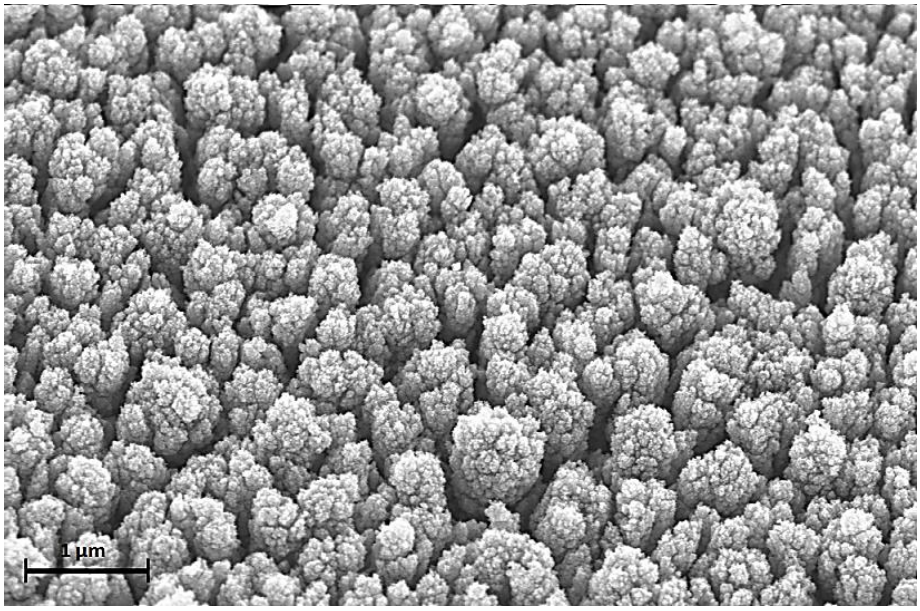

Figure 35: HR-SEM image of AN-TiN50 sample after CV scans in 0.5 M H_2SO_4

The situation for the annealed TiN 50 Pa sample is different: even in this case the nanostructures are degraded by the combined action of voltage and acid, since little cracks and canyons can be seen between the nanotrees. However, this time the effect is not as extreme as it was for the as deposited film: the mean width of the cracks is ∼170 nm, one third in comparison with the as deposited sample, and no island formation on the film is seen. After the annealing, cycling the TiN support doesn't make the nanotrees collapse one on another, with no substantial loss in surface area, as is confirmed by the CV plots of AN-TiN50.

Chapter 4

Deposition of Pt Catalyst on TiN Support

4.1. Electrochemical References

As a preliminary procedure before the optimization of the Pt catalyst electrodeposition technique and the testing of the support+catalyst material, a Pt/Ru thin film is fabricated and electrochemically tested, as a first reference value for future experiments.

The deposition of the thin film is carried out via DC magnetron sputtering from a Pt/Ru target (Testbourne, 99,99% Pt/Ru 50/50 wt.), in a vacuum chamber (base vacuum 10^{-3} Pa) filled with argon (99,9999%) at the desired pressure. As substrates, glassy carbon and FTO are chosen. The result is a thin and compact Pt/Ru film, with a width of 100 nm. The fabricated samples, named PtRu-GC (the ones deposited on glassy carbon) and PtRu-FTO (the ones deposited on FTO) are then electrochemically tested in a half-cell configuration, with a 0.5 M H_2SO_4 + 1 M CH_3OH solution, with the following protocol:

- 1 CV scan, composed of 10 cycles from 0,1 V to 1 V, with a scan rate of 150 mV/s, to activate the catalyst;
- 1 LSV, from 0,45 V to 1 V, with a scan rate of 10 mV/s, to check the activity of the Pt/Ru catalyst towards methanol oxidation and to qualitatively identify the onset potential of the MOR;
- 2 CV scan, each composed of 50 cycles from 0,1 V to 1 V, with a scan rate of 150 mV/s, in order to monitor the performance of the material after repeated cycling.

The CV plots for PtRu-GC and PtRu-FTO are shown in the figure below.

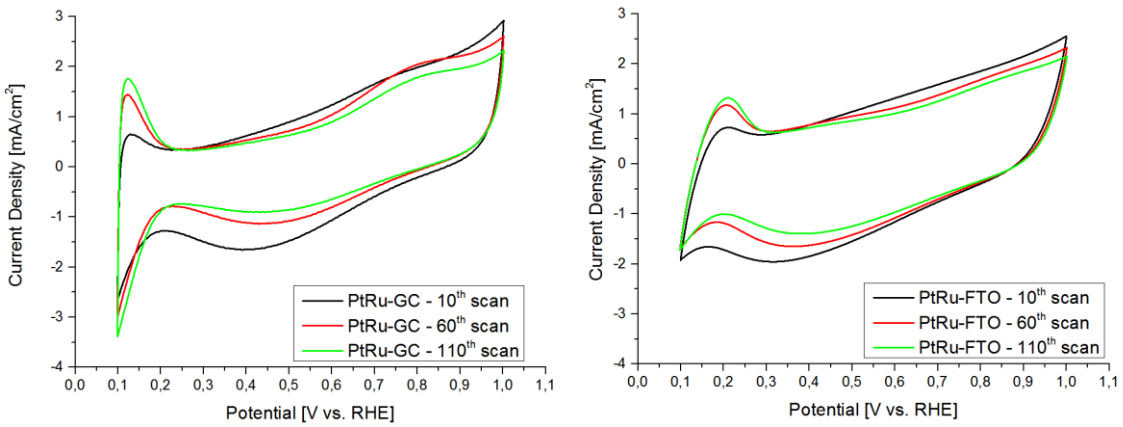

Figure 36: CV plots for PtRu-GC (left) and PtRu-FTO (right). Scan rate: 150 mV/s. Electrolyte: 0.5 M H_2SO_4 + 1 M CH_3OH

For the PtRu-GC sample we can see that:

- After 10 cycles the catalyst is not active towards methanol oxidation, since at ~0,7-0,8 V no oxidation current peak can be seen and therefore no reaction is occurring;
- At 0,2 V, during the reverse scan, a reduction peak is seen: this is the onset of hydrogen evolution reaction, and the peak in the CV is the adsorption of H^+ ions on Pt active sites. The corresponding oxidation peak appears at 0,15 V in the forward, and it is due to the desorption (and oxidation) of H^+ ions. Differently from a typical platinum CV, where three humps – corresponding to the adsorption/desorption of hydrogen on the three active faces

of platinum – can be seen, in this CV there is just one single peak i.e. just one Pt face is active. This is probably due to the method of deposition: the sputtered PtRu film is very compact, hydrogen can't penetrate it and it reacts on the only exposed Pt facet;

- The 60th and 110th scan show an oxidation peak at 0,7 V: after the activation, the catalyst is active towards the MOR.

For PtRu-FTO, however, no oxidation peak corresponding to the MOR can be seen, even after the 110th scan: it seems that the sample is not active at all towards the reaction, as suggested by the LSV here reported. While the onset potential of the MOR for PtRu-GC is ~0,5 V, it is absent for PtRu-FTO. We suggest that the lower conductivity of FTO can be a probable cause of this lack of activity.

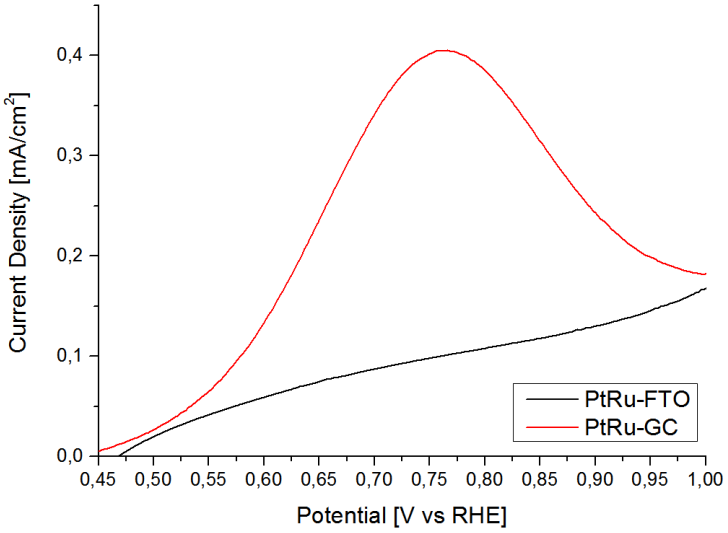

Figure 37: LSV for PtRu-GC (red line) and PtRu-FTO (black line). Scan rate: 10 mV/s. Electrolyte: 0.5 M H_2SO_4 + 1 M CH_3OH

4.2. TiN/PtRu Multilayer Catalyst

After the testing of the reference PtRu thin films, an attempt is made in fabricating a multilayered TiN/PtRu catalyst utilizing both PLD and DC magnetron sputtering; the attempt comes from the idea of dispersing the PtRu alloy on the whole TiN nanostructure. This objective would be achieved in a two-step fabrication:

- Depositing 200 nm of TiN with PLD, and covering it with 10 nm of sputtered PtRu. This process is repeated 5 times, in order to obtain five TiN/PtRu bilayers with a total catalyst loading of 50 µm/cm^2;
- Annealing the as deposited material at high temperature: we've seen that with annealing the TiN nanostructure changes its morphology and crystalline structure, with an increase in height. With this recrystallization the PtRu alloy, compressed between two TiN layers, should be pushed out and cover the nanostructures, dispersing on their surfaces.

Deposition takes place in a vacuum chamber (vacuum in the order of 10^{-3} Pa), while the process pressure is changed continuously: during pulsed laser deposition of TiN, N_2 is the process gas

and the pressure is 50 Pa, while during PtRu sputtering Ar is the process gas and the pressure is 15 Pa.

Two high-resolution SEM cross-section for the multilayer material, both as deposited and after thermal annealed – 500°C, 4 hours annealing in vacuum – are shown to better understand the composition of the TiN/PtRu.

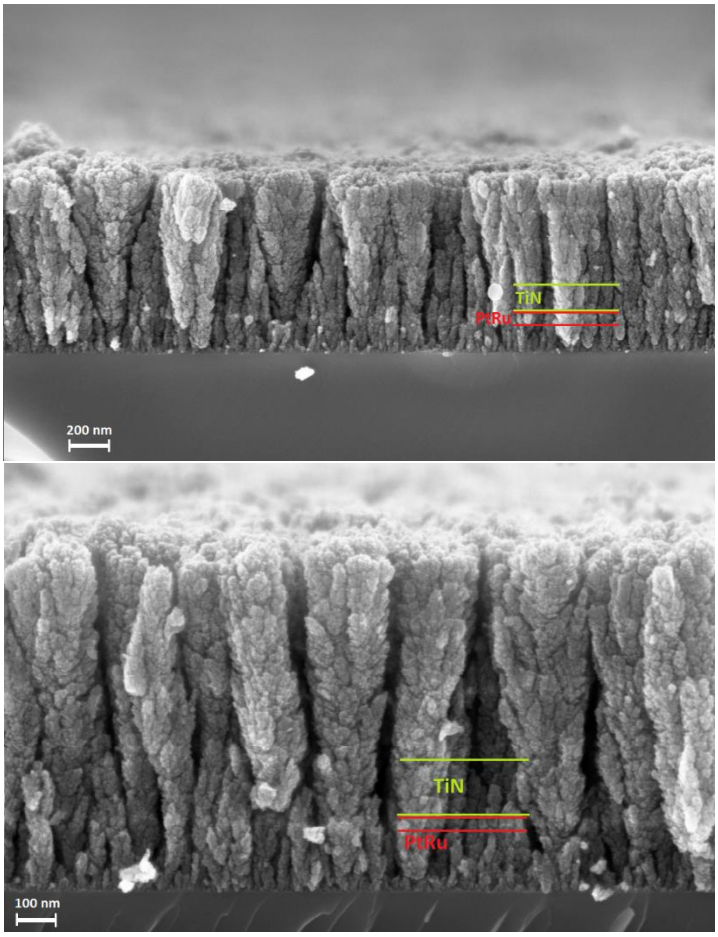

Figure 38: HR-SEM cross-section for AD-TiN/PtRu (top) and AN-TiN/PtRu (bottom)

The as deposited and annealed samples are then tested in half-cell configuration, and their performance towards MOR and their stability are tested with cyclic voltammetry experiments. As for the bare TiN films, the material undergoes 3 CV scans (the first composed of 10 cycles, the other two of 50 cycles) in 0.5 M H_2SO_4 + 1 M CH_3OH ranging from 0,1 V to 1 V, with a scan rate of 150 mV/s. The last cycle of each scan is then plotted.

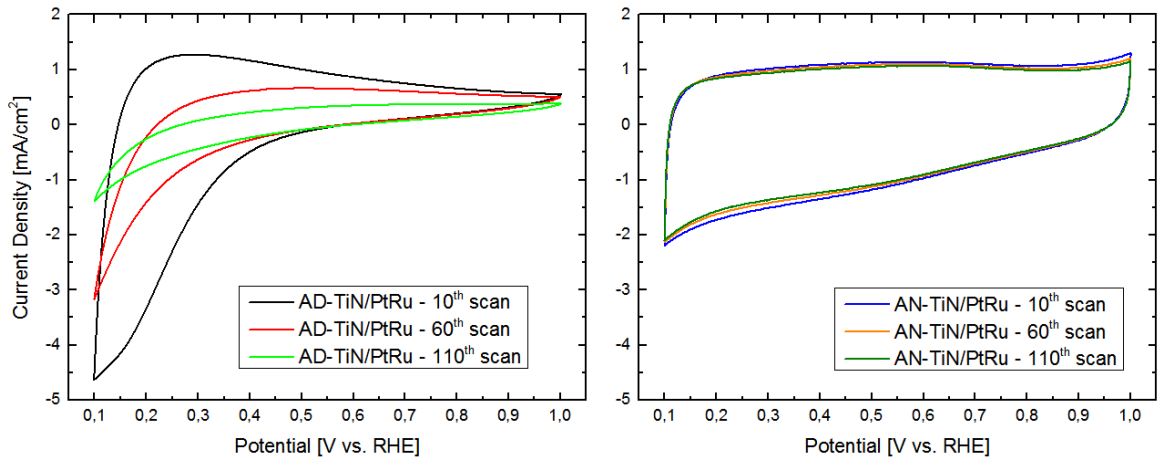

Figure 39: Cv plots for AD-TiN/PtRu (left) and AN-TiN/PtRu (right). Scan rate: 150 mV/s. Electrolyte: 0.5 M H_2SO_4 + 1 M CH_3OH

A quick analysis of the CV plots reveals that the multilayer has no activity towards MOR, because no current peak is seen for potentials above 0,4 V. By comparing these CVs with the ones of the bare TiN support, we see that there is no difference in electrochemical behavior: the sputtered PtRu catalyst is somehow not active.

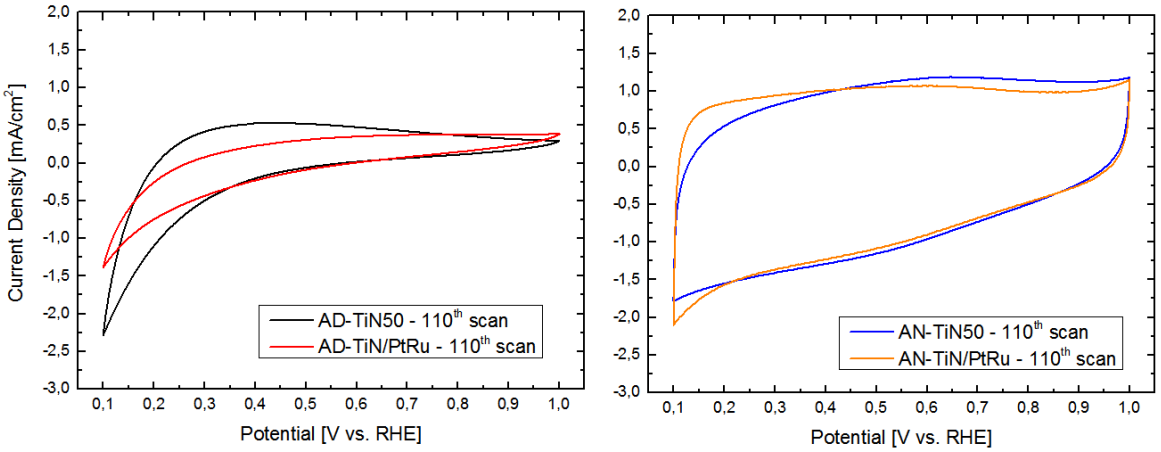

Figure 40: CV comparison between the as deposited (left) and annealed (right) TiN vs. TiN/PtRu. Scan rate: 150 mV/s. Electrolyte: 0.5 M H2SO4 + 1 M CH3OH

An explanation to this behavior is:

- For the as deposited TiN/PtRu, after the sputtering of a PtRu layer the following ablated TiN layer completely covers the metal film, which can't contact the electrolyte. The final PtRu layer, instead, is too thin and too compact: the catalyst molecules are not arranged in nanoparticles, which would have high surface area and would yield high currents, but they form a very thin film with no structuration and minimum surface area;
- For the annealed TiN/PtRu the same applies: the thermal treatment and the recrystallization of TiN does not push out the PtRu inner layers, which remain segregated inside the TiN structure and are not in contact with the electrolyte. Moreover with annealing carbon contaminations are added to the film, which worsen the situation for the PtRu catalyst.

In conclusion, because of the obvious fabrication defects that generate the poor electrochemical performance of the material, the TiN/PtRu multilayer is soon discarded.

4.3. Platinum Electrodeposition

After the failed attempt with the TiN/PtRu multilayer, the chosen strategy for depositing the catalyst on the support material is electrodeposition: the advantages and drawbacks of the technique have been already discussed in section 2.1.6.

Since electrodeposition has not been tried before, it is useful to have a "blueprint" deposition recipe from literature. An ideal recipe should not only be already tested for depositing a Pt catalyst for fuel cell applications, but should also be a galvanostatic – and not potentiostatic – one.
Faraday's law affirms that mass is directly proportional to the current that is flowing, or better, to the total charge that is transferred to an electrode. Therefore, when electrodepositing a material, the deposited quantity is proportional to the total charge involved in the process. A potentiostatic electrodeposition deposits the metal catalyst applying voltage pulses to the electrode. According to Ohm's law, the applied current – and consequently the deposited mass – is proportional to the voltage through the electrode resistance: when the electrode material changes, thus, the current will be different even if the same voltage is applied. A potentiostatic deposition, since is dependent on the electrode material, is not a good blueprint recipe.

A galvanostatic electrodeposition, on the other hand, imposes to the electrode a current pulse therefore the relationship between transferred charge and mass is univocal and not influenced by the electrode material.

For the purpose of this work, the chosen blueprint recipe comes from [35], where the pulsed technique is used to deposit Pt and Ru nanoparticles on a carbon cloth as anode catalyst for DMFCs. The paper also provides some optimal process parameters in order to obtain a good nanoparticles dispersion and a good methanol oxidation current:

- Current on-time of 50 ms;
- Current off-time of 400 ms;
- Current density of 50 mA/cm^2 and total charge of 8 C/cm^2.

With these parameters, the obtained nanoparticles exhibits a mean diameter of 4-20 nm, which is a good size value. Schematics of the current pulses is shown in figure 41.

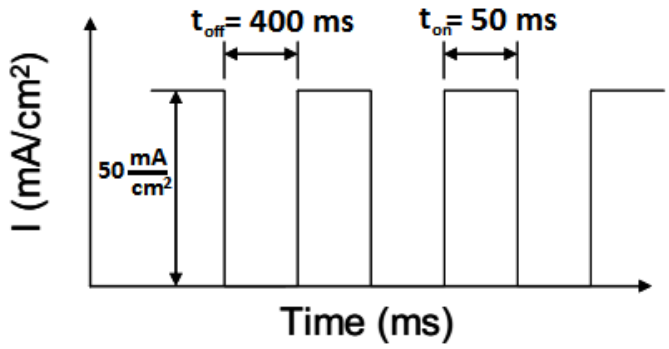

Figure 41: current pulses for the reference electrodeposition recipe

The first implementation step for the electrodeposition of platinum in the catalyst is replicating the recipe on the TiN scaffold depositing the Pt catalyst: we want to obtain results that are comparable, or at least consistent, with the literature.

This first test is carried out on AD-TiN50 on a glassy carbon substrate, with the following experimental setup – that will be used for all the following electrodepositions:

- A Pt mesh is used as counter electrode, while a saturated calomel electrode (SCE, E_0=+0,244 vs RHE) is used as reference electrode;
- The electrolyte is prepared by mixing appropriate amounts of Pt precursor – $H_2PtCl_6 \cdot xH_2O$ – and H_2SO_4 in aqueous solution. The resulting concentrations for Pt and H_2SO_4 are, respectively, 5 mM and 0.5 M. H_2SO_4 is added to the precursor solution to increase the conductivity of the deposition bath. This electrolyte will be used for all the electrodeposition process.

For this first, preliminary test, the applied current pulse on-time is 50 ms, the off-time pulse is 400 ms, the applied current density of 50 mA/cm$_2$ with a total charge of 8 C/cm$_2$.

After the deposition process, the sample AN-TiN/Pt8-50 is dried overnight at room temperature before subsequent electrochemical testing, which takes place as follows: 3 CV scans (the 1st composed of 10 cycles, the other two of 50 cycles) from 0 V to 1,3 V in 0.5 M H_2SO_4 solution to check the presence of the Pt catalyst and its activity towards hydrogen adsorption/desorption.

For the cyclic voltammograms in H_2SO_4, the last cycle of each scan is plotted. The 10th scan is plotted alone to highlight the activation process that affects the catalyst.

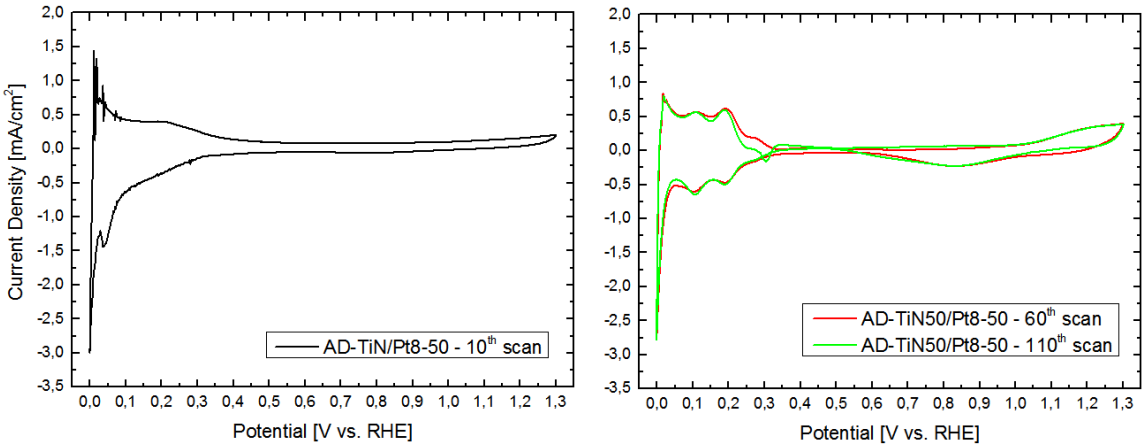

Figure 42: CV scans (left: 10th cycle, right: 60th and 110th cycle) for AD-TiN50/Pt8-50. Scan rate: 150 mV/s. Electrolyte: 0.5 M H_2SO_4

During the forward potential scan of the 10th cycle, no activity can be seen for the Pt catalyst: there is no clear hump in the oxidation peak at ~0 V corresponding to the desorption and oxidation of hydrogen ions. Moreover there is no reaction onset can be seen at ~0,9 V, corresponding to the reversible oxidation reaction of the platinum catalyst. In the backwards scan, consequently, no reduction current peak associated with the reduction of the previously formed platinum oxides is seen – since no oxides have been formed. However in the backwards scan, at ~0,05 V, the first hump related to the adsorption of hydrogen on platinum can be seen in the reduction peak.

The explanation to this behavior is that the catalyst activates after 10 cycles, as is confirmed by the scans plotted in figure 42. When the situation is stabilized, we can clearly see:

- At high potentials, above 0,5 V, an increase in the oxidation current at ~1,1 V: this is the onset of the platinum oxidation reaction. The corresponding reduction peak at 0,8 V is also present;
- At low potentials the bumps of the adsorption/desorption of hydrogen on Pt active sites are present and well visible.

As a conclusion, the electrodeposited Pt catalyst after 10 cycles behaves as widely reported in literature, in regards with the hydrogen adsorption and the Pt oxides formation. However, after testing is concluded, it is noticed that the TiN film is delaminated: the scan acquired in figure 41 shows the features not of TiN-supported Pt, but of the platinum that during electrodeposition landed not on the film but on the bare glassy carbon substrate.

This phenomenon is probably caused by the AD-TiN scaffold itself: in acidic environment TiN is prone to form oxides. When, during electrodeposition, potentials in the order of -0,3 V are reached, the oxidized TiN undergoes reduction, and the adsorbed oxygen molecules are torn off from the material. This reaction is what causes the embrittlement and subsequent delamination of the TiN support.

With this preliminary experiment, we have obtained a working electrodeposited catalyst, but at the same time the TiN film has revealed its instability in the harsh acidic condition of electrodeposition bath and potential sweeping.

The implementation of the Pt electrodeposition to obtain a working catalyst, after this first preliminary test, is structured in the following steps:

I. Testing the stability of the TiN film throughout electrodeposition and the stability of the TiN+Pt catalyst after cyclic voltammograms;
II. Determine the faradaic efficiency for the electrodeposition process, in order to evaluate precisely the real catalyst mass deposited on TiN;
III. Optimize the total deposited charge during electrodeposition, in order to obtain a reasonable catalyst loading and to maximize the ECSA of the Pt catalyst;
IV. Optimize the TiN support: since TiN50 and TiN60 share the same electrochemical behavior, the influence of the deposition pressure (and therefore of the nanostructure) on the ECSA of the catalyst is investigated, in order to maximize the active area of the catalyst and obtain the best performance;
V. Optimize the duration of the current on-time pulse: we want to see how changing this parameter during the electrodeposition modifies the Pt deposit properties and ultimately the performance and activity of the catalyst.

4.4. Platinum Electrodeposition – TiN Stability Evaluation

The first step in the implementation of the electrodeposition technique are resolving the film delamination problem and investigating the influence of the deposition pressure on the performance of the electrodeposited catalyst. To overcome the delamination problem, the deposition is carried out on AN-TiN samples (with the standard length of 1 μm), since electrochemical characterization pointed out the enhanced stability in harsh environments of the annealed TiN films.

For the stability evaluation, during electrodeposition the total deposited charge is increased from 8 C/cm^2 to 16 C/cm^2. The increase of this parameter is performed to deposited a bigger catalyst loading on the TiN film, so that the effect of Pt can be clearly seen from the CV plots.

The fabricated AN-TiN/Pt16-50 catalyst is the dried overnight and subsequently tested in a half-cell configuration, with the CV protocol already implemented. In the following figure, the CV plots are shown.

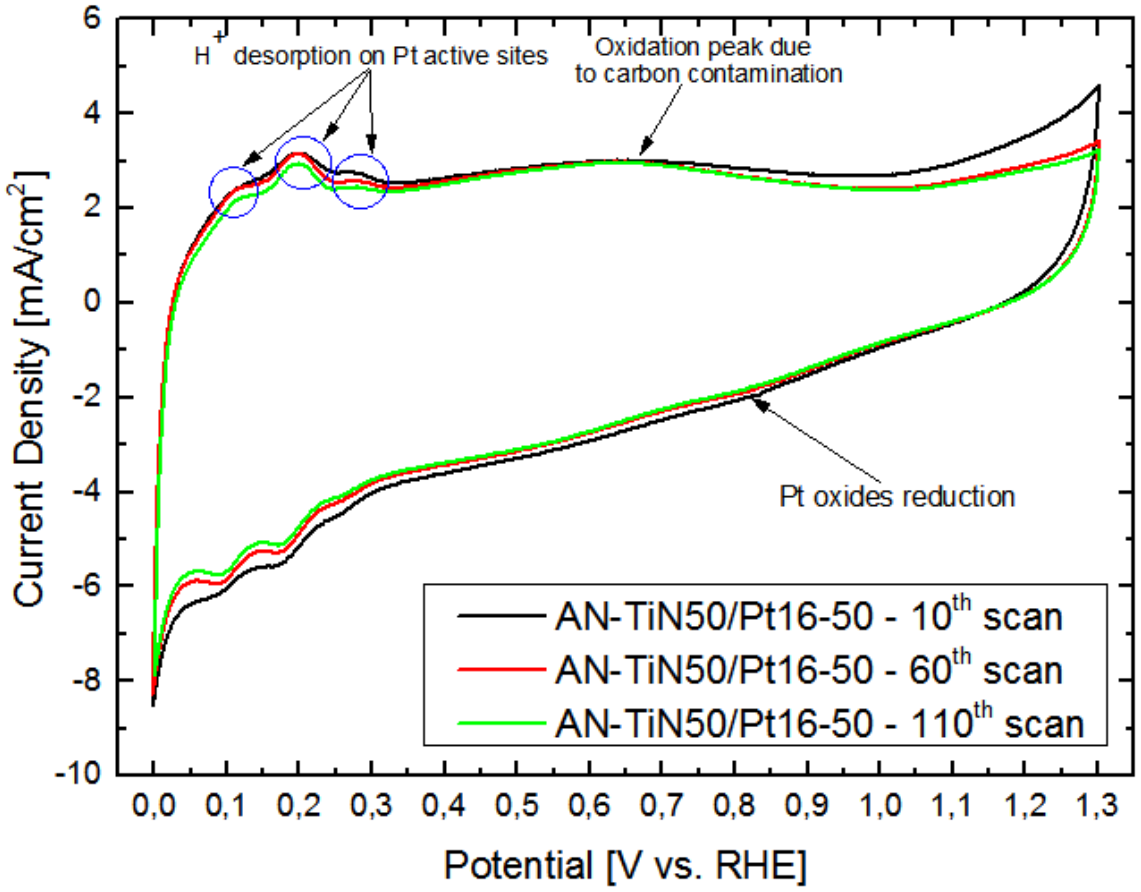

Figure 43: CV plots for AN-TiN/Pt16-50 catalyst. Electrolyte: 0.5 M H_2SO_4. Scan rate: 150 mV/s. The catalyst features are highlighted.

AN-TiN50/Pt16-50 shows good behavior, outclassing the previous one that implemented the as deposited films, and more importantly exhibits electrochemical features consistent with the literature. In particular, at low voltage the three characteristic peaks of adsorption/desorption of hydrogen ions on the three Pt active facets can be recognized. The humps related to the desorption of hydrogen ions in the oxidation region are indicated in the plot.

A carbon contamination present on the annealed TiN film, as confirmed by the carbon oxidation peak at ~0,5 V. The carbon contamination is a serious problem for the overall utilization and efficiency of the catalyst: since the carbon oxidation peaks increases the overall double layer current of the electrode, the hydrogen desorption region in the CV plot will be smaller and the overall Electro-Chemical Surface Area (ECSA) of the catalyst will be lower. Effort is put into eliminating the contamination affecting the tubular furnace where annealing takes place; while in the later stages of this work the problem is limited and the carbon contamination decreases, it is still not completely eliminated. Therefore, all of the catalyst suffers to a certain degree of a loss of ECSA and a performance degradation that can be ascribed to the undesired presence of carbon.

Following this test, we have confirmed one more time the superior chemical stability of the AN-TiN film: as final proof of this conclusion, after the CV test AN-TiN50/Pt16-50 has not detached

from the substrate, nor visible signs of mechanical instability can be spotted. The conclusion of this implementation step is that the following electrodepositions will be performed on annealed TiN films.

4.5. Platinum Electrodeposition – Deposited Charge Optimization

With the previous optimization steps in the implementation of the catalyst deposition method, electrodeposition of Pt catalyst has been successfully performed and a stable working TiN-supported catalyst has been obtained. With the third step in the implementation, the focus shifts on enhancing the performance of the catalyst. To reach this goal, the total deposited charge is varied in order to obtain two results:

- **Depositing a reasonable catalyst loading** on the support: the deposited catalyst mass is directly proportional to the deposited charge, and to the overall cost of the material. Typical Pt catalyst loadings for DMFC anodes range from 2 to 8 mg/cm^2, depending on the application [7], while for PEMFCs Pt loadings of 0,2 mg/cm^2 up to 6 µg/cm^2 have been obtained [44]. In order to demonstrate the possibility of obtaining a support+catalyst material deposited via PLD, to be exhaustively characterized in future works, that can compete with the state-of-the-art catalyst, we decided that the deposited catalyst loading should not exceed 0,3-0,4 mg/cm^2;
- **Achieving the maximum ECSA**: this value is inversely proportional to the catalyst loading but, at the same time, it is directly proportional to the hydrogen desorption area in the CV plots. This one is, in turn, proportional to the active catalyst mass, which theoretically increases if the catalyst is well dispersed on the TiN nanostructures during electrodeposition. Ideally, this last relationship holds is based on the hypothesis of optimal dispersion of the catalyst, which is to be verified.

To summarize, the deposited charge to be implemented is the result of an optimization process: it is the one that minimizes the overall cost while still giving a good catalytic activity and a high ECSA.

For this optimization step, four different deposited charges are tested: 8 C/cm^2, 16 C/cm^2, 32 C/cm^2, 64 C/cm^2. During these depositions, the fixed parameters are:

- Current pulse on-time: 100 ms, current pulse off-time: 500 ms;
- Current pulse intensity: 50 mA/cm^2;
- Support material: TiN 50 Pa, with a length of 1 µm, pre-annealed at 500°C for 4 hours in vacuum (AN-TiN50).

The four samples, named AN-TiN50/Pt8-100 (for the 8 C/cm^2 sample), AN-TiN50/Pt16-100 (16 C/cm^2), AN-TiN50/Pt32-100 (32 C/cm^2) and AN-TiN50/Pt64-100 (64 C/cm^2) are fabricated and then dried overnight at room temperature. Subsequently, they are tested in an electrochemical half-cell configuration, with a 0.5 M H_2SO_4 solution, with a scan rate of 150 mV/s.

Three CV scans (10 cycles the first one, 50 cycles the other two) from 0 V – to highlight the onset of the hydrogen evolution reaction – to 1,3 V are performed and the last cycle of each scan is plotted. For the purpose of this optimization step, no CV scan is performed in a methanol-containing solution: the main interest is determining the catalyst with the best active area and this information, which is directly connected to the performance towards the MOR, can be obtained with simple CVs in H_2SO_4.

It must be pointed out that, due to the carbon contamination in the tubular furnace where annealing takes places, the four samples presents carbon contaminations.

In figure 44, the CV plots for the four samples are reported.

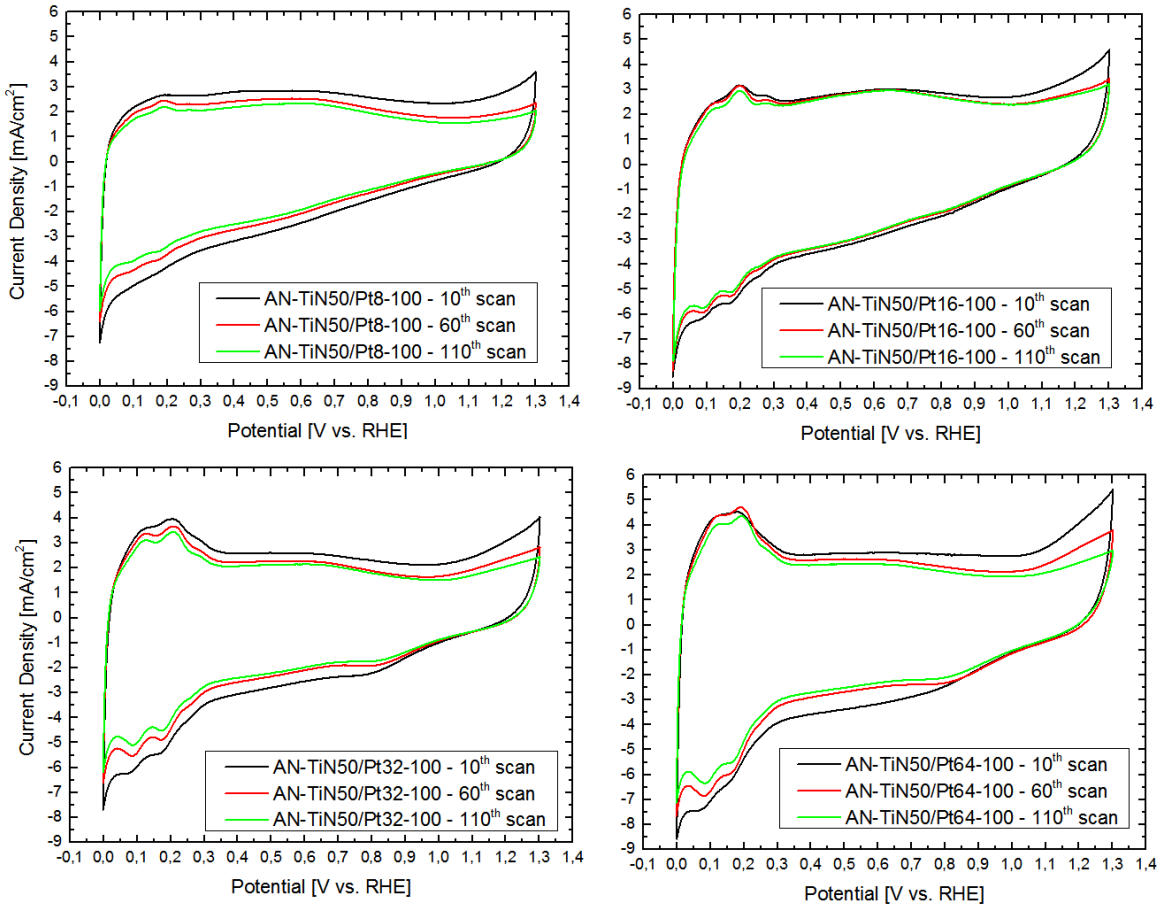

Figure 44: CV plots for different deposited charges: 8 C/cm² (top left), 16 C/cm² (top right), 32 C/cm² (bottom left), 64 C/cm² (bottom right). Scan rate: 150 mV/s. Electrolyte solution: 0.5 M H_2SO_4.

We can see that for the AN-TiN50/Pt8-100 and AN-TiN50/Pt16-100 samples the hydrogen desorption peaks at low potential are not very sharp and lie inside, almost completely, the high double layer current region generated by the carbon contaminants: this suggests a very low ECSA and a poor performance of the catalyst.

The situation is better for the AN-TiN50/Pt32-100 and AN-TiN50/Pt64-100 samples: even though the carbon contamination is still present and the double layer current is very high, the hydrogen desorption peaks can be clearly spotted. The same applies for the Pt oxide reduction peak at 0,8 V in the reverse scan, which on the other hand couldn't be clearly distinguished on

AN-TiN50/Pt8-100 and AN-TiN50/Pt16-100 because it was convoluted in the carbon reduction peak. The presence of the Pt oxide reduction peak for the last two samples is an additional proof of the activity of the Pt catalyst.

Apart from a qualitative analysis of the CV plots, the performance and the activity of the different catalyst is calculated quantitatively through ECSA. In section 2.1.6 it was stated that the effective deposited catalyst is linked to the ideal – i.e. the one calculated with Faraday's law – deposited quantity through the *faradaic efficiency* of the electrodeposition. Unfortunately, this parameter cannot be calculated *a priori* but only with a recursive approach, employing different methods after the deposition is performed.

For the evaluation of the ECSA in this optimization step, the utilization of a recipe reported in literature as a blueprint gives us a first evaluation of the faradaic efficiency of our process. In [35], the efficiency is:

$$\eta_{faradaic} = \frac{m_{Pt,real}}{m_{Pt,ideal}} \sim 2{,}1\% \qquad (4.1)$$

The faradaic efficiency reported in the literature has been used in this step to evaluate the total catalyst load, because in this optimization step the total deposited electrical charge has been varied. The variation of the deposited charge means that the TiN films are exposed to the harsh environment of the electrodeposition bath and to prolonged current pulses for different periods of time: the effect of these conditions on the mechanical resistance and endurance of the TiN film is yet to be determined, therefore calculating the deposited catalyst loading with a mass measurement would probably lead to inaccurate results, because mass variations of the TiN films may invalidate the obtain data.

Consequently, the value obtained by the reference paper is used as a first esteem of the faradaic efficiency of the process. Since the electrodeposition bath employed and the deposition parameters are similar, we can assume that for a first analysis, this value is an acceptable approximation of the real efficiency.

However, between our deposition and the one reported in the literature there are many differences that must be taken into account:

- Different substrate for deposition: in the paper the catalyst was deposited on carbon cloth, here on a TiN support deposited on a glassy carbon substrate;
- The deposition parameters (pulse on-time and off-time) are similar but not the same;
- The total deposited charge is not the same.

Because of these factors, the efficiency value taken from the reference paper must not be considered a correct, precise value, but an indication of the order of magnitude of the efficiency. The ECSA values plotted in the figure below, therefore, must not be considered correct; their trend, however, can be considered plausible, because the same factor has been employed in the calculation of the ECSA of all the samples.

The resulting ECSAs and their evolution through cyclic voltammograms are plotted in figure 45, with the numerical values reported for the 10th, 60th and 110th CV scan.

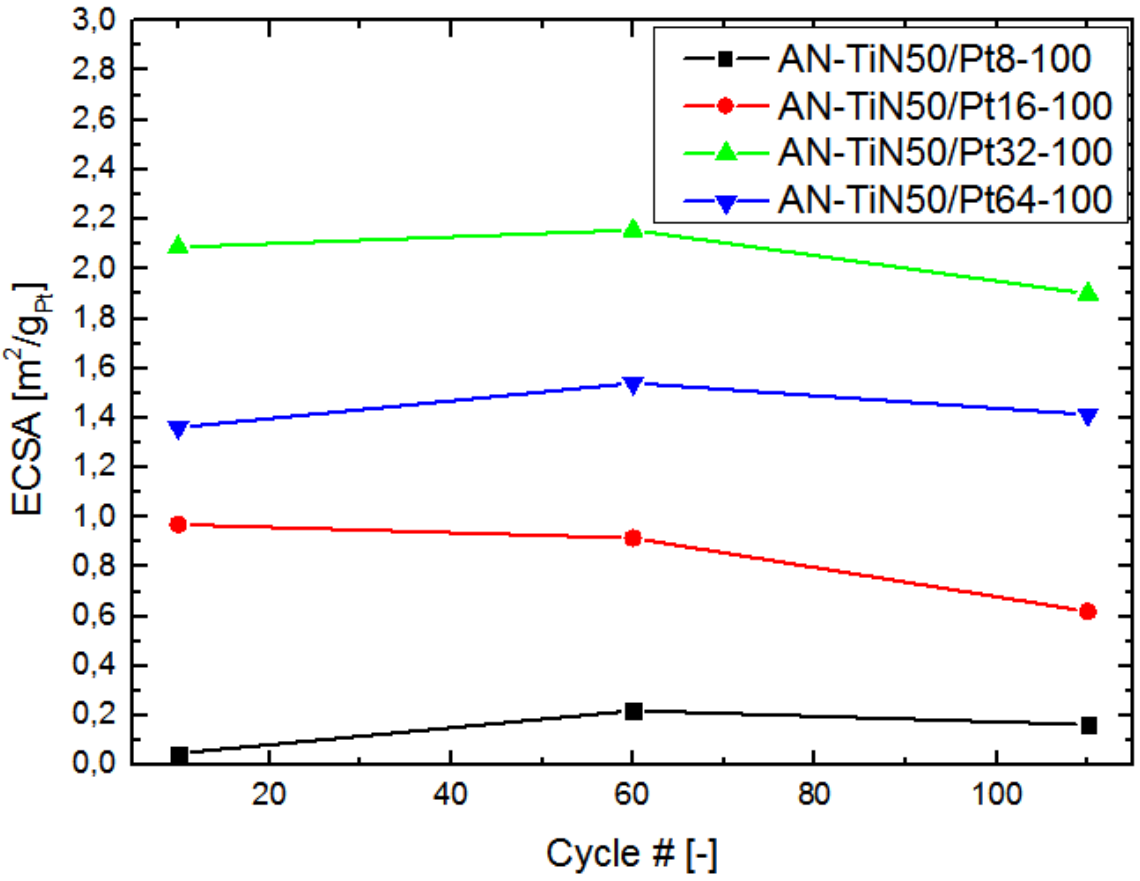

Figure 45: ECSA variation during CV scans for the four catalyst

From the ECSA analysis, some considerations can be done:

- The initial hypothesis on the very low ECSA for AN-TiN50/Pt8-100 is correct: because of the double-layer current the ECSA has a very low value, with a peak of 0,2 m^2/g_{Pt} at the 60th scan;
- The situation is slightly better for AN-TiN50/Pt16-100, even though after the initial maximum ECSA value, the trend decreases steeply after the 60th cycle dropping to a very low value (0,6 m^2/g_{Pt}) at the final scan;
- The ECSA is higher for both AN-TiN50/Pt32-100 and AN-TiN50/Pt64-100. The same trend of AN-TiN50/Pt8-100 is observed, with an initial increase of the ECSA between 10th and 60th cycle and a subsequent decrease from the 60th cycle to the 110th. As expected, the ECSA magnitude for both catalysts is bigger than that of AN-TiN50/Pt8-100. However, AN-TiN50/Pt32-100 exhibits a bigger ECSA than AN-TiN50/Pt64-100, despite its catalyst loading is halved.

This last effect can be explained as a saturation of the TiN nanostructure when 64 C/cm^2 of platinum are deposited: that is, at a certain point the Pt nanoparticles don't deposit on the TiN nanostructure anymore but preferentially on top of other, previously deposited Pt

nanoparticles, forming clusters with bigger dimension and diameter, that have therefore a lower surface/volume ratio. The consequence is a decrease of the catalyst total active area.

The observed ECSA trend, i.e. the initial increase between 10th and 60th cycle and the final decrease between the 60th and 110th cycle, is explained with two concurring mechanism that affects the nanostructure and the catalyst during potential sweeping:

- The initial increase in ECSA is due to the catalyst activation effect: during the first CV cycles, not all the catalyst particles are active, because some impurities deposited on the film can be present and block the contact between electrolyte and catalyst. After some scans these impurities are oxidized or removed, thanks to the combined action of acid and potential sweeping, and the previously covered catalyst particles come in contact with the electrolyte, with an increase in the overall ECSA;
- The final decrease effect is caused by two phenomena: platinum dissolution and the "island" effect that affects the TiN nanostructure. For the first cause, when the potential is higher than 0,8 V, platinum is dissolved, with a consequent loss in active area [45]. As for the second cause, the island effect, consisting in the collapse of the nanotrees that compose the film – as pointed out in section 3.5 – leads to the formation of nano-assemblies inside which the entrance of reagent is obstructed. This transformation in the nanostructure leads to a loss of support – and consequently catalyst – active area.

The effect of extensive potential sweeping in acidic media on the catalyst is clear on the following high-resolution SEM image, showing the appearance of the TiN "islands" that reduce the active area. Even in this case many cracks and canyons, with a mean width of approximately 200 nm, appear on the surface, while the nanotrees organize in less-spaced structures.

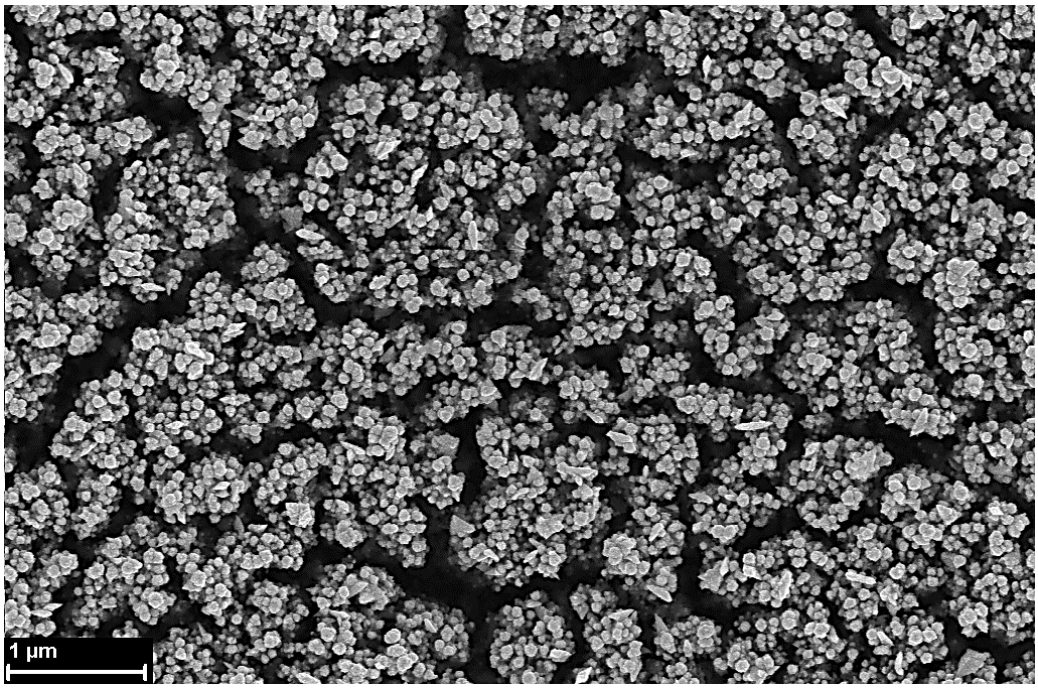

Figure 46: HR-SEM top view for AN-TiN50/Pt16-100 after CV scans

In addition to the electrochemical analysis of the catalyst activity, the achieved Pt dispersion through electrodeposition is investigated, as long as the mean diameter of the deposited particles, with the help of high-resolution SEM images, which are shown in the next figures.

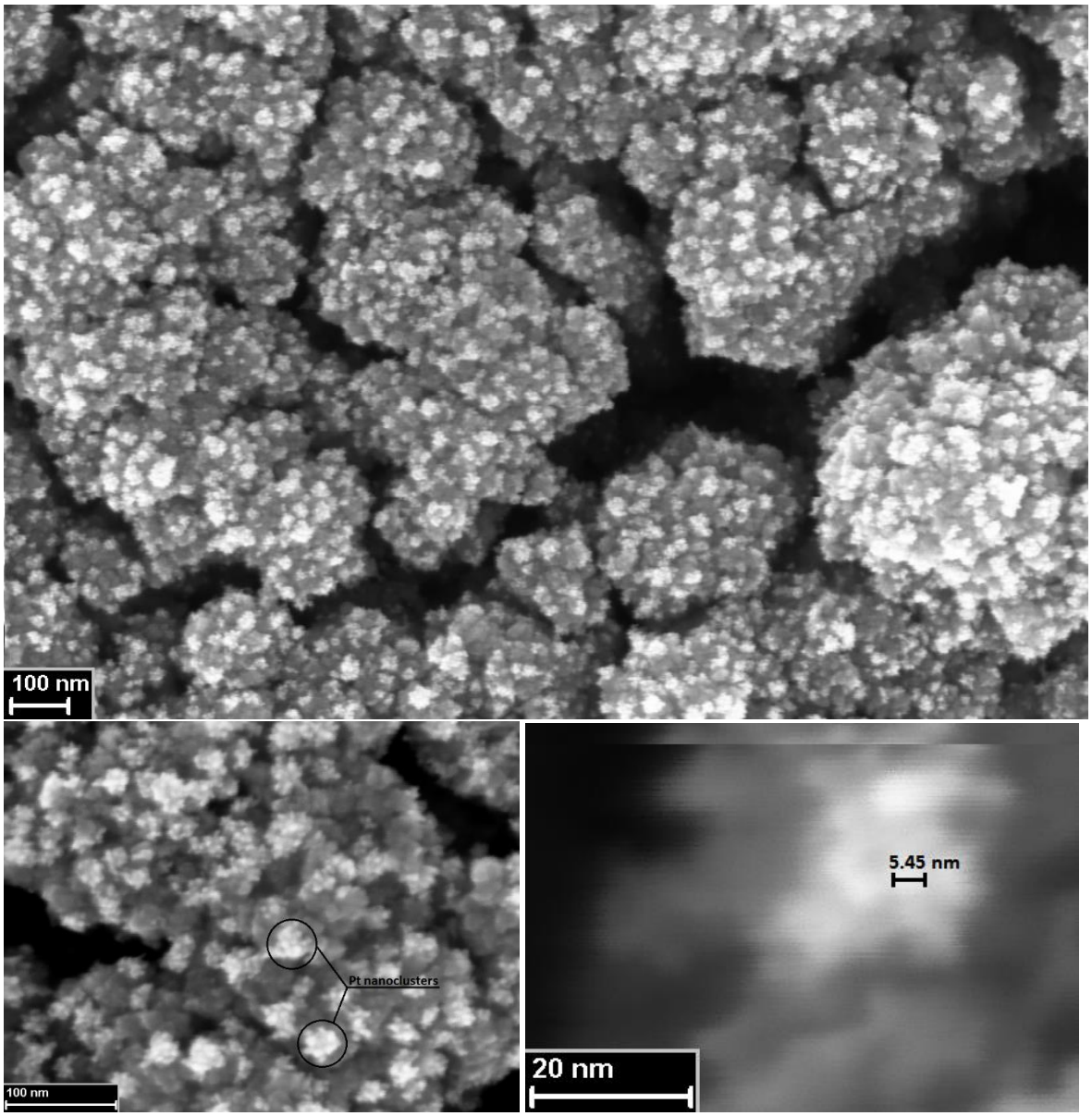

Figure 47: TOP: HR-SEM top view for AN-TiN50/Pt64-100 before CV. BOTTOM LEFT: higher magnification, highlighting Pt nanoclusters. BOTTOM RIGHT: higher magnification, highlighting Pt nanoparticle

Figure 47 shows top views for AN-TiN50/Pt64-100 with increasing magnifications. The upper image reveals the Pt coverage obtained through electrodeposition: the majority of the Pt particles deposit on the tips of the TiN nanostructure, while a lesser part penetrates in depth inside the nanostructure and deposit on the "trunk" of the nanotrees. This indicates that the dispersion of the catalyst is not optimal, because part of the nanostructure is not contacted by the catalyst and the overall ECSA that will be obtained will be lower than the surface area of TiN.

In the bottom left image, at higher magnification, Pt nanoclusters are indicated: the formation of the nanoclusters, that was hypothesized as cause of the lower active area of AN-TiN50/Pt64-100 in comparison with AN-TiN50/Pt32-100, with a mean diameter of ∼20 nm, is in fact the cause of this lower value and is caused by the saturation of the TiN support due to the high deposited charge. Finally the bottom right image, at highest magnification, highlights the size of the deposited Pt nanoparticles when clusters are not formed: a mean diameter of ∼5,5 nm is obtained, a value that is in line with the results reported in literature for MOR Pt-based catalysts [46, 47], and that helps in maximizing the catalyst ECSA.

Unfortunately, it wasn't possible to obtain any HR-SEM image for the AN-TiN50/Pt32-100, therefore a comparative morphological study for the Pt nanoparticles on the two different substrate can't be performed.

After this analysis, we can draw conclusions for the next optimization phase of the electrodeposition:

- The most promising deposited charge is 32 C/cm^2, because it holds the best ECSA value;
- When 64 C/cm^2 are deposited, a saturation of the support is reached and the increase in Pt loading doesn't lead to a corresponding increase in ECSA. Furthermore, the estimated catalyst loading for TiN50/Pt64 is ∼0,68 mg/cm^2, which despite being below the values reported in literature, exceeds roughly twice the desired loading pointed out at the beginning of this optimization step (0,3-0,4 mg/cm^2);
- With a current pulse on-time of 100 ms nanoparticles with a mean diameter of 5,5 nm are obtained. Since pulse on-time and nanoparticles diameter are related, an investigation of the relationship between current pulse duration and nanoparticles diameter is necessary in order to achieve the best possible catalytic performance.

The conclusion of this optimization step is that the total charge to be deposited on the TiN nanostructure is 32 C/cm^2: this value will be kept constant in the following optimization step and in the implementation of the electrodeposition.

At this point, the last two optimization steps have to be performed, and are focused – respectively – on the influence of the nanostructure on the ECSA of the catalyst and, lastly, on the relationship between pulse on-time, nanoparticle diameter and catalytic performance.

4.6. Platinum electrodeposition – Faradaic Efficiency Determination

Now that the total charge to be deposited on the TiN film has been optimize, a more precise evaluation of the faradaic efficiency of electrodeposition is necessary in order to obtain quantitative information on the deposited catalyst loading with the employed electrodeposition parameters and, consequently, a more accurate evaluation of the ECSA of the deposited Pt catalyst. To obtain this data, the following procedure is employed:

- Electrodeposition of Pt is carried out on different glassy carbon substrates, with the same deposited charge of 32 C/cm^2;

- The mass of the different substrates before and after deposition is measured; the measured difference is the deposited Pt catalyst loading;
- With a fixed deposited charge, the ideal deposited catalyst loading is known (see equation 2.1. with $\eta_{faradaic}$=1) and the faradaic efficiency of the deposition can be calculated as the ratio between real and ideal catalyst loading.

The results of these tests are reported in table 4.

	$m_{Pt,ideal}$ [mg/cm^2]	$m_{Pt,real}$ [mg/cm^2]	$\eta_{faradaic}$ [%]
Sample #1	12,94	0,590	4,56%
Sample #2	12,94	0,217	1,68%
Sample #3	12,94	0,280	2,16%
Sample #4	12,94	0,297	2,30%
Sample #5	12,94	0,190	1,47%
Sample #6	12,94	0,079	0,61%
Sample #7	12,94	0,367	2,84%
Sample #8	12,94	0,272	2,10%

Table 4: faradaic efficiency recorded for electrodeposition of Pt on different substrates

From these results, the mean value and the error affecting the measure are calculated, for both faradaic efficiency and deposited catalyst loading. The results are reported in equation 4.2. and 4.3. below.

$$\eta_{faradaic} = 2{,}21 \pm 1{,}15\% \tag{4.2}$$

$$m_{Pt} = 0{,}287 \pm 0{,}149\ mg_{Pt}/cm^2 \tag{4.3}$$

This value will be the one used to evaluate the ECSA from this point on.

4.7. Platinum Electrodeposition – Support Optimization

With the pressure scan for the different deposited TiN films carried out in section 3.2.1 and 3.2.2. and from the analysis of annealed TiN50 and TiN60 films reported in section 3.3, we reached the conclusion that the TiN60 nanostructure holds a higher surface area and a more pronounced porosity than TiN50. When the two annealed films were electrochemically characterized in section 3.4, the comparison of the CV plots lead to the conclusion that the electrochemical behavior of the two supports is the same, with no evident difference observed in the cyclic voltammograms. Because of this evidence, to obtain the maximum catalyst ECSA, electrodeposition is performed also on annealed TiN60 film, to investigate how the different support porosity changes the activity of the Pt catalyst.

The morphological and electrochemical features of AN-TiN50 and AN-TiN60 pointed out in the previous paragraph are reported in the following figure.

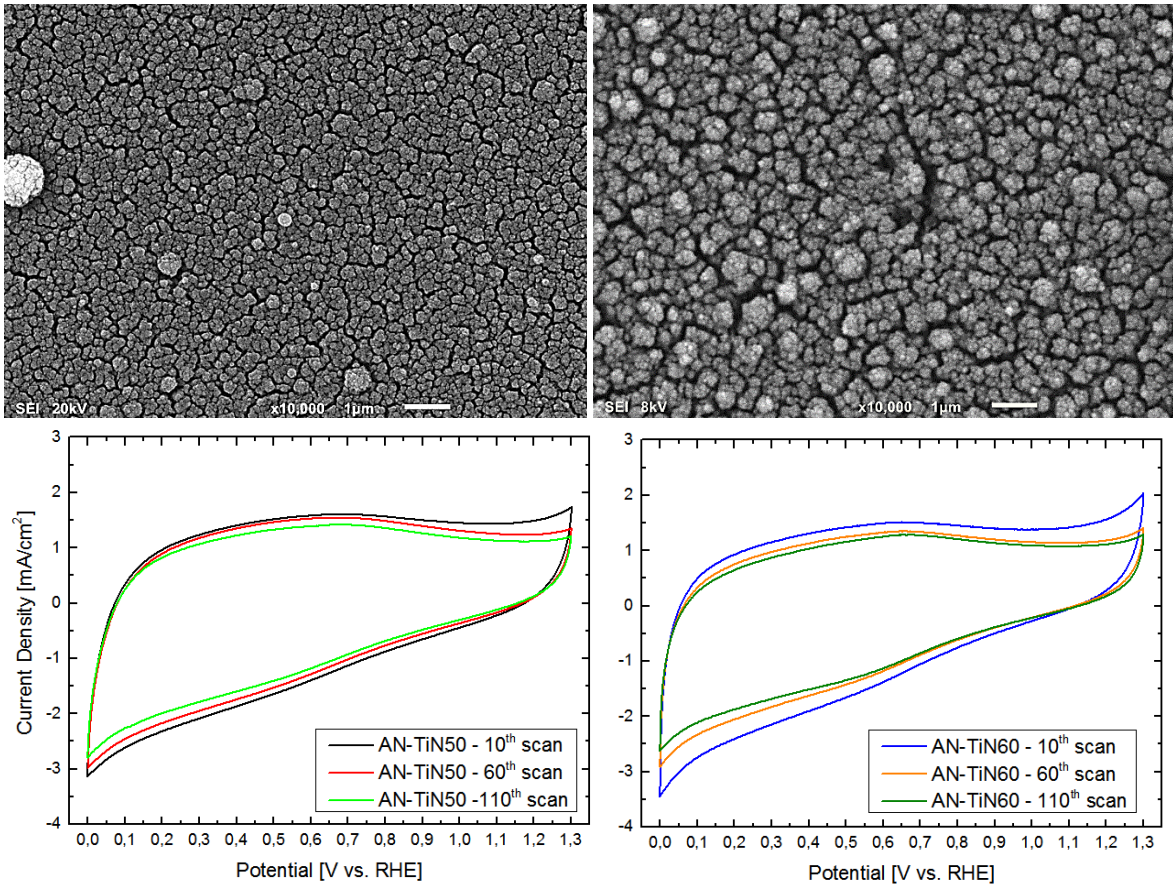

Figure 48 TOP LEFT: SEM top view of AN-TiN50. TOP RIGHT: SEM top view of AN-TiN60. BOTTOM LEFT: CVs for AN-TiN50. BOTTOM RIGHT: CVs for AN-TiN60. Electrolyte: 0.5 M H_2SO_4. Scan rate: 150 mV/s

The process parameters employed for electrodeposition are the following:

- Current pulse on-time: 100 ms, current pulse off-time: 500 ms;
- Current pulse intensity: 50 mA/cm^2;
- Total deposited charge: 32 C/cm^2.

After deposition and drying overnight, the two catalyst AN-TiN50/Pt32-100 and AN-TiN60/Pt32-100 are electrochemically tested in 0.5 M H2SO4 and their ECSA is compared. The results are plotted in figure 49.

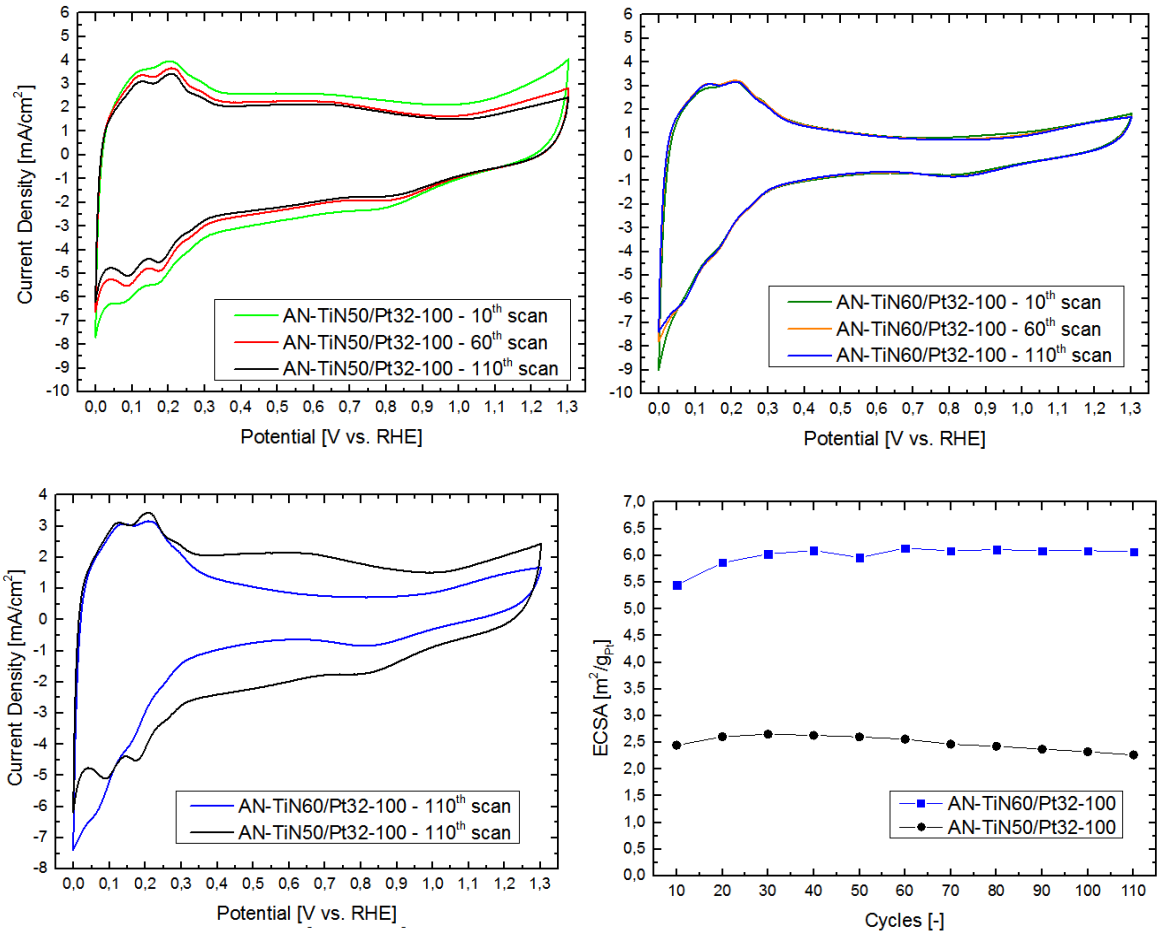

Figure 49: Top: CV plots for AN-TiN50/Pt32-100 and AN-TiN60/Pt32-100. Bottom left: 110th scan comparison for the two catalyst. Bottom right: ECSA comparison

Three information can be inferred from the reported plots:

- Changing the deposition pressure for TiN doesn't change the electrochemical behavior of the Pt catalyst: the two CVs, in fact, share the same features. At low potential, for both catalysts the three "humps" related to the adsorption and desorption of hydrogen ions are present and in the reduction zone at ~0,8 V the Pt oxides reduction peak is seen;
- The current densities in the low-potential zone are comparable, but while this value decreases with increasing CV cycles for AN-TiN50/Pt32-100, for the other catalyst it remains roughly constant: this demonstrates a better stability of the catalyst on the TiN60 support;
- The obtained ECSA are extremely different, with the value for AN-TiN60/Pt32-100 being almost three time higher than the one for the other catalyst: while for the former the mean ECSA is 6 m^2/g_{Pt}, for the latter it is 2,5 m^2/g_{Pt}. This increase is attributed to two factors: the first is the superior porosity of the AN-TiN60 catalyst, which allows a better dispersion of the catalyst nanoparticles and assures a more efficient coverage of the whole surface area of the nanostructures. The second factor is the the presence, for the AN-TiN50 substrate, of an oxidation peak at ~0,65 V that hides the real double layer current. The hypothesized origin of such peak is a carbon contamination for AN-TiN50/Pt32-100.

Consequently, AN-TiN60 is chosen as support materials for the following electrodepositions, because it has higher ECSA and it doesn't show the same contamination affecting the AN-TiN50 film. These features can surely help in maximizing the performance and the activity of the final catalyst.

4.8. Platinum Electrodeposition – Current On-Time Optimization

In electrodeposition, the deposit properties are strictly related to the pulsed current parameters: in particular, the crystallization of the deposited metal particles involves the incorporation of adsorbed atoms in the crystal lattice. This phenomenon occurs through two mechanisms:

- Formation of new metallic crystals: this mechanism is favorited by a high adsorbed atoms density and high applied voltage;
- Building up of old crystals, which depends on the surface diffusion rate of the metal. [34]

The formation of new crystal is directly influenced by the applied electrical bias: increasing the intensity of the applied current and decreasing the on-time pulse, the nucleation rate increases, resulting in finer crystals. In addition, by decreasing the on-time pulse the deposited metal particles have less time to organize onto the substrate, which results in a decrease of the mean diameter of the deposited particles. On the other hand, by increasing the on-time pulse the particles have more time to reorganize and the probability of depositing bigger metal clusters composed of many particles increases: since the clusters have a bigger mean diameter, this would result in a lower catalytic area.

The last step in the implementation of the electrodepositions consists in optimizing the pulse on-time, based on the considerations done in the previous paragraph. With a total deposited charge of 32 C/cm^2, constant, the on-time is varied between 50 ms and 100 ms and the influence of this parameter on the performance of the catalyst is investigated.

To summarize, this optimization step consists of:

I. Electrodeposition of the Pt catalyst. This is performed with the same experimental setup of section 4.3 The total deposited charge is 32 C/cm^2 and the current off-time pulse are 500 ms, constant. The pulse on-time is varied between 50 ms and 100 ms;
II. Electrochemical testing is carried out through cyclic voltammograms: CVs are performed in 0.5 M H_2SO_4 solution between 0 V and 1,3 V with a scan rate of 150 mV/s. The 10th,60th and 110th CV scans are plotted, and the ECSA of the catalyst and its evolution during cycling is reported.

Since at this point we are still interested in maximizing the catalytic area no test is carried out in H_2SO_4 + CH_3OH solution: the performance analysis of the catalyst towards MOR will be analyzed when the optimization of the TiN/Pt catalyst will be concluded.

By changing the pulse on-time, we expect to see a change in the ECSA of the catalyst as a consequence of the different mean diameter obtained for the deposited particles: when the on-time is decrease, the Pt deposit has less time to reorganize on the TiN support and is less likely to form bigger assemblies, with a decrease in the mean particle size. Therefore, with an on-time of 50 ms, we expect to see the biggest ECSA.

The fabricated catalysts, named AN-TiN60/Pt32-100 and AN-TiN60/Pt32-50 (for the one deposited with the on-time of 50 ms) are tested according to the protocol pointed out before. The resulting CV plots in 0.5 M H_2SO_4, and a comparison between the two 110th scans of the catalysts, are shown in figure 50 and 51.

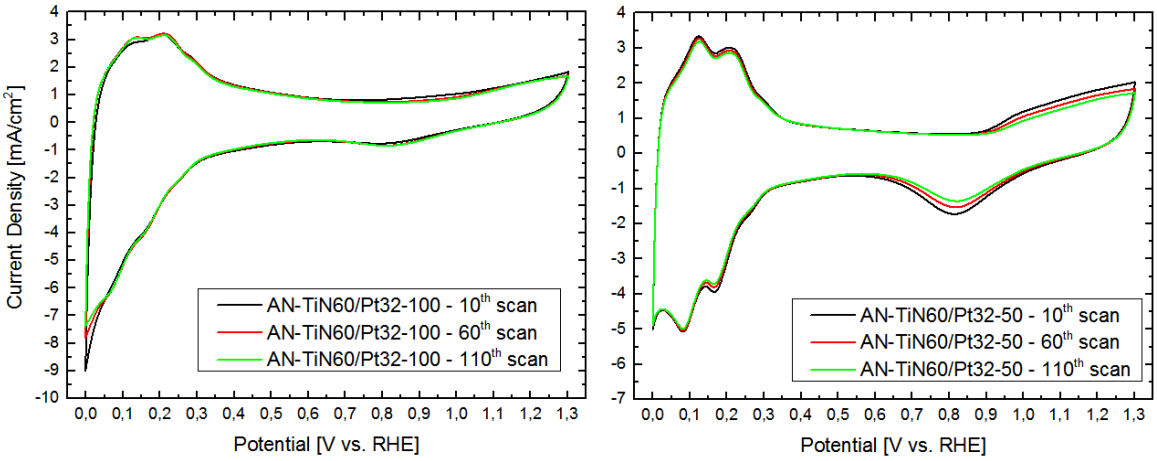

Figure 50: CV plots for AN-TiN60/Pt32-100 (left) and AN-TiN60/Pt32-50 (right). Electrolyte: 0.5 M H_2SO_4. Scan rate: 150 mV/s

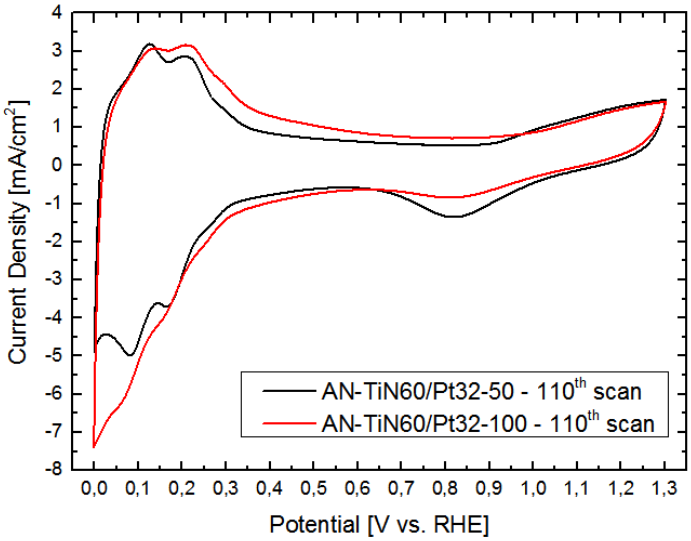

Figure 51: 110th CV scan comparison for AN-TiN60/Pt32-100 and AN-TiN60/Pt32-50

The first qualitative consideration that can be done is that both catalyst are quite stable after extensive testing, meaning that no important decrease in the current density is observed after 110 cycles. The higher current density in the low potential region for AN-TiN60/Pt32-100 suggests that a bigger quantity of hydrogen is adsorbed on Pt, i.e. the catalytic activity seems

higher. On the other hand, AN-TiN60/Pt32-50 shows a better behavior of the other catalyst: the hydrogen adsorption/desorption peaks are more well-defined and not convoluted, which hints to a better activity of all the Pt facets. The reduction peak of the Pt oxides at 0,8 V is more defined, a feature attribute to an improved removal of impurities and a re-crystallization of platinum taking place when the potential reaches high values during CV.

By elaborating the CV plots, the ECSA of the two catalysts are calculated and the results are shown in figure 52, where the error bars due to the measurement uncertainty are included, and in figure 53, where the evolution of the two ECSAs along cycling is compared.

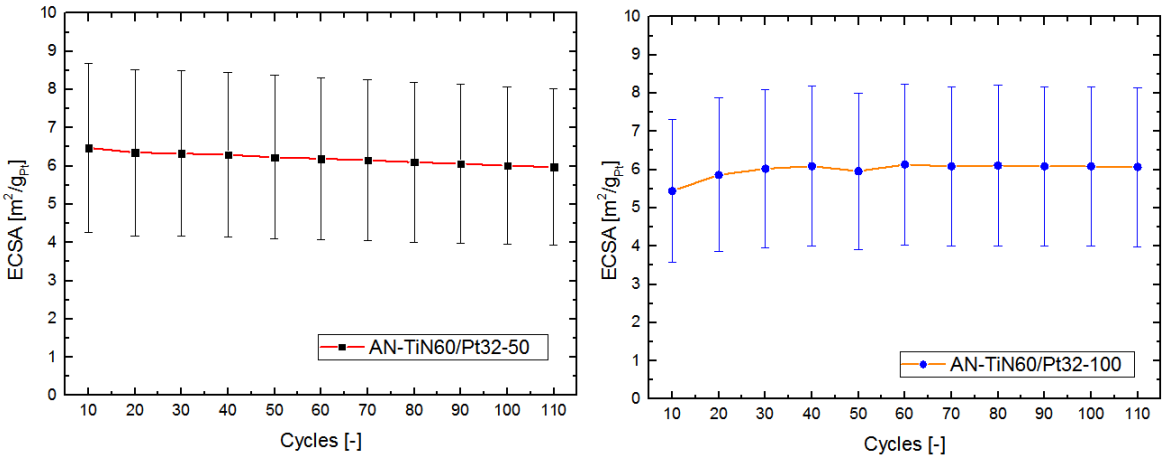

Figure 52: ECSA evolution during cycling for AN-TiN60/Pt32-50 (left) and AN-TiN60/Pt32-100 (right). Error bars are included.

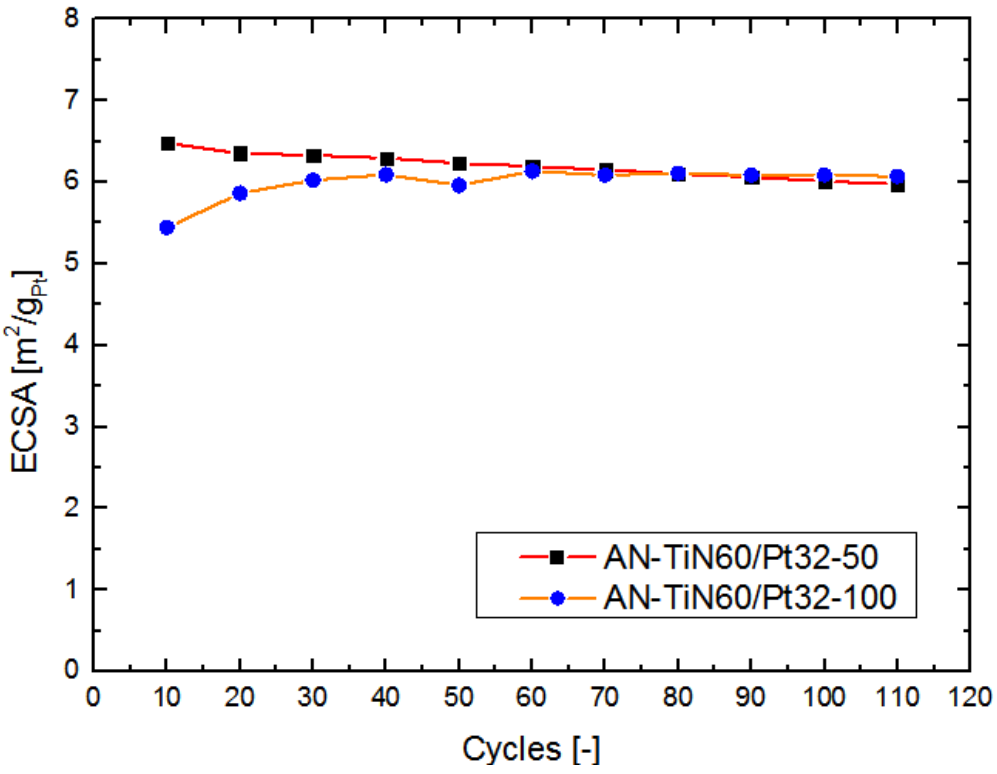

Figure 53: ECSA comparison for AN-TiN60/Pt32-50 and AN-TiN60/Pt32-100

The two catalysts show small but important differences in behavior:

- **ECSA magnitude**: AN-TiN60/Pt32-50 has a higher ECSA than AN-TiN60/Pt32-100 for the first 80 CV scans until the 80th CV scan, with a decreasing difference between the two values. After 80 scans however the situation changes and AN-TiN60/Pt32-100 is the catalyst with bigger ECSA;
- **ECSA variation**: here the behavior of the two catalysts is the opposite. AN-TiN60/Pt32-50 shows a decreasing ECSA with increasing CV cycles – a feature shared with other PEM Pt-based catalysts studied in the literature [27] – with a total ECSA reduction of ∼8% after 110 CV cycles, corresponding to a decrease from 6,48 m^2/g_{Pt} after 10 cycles to ∼5,98 m^2/g_{Pt} at the 110th cycle.
  On the other hand the ECSA of AN-TiN60/Pt32-100 increases with increasing CV scans, going from 5,44 m^2/g_{Pt} after 10 scans to 6,07 m^2/g_{Pt} after 110 scans with a total gain of 11,6%. This behavior influences the overall performance of the catalyst: while the ECSA of AN-TiN60/Pt32-50 gets smaller, the one of AN-TiN60/Pt32-100 is almost constant from the 60th cycle onward, resulting in an overall bigger ECSA value after 80 scans.

With this analysis of the CV plots of the catalysts and the evolution of their ECSA through cycling, AN-TiN60/Pt32-50 is chosen as most suitable catalyst for MOR instead of AN-TiN60/Pt32-100: despite the final ECSA value of the latter is higher than the one of the former, the final increase of 1% is too small if compared with the lower surface area – and therefore worse performance – shown by AN-TiN60/Pt32-100 during the first 80 CV scans. For this reason, the chosen pulse on-time is 50 ms and it is the one that will be implemented in the fabrication of the final catalyst.

Chapter 5

Final Testing of the TiN-Supported Pt Catalyst

5.1. Testing Protocol for the TiN/Pt Catalyst

As a result of all the optimization steps carried out in chapters 3 and 4, the final recipe for the fabrication of the catalyst is established and is here reported:

- **Support**: TiN deposited with a background N_2 pressure of 60 Pa and annealed at 500°C for 4 hours in vacuum, with a length of 1 µm, named AN-TiN60;
- **Catalyst loading**: total deposited charge of 32 C/cm^2, corresponding to an averaged platinum loading of 0,2865 mg$_{Pt}$/cm^2;
- **Electrodeposition parameters**:
  - *Current pulse intensity:* 50 mA/cm^2;
  - *Current pulse on-time*: 50 ms;
  - *Current pulse off-time*: 500 ms.

Now that the process is optimized, the last goal of this work is to characterize the catalyst and investigate the variation of its performance throughout extensive electrochemical testing, in order to compare its working lifetime with other TiN-based catalysts studied in literature and carbon-based materials available for commercial DMFCs. This final investigation and "full life" characterization takes place with the following testing protocol:

I. SEM & XRD analysis for the pristine catalyst;
II. For the first phase of electrochemical testing, two identical AN-TiN60/Pt32-50 catalyst are fabricated. The first, named AN-TiN60/Pt32-50#1 is tested through CVs in acid. The second, named AN-TiN60/Pt32-50#1 is tested through CVs and LSV in methanol. The objective of this first electrochemical testing is to investigate the active area and the MOR performance, respectively, of the pristine catalyst;
III. Both catalyst, after electrochemical testing, are once again physically analyzed through X-Ray Diffraction;
IV. In the second phase of electrochemical testing, the catalyst previously cycled in methanol (AN-TiN60/Pt32-50#2) undergoes cyclic voltammetry analysis in 0.5 M H_2SO_4. This experiment is carried out to understand how the potential sweeping and the interaction between catalyst and methanol modifies the ECSA of the catalyst, in comparison to a pristine situation;
V. A final XRD analysis on AN-TiN60/Pt32-50#2 is performed to understand if the repeated cycling influences the morphological properties of the material;
VI. In conclusion, AN-TiN60/Pt32-50#2 is cycled once again in 0.5 M H_2SO_4 + 1 M CH_3OH, to evaluate the performance of the catalyst towards MOR after the previous extensive cyclic voltammograms, and how the electrochemical testing modifies the activity of the catalyst towards methanol.

In order to assess the efficiency and the activity of the AN-TiN60/Pt32-50 catalyst, the following parameters, extrapolated from the CV scans, are used:

- **ECSA***:* the electrochemical surface area of the catalyst is calculated from the CV plots in 0.5 M H_2SO_4 solution with the procedure explained in section 2.2.4 and expanded in Appendix A.2;
- **ΔE***:* the potential separation between the peaks in the forward scan and backwards scan in a methanol-containing electrolyte has been used in literature as an activity parameter for the catalyst in literature [48]. The lower the ΔE, the better. This value is ∼200 mV at a scan rate of 50 mV/s for a pure Pt catalyst [24];
- $\mathbf{I_{ratio}}$*:* the ratio between the forward peak current and the backwards peak current has been employed extensively in the literature as an indicator of the CO tolerance of the catalyst [49], since the backwards peak current is often associated to the oxidation of the CO intermediate.

Regarding this last parameter, it is extremely important to point out that the nature of the current peak in the reverse scan is still debated, and many studies reject its interpretation as oxidation of the CO intermediate [50]. In particular, a recent study by Chung, Lee and Sung [51] suggests that the backwards peak is related to the oxidation of the adsorbed –OH species (inactive towards MOR) on Pt surface and the oxidation of fresh adsorbed methanol on the just-freed Pt sites. With this interpretation, the I_{ratio} is not employed as catalyst CO tolerance criterion, but as an indicator of the oxophilicity – that is, the easiness to form oxygenated species – of the catalyst: a high I_{ratio} indicates a behavior similar to a PtRu/C catalyst (which is known to be easily oxidized) therefore a good performance towards MOR.

Despite this debate, to compare the MOR performance of the TiN/Pt catalyst with other reference catalyst for DMFC in the same testing conditions, cyclic voltammetry with a scan rate of 50 mV/s is implemented as experiment. The final goal of these tests and comparisons is to investigate how the presence of TiN affects the performance of Pt, in particular the main objective is understanding how the physical properties of TiN and its tendency to form hydroxides can be exploited in order to lower the ruthenium loading in the anode catalytic layer while still inhibiting the CO poisoning of Pt.

5.2. Morphological Analysis of the Pristine Catalyst

After the fabrication of AN-TiN60/Pt32-50#1 and #2, an X-Ray diffraction spectrum of the material is recorded and high-resolution SEM top views are taken to analyze the morphology of the catalyst.

The XRD spectrum of the catalyst is presented in figure 55, where the reference peaks of TiN and Pt crystalline planes are also reported, while the HR-SEM images are in figure 54. For the SEM images, two magnification are reported: the higher one is reported to show the presence of Pt nanoparticles on the TiN support, while the lower one, highlights the morphological structure of the support after electrodeposition.

By comparing figure 54 with the SEM images reported in sections 3.2. and 3.3. for the bare TiN support, a complete change in the morphology of the nanostructure can be observed: while after deposition and annealing the TiN scaffold had a tree-like shape with a tip that appears round from a top view (figure 23), after electrodeposition the scaffold assumes a lamellar structure, with a modification in the tips of the nanotrees showing a directional growth of the nanostructure. This modification takes probably place during the electrodeposition of the catalyst, but the explanation of the phenomenon affecting TiN is yet to be investigated.

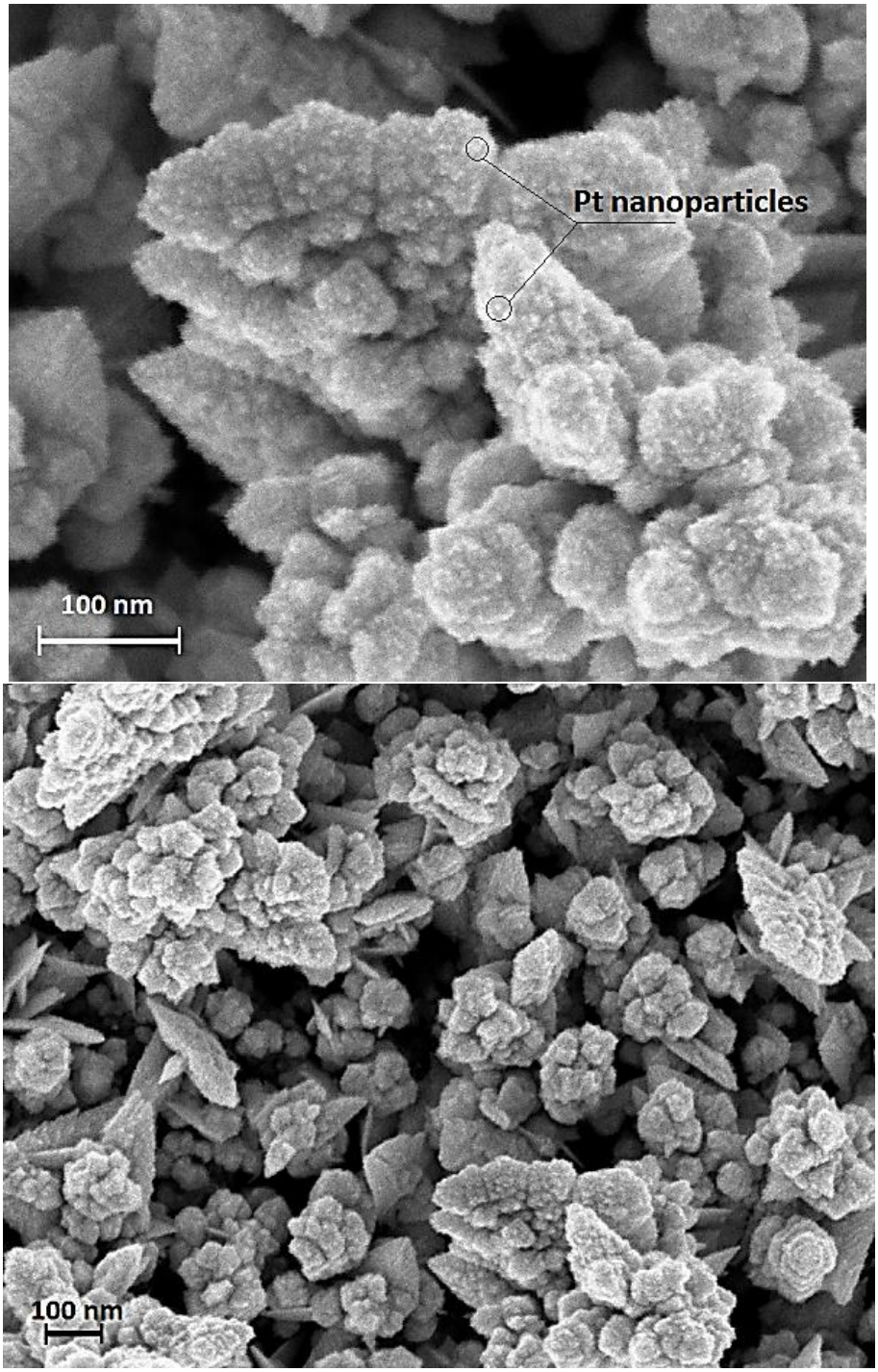

Figure 54: HR-SEM top view images of pristine AN-TiN60/Pt32-50 catalyst at different magnifications

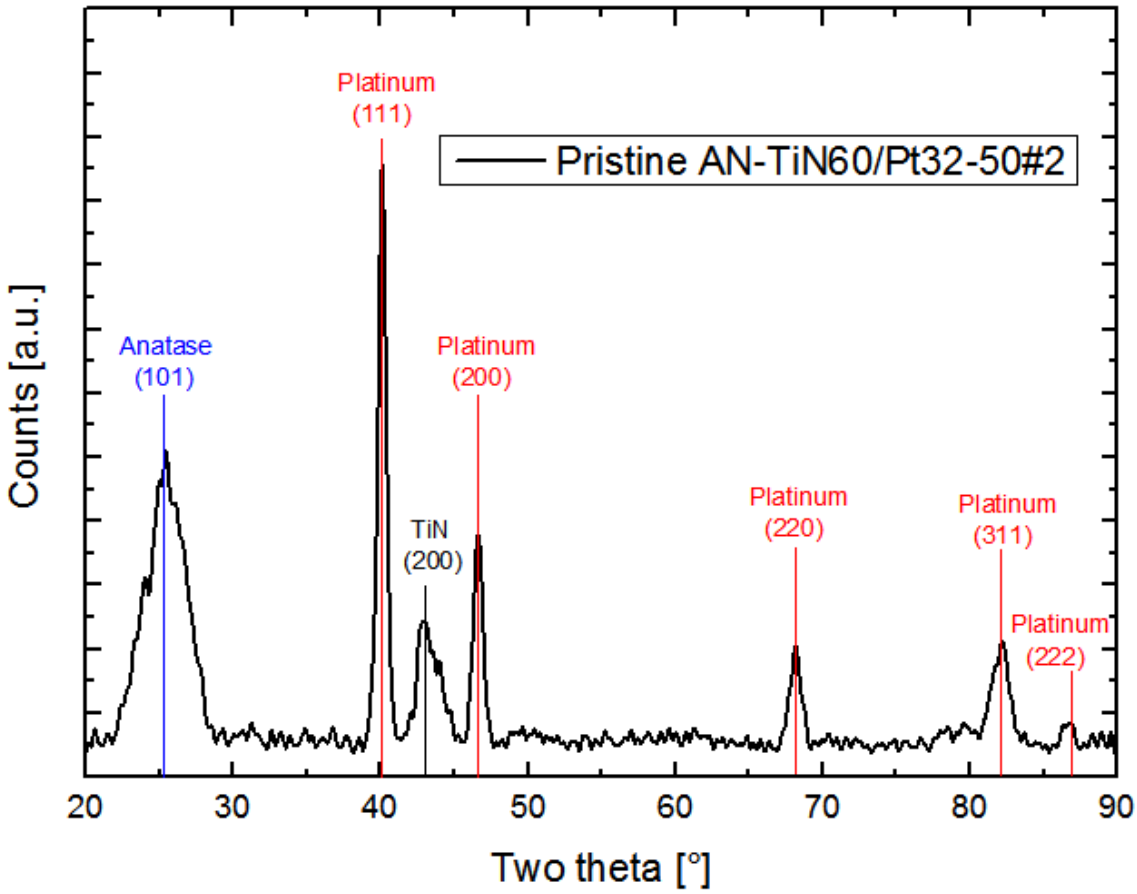

Figure 55: XRD spectrum of the pristine AN-TiN60/Pt32-50 catalyst

5.3. Electrochemical Characterization of the Pristine Catalyst

The first step of the electrochemical characterization is the cycling of the two copies of the catalyst – that are nominally identical – in different electrolytes, 0.5 M H_2SO_4 and 0.5 M H_2SO_4 + 1 M CH_3OH. The cyclic voltammograms are performed with the procedure already employed in chapter 4, and the 10^{th}, 60^{th} and 110^{th} scans are reported in figure 56.

The CV curves in the left picture show the usual features of a Pt catalyst in acid solution, with the hydrogen adsorption/desorption peaks at low potential, the onset of Pt oxidation at ~0,9 V, the oxidation of surface impurities at the highest potentials and, lastly, the Pt oxides reduction peak in the reverse scan at ~0,85 V. We notice a decrease in the oxidation current at 1,3 V, corresponding to the elimination of impurities through cycling.

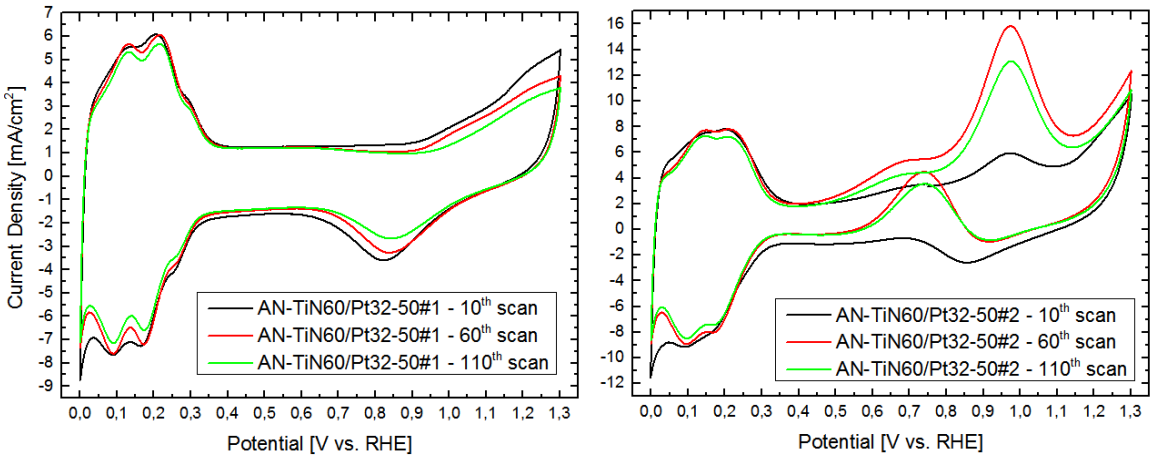

Figure 56: CV plots for the two AN-TiN60/Pt32-50 catalysts. Electrolyte: 0.5 M H_2SO_4 (left), 0.5 M H_2SO_4 + 1 M CH_3OH (right). Scan rate: 150 mv/s

The voltammograms in 0.5 M H_2SO_4 + 1 M CH_3OH reveal many information when it comes to the high potential region, while the low-potential region, for all the three different plotted cycles, still shows the same features discussed in the previous paragraph.

For all plotted cycles an oxidation peak at ~0,95 V, connected to the methanol oxidation on Pt active sites, can be seen; the magnitude of the peak oxidation current, however, increases with increasing cycles ranging from 5,94 mA/cm^2 after 10 scans to 15,8 mA/cm^2 after 110 scans, with an almost threefold increase. This phenomenon can be explained with an activation of the Pt catalyst throughout cycling. The main MOR peak is followed by the onset of another oxidation reaction at ~1,1 V. This reaction, which is stopped when the scan is reversed, is attributed to the methanol oxidation not on platinum, but on Pt-oxides active sites, as explained by the model proposed in [51]: the reaction can't be completely attributed to the oxidation of impurities, differently than the other sample, because the peak oxidation current for AN-TiN60/Pt32-50#2 is three times higher. When the scan is reversed, firstly a reduction current peak is observed between 0,85 V and 0,9 V, followed by another oxidation reaction at ~0,75 V whose current increases with increasing cycles, similarly to what happens for the MOR peak at 1,1 V: according to [51], this is caused by the oxidation of a surface –OH layer on the Pt catalyst (which creates from Pt oxides at ~1 V in the reverse scan) and the migration of fresh methanol on the free Pt active sites. Lastly, the onset of another oxidation reaction can be observed, for the 60th and 110th scan, at 0,45 V: since this reaction is absent in the 10th scan and at that potential the oxidation of CO begins [5] – although with a slow reaction rate – we hypothesize the peak is related to the oxidation of CO generated by the oxidation of methanol in the previous cycle.

After the analysis of the CV plots, the activity parameters for the catalyst are plotted. The ECSA evolution through cycling of the AN-TiN60/Pt32-50 pristine catalyst is shown in figure 57.

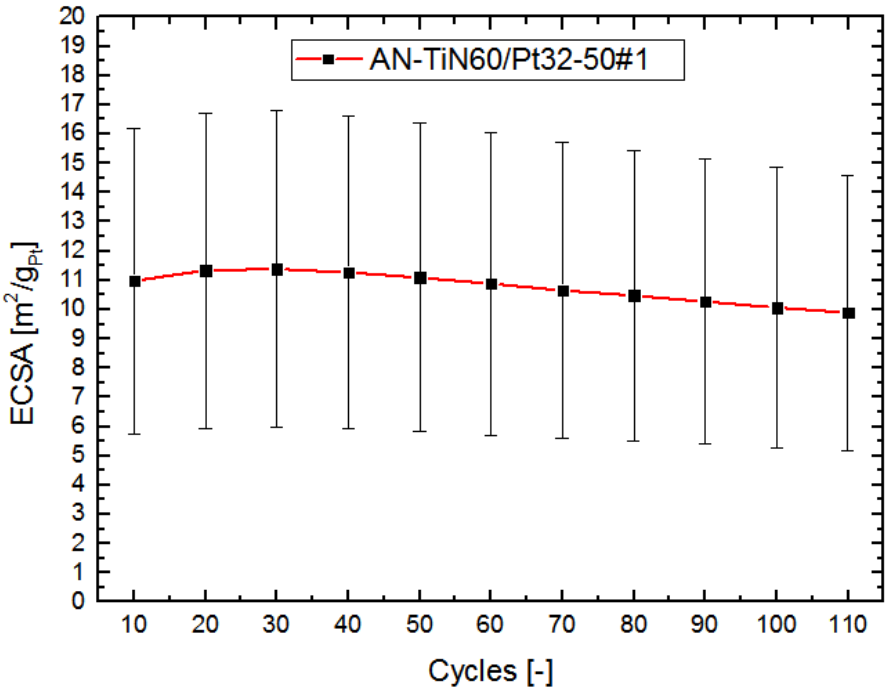

Figure 57: Pristine AN-TiN60/Pt32-50 ECSA evolution. Error bars due to faradaic efficiency of electrodeposition are included

Similarly to the AN-TiN60/Pt32-100 catalyst tested in section 4.7, pristine AN-TiN60/Pt32-50#1 shows an activation effect leading to an ECSA increase in the first 20 CV scans. After that, however, the active area slowly decreases, with a rate of approximately 0,02 m^2/cycle: this decrease is probably due to the island effect that affects the TiN support and already observed in the previously-fabricated materials.

After that, the MOR performance evaluation criterions are plotted in figure 58, along with the CV plot for the catalyst, acquired with a scan rate of 50 mV/s. These scans are performed after the catalyst has been cycled 60 times in the same electrolyte with a scan rate of 150 mV/s, therefore already indicate a stabilized behavior of the catalyst with respect to the potential sweeping and the acidic environment.

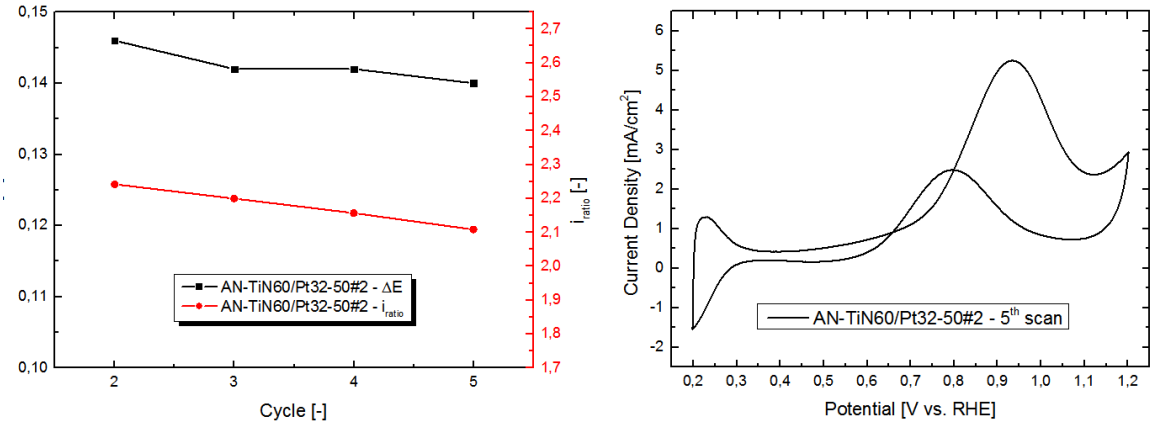

Figure 58: ΔE and I_{ratio} for the pristine AN-TiN60/Pt32-50#2 catalyst (left) and CV plot in 0.5 M H_2SO_4 + 1 M CH_3OH (right). Scan rate: 50 mV/s

The CV plot in the right shows the same features of the scan reported in figure 56, which will therefore be not discussed again. On the other hand, the ΔE and the I_{ratio} for the pristine catalyst give new insights on the catalytic efficiency of pristine AN-TiN60/Pt32-50: ΔE, the separation between the forward and backwards oxidation peaks, remains approximately constant at ~142 mV and the I_{ratio}, linked to the degree of oxophilicity of the catalyst, is ~2,2. In table 5 the values obtained for the AN-TiN60/Pt32-50 catalyst are benchmarked against a commercial E-TEK catalyst (Pt 20% on Vulcan carbon) and pure Pt.

	TiN60/Pt50	E-TEK	Pure Pt
I ratio [-]	2,24-2,10	1,04 [51]	1 [52]
ΔE [mV]	146-140	200	200

Table 5: comparison of MOR performance indicators for AN-TiN60/Pt32-50 and commercial catalysts

The comparison shows that the pristine catalyst shows a better performance than a pure Pt catalyst and E-TEK, with a dramatic increase in the I_{ratio} – which indicates a better capability of the catalyst to oxidize the –OH surface layer on the Pt particles – and a decrease in the separation between the two oxidation peaks, corresponding to a good performance towards the MOR.

5.4. Morphological Analysis After the First Cycling

After the first round of CV scans, the morphology of the two cycled AN-TiN60/Pt32-50 catalysts is studied one more time to investigate potential changes in the nanostructure caused by the electrochemical testing. Firstly, the XRD spectra of the catalyst are reported in figure 59.

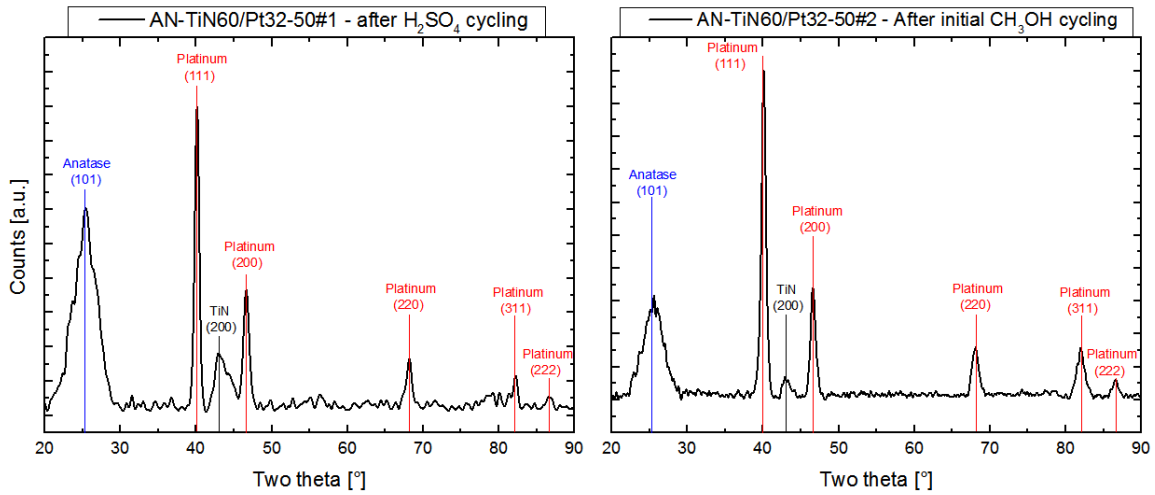

Figure 59: XRD spectra for AN-TiN60/Pt32-50#1 (left) and AN-TiN60/Pt32-50#2 (right)

In table 6 the variation of the Pt crystalline grains and of the lattice strain with electrochemical testing is reported: we want to investigate how different electrolytes influence the morphology and the mechanical properties of the catalyst particles, and how this variations influence the second phase of electrochemical testing.

	Pt (111)	Pt (200)	Pt (220)	Pt (311)	Pt (222)	Strain
	[Å]	*[Å]*	*[Å]*	*[Å]*	*[Å]*	*[%]*
Pristine TiN60/Pt50	147,1	118,1	120,3	83,2	149,4	11,09
TiN60/Pt50 – after H_2SO_4 cycling	137,3	110	143	186,8	205,3	8,36
TiN60/Pt50 – after CH_3OH cycling	131,5	118,5	104,2	140,6	123,9	8,44

Table 6: Crystalline size and lattice strain variation for Pt particles through electrochemical testing

While for the lattice strain, and for the Pt (111) plane, the electrolyte has no influence, since the same trend is observed – both values decrease in comparison with the pristine catalyst – the two electrolytes change in different ways the other lattice parameters:

- Cycling in methanol decrease the width of the (220) and (222) planes, while this value increases after cycling in sulfuric acid;
- The width of the Pt (311) plane is higher after both acid and methanol cycling, but with different increases: +225% for acid cycling, +169% for methanol cycling.

For both electrolytes, a decrease in the Pt lattice strain is observed, as a consequence of the relaxation of the nanoparticles caused by cycling and its effect on the Pt nanoparticles.

5.5. Stability Analysis for AN-TiN60/Pt32-50 Catalyst

The catalyst that was cycled in methanol in section 5.3, that is, AN-TiN60/Pt32-50#2 is again tested electrochemically after the XRD analysis. This time the catalyst is cycled in 0.5 M H_2SO_4, to understand how the potential sweeping and the interaction with methanol modify the ECSA of the catalyst, in comparison with the pristine situation. The 10^{th}, 60^{th} and 110^{th} scan in 0.5 M H_2SO_4 – which are the overall 120^{th},170^{th} and 220^{th} CV cycles for the catalyst – are plotted in figure 60.

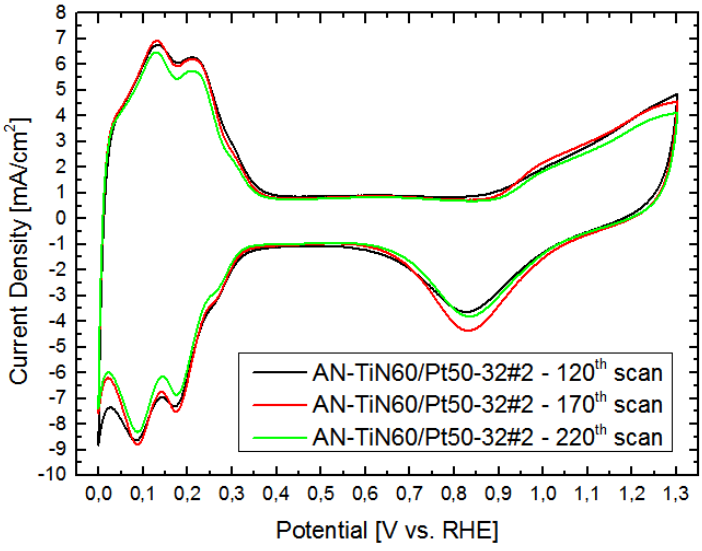

Figure 60: CV plots for AN-TiN60/Pt32-50#2. Electrolyte: 0.5 M H_2SO_4. Scan rate: 150 mV/s

In figure 61 the 220th CV scan of AN-TiN60/Pt32-50#2 is compared to the 110th scan of AN-TiN60/Pt32-50#1, and the ECSA of the two catalysts are plotted.

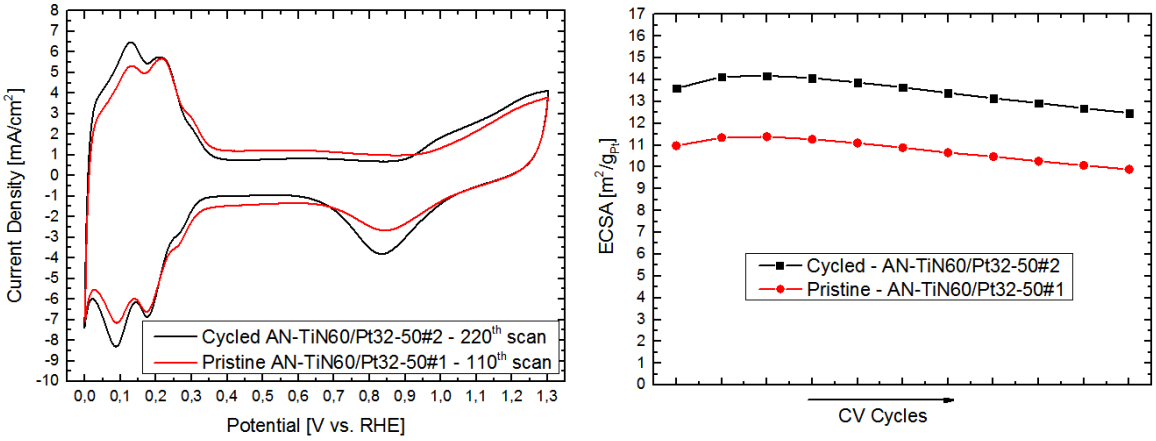

Figure 61 LEFT: Comparison for the last CV scan for AN-TiN60/Pt32-50#1 and #2. RIGHT: ECSA evolution of AN-TiN60/Pt32-50#1 and #2

Despite the previous CV scans in 0.5 M H_2SO_4 + 1 M CH_3OH, the cycled catalyst exhibits a better ECSA value than the pristine catalyst, with a medium increase in magnitude of ~25%. The ECSA evolution trend through cycling is the same for both catalysts, as can be inferred from the CV scan comparison, because the same current peaks can be spotted, although with different intensities. This result is extremely interesting, because after cycling in methanol – which should negatively affect the performance and activity of the catalyst – no worsening in the activity can be seen.

This effect can be caused by the reduced double-layer current of the cycled AN-TiN60/Pt32-50#2 in comparison with the pristine catalyst, which increases the hydrogen desorption area at low voltage, and by the smaller oxidation current at potentials above 0,9 V, probably due to the smaller impurities on the film and to the littler Pt oxidation taking place at high potential.

After electrochemical testing, AN-TiN60/Pt32-50#2 is again structurally studied through X-Ray Diffraction. The resulting spectrum is plotted in figure 62, along with a comparison of the resulting spectrum with the XRD pattern recorder after the first cycling in methanol for AN-TiN60/Pt32-50#2.

The comparison between the two XRD spectra show no evident change in the diffraction peaks, in width nor in intensity, of the catalyst before and after the second CV test in 0.5 M H_2SO_4.

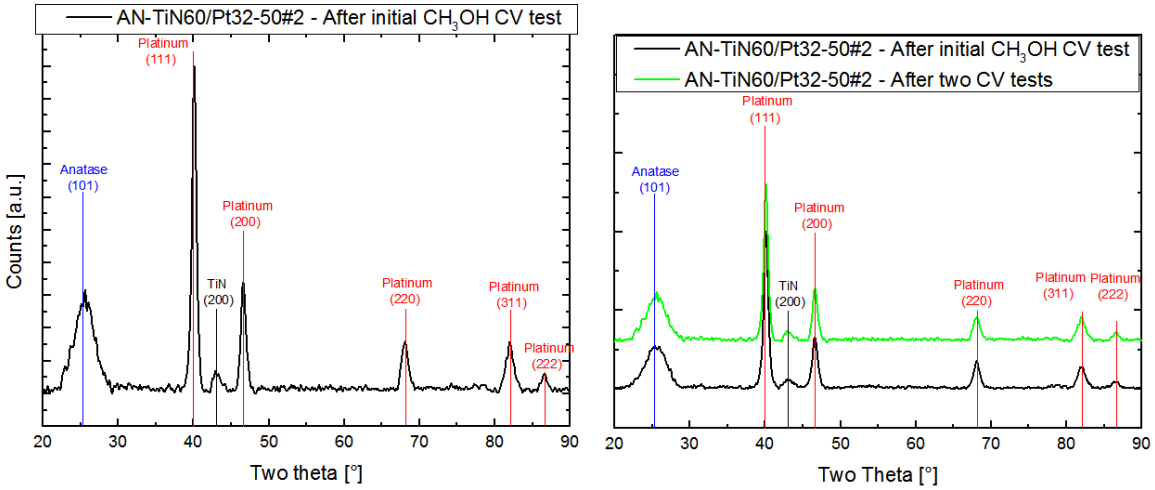

Figure 62 LEFT: XRD spectrum for cycled AN-TiN60/Pt32-50#2. RIGHT: XRD spectra comparison for AN-TiN60/Pt32-50#2, before and after the second CV test in 0.5 M H_2SO_4

As already reported for the previously-plotted XRD spectra, the size variation of the Pt crystalline planes and of the Pt lattice strain with successive electrochemical testing is described in table 7.

	Pt (111)	Pt (200)	Pt (220)	Pt (311)	Pt (222)	Strain
	[Å]	*[Å]*	*[Å]*	*[Å]*	*[Å]*	*[%]*
Pristine TiN60/Pt50	147,1	118,1	120,3	83,2	149,4	11,09
AN-TiN60/Pt32-50 – after initial CH_3OH cycling	131,5	118,5	104,2	140,6	123,9	8,44
AN-TiN60/Pt32-50 – after two CV test	128,3	110,3	118,3	102,4	253,8	7,38

Table 7: Crystalline size and lattice strain variation for Pt particles through electrochemical testing

With consecutive electrochemical testing, a decrease in the Pt lattice strain – proportional to the number of cycles the catalyst undergoes – is observed: this decrease is ascribed by a relaxation of the Pt lattice due to an increase of the mean particle size with electrochemical testing.

The last experiment performed to evaluate the long-term stability of the AN-TiN60/Pt32-50#2 catalyst is cyclic voltammetry in 0.5 M H_2SO_4 + 1 M CH_3OH. 50 CV cycles are performed with a scan rate of 50 mV/s and the performance parameters for MOR, the potential separation between the forward and backwards current peaks and the ratio between these two peaks, are collected every 5 cycles. The objective of this analysis is understanding how the repeated cycling in different electrolytes influences the activity of the catalyst towards the methanol oxidation and how its performance is affected by prolonged potential sweeping.

The result of the test are shown in figures 63 and 64.

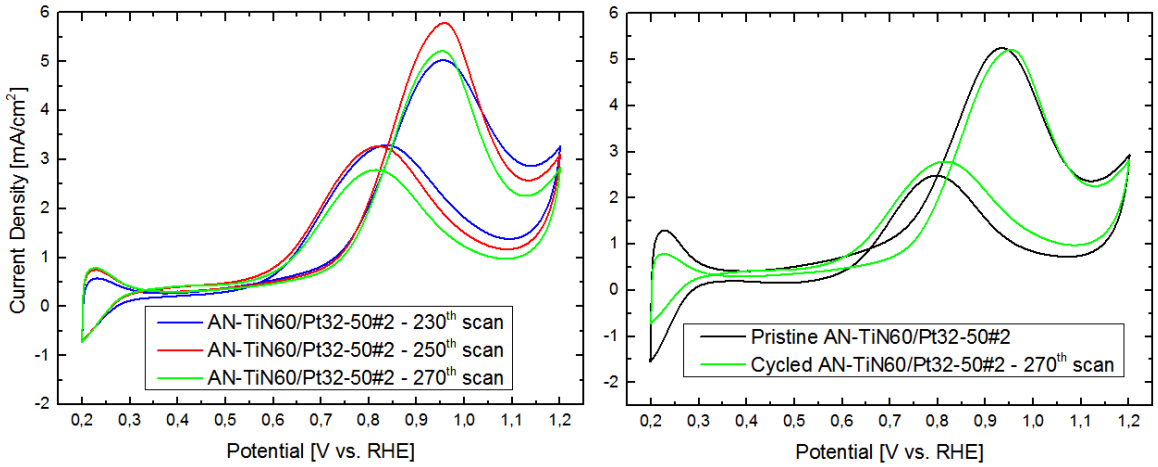

Figure 63 LEFT: CV plot for the cycled AN-TiN60/Pt32-50#2. RIGHT: CV comparison between pristine and cycled AN-TiN60/Pt32-50#2. Electrolyte: 0.5 M H_2SO_4 + 1 M CH_3OH. Scan rate: 50 mV/s.

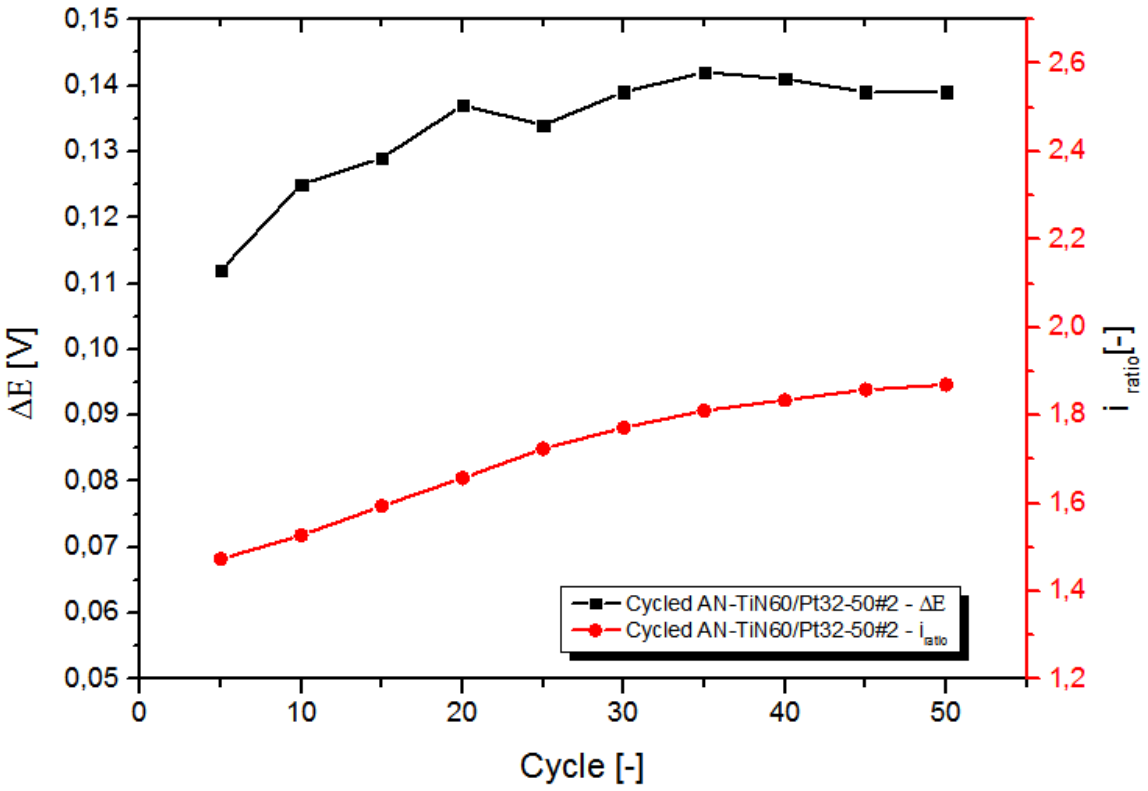

Figure 64: ΔE and I_{ratio} for the cycled AN-TiN60/Pt32-50#2 catalyst

By comparing the CV plots for the catalyst in the two different situation (pristine and cycled) as shown in figure 63, the following considerations can be done:

- The peak current density for the forward scan, related to the oxidation of methanol on Pt active sites, show no visible sign of decrease after extensive cycling;
- The peak current density for the backwards scan, on the contrary, is higher for the cycled situation in comparison to the pristine situation: this information reveals that the performance of the catalyst is negatively influenced by the extensive CV scanning, since a

higher value for this peak means a worse ability of the catalyst to remove the –OH layer that forms on Pt active sites. In other words, this means that the activity of the catalyst towards methanol oxidation decreases;

- Both oxidation peaks slightly shifts to higher potentials after extensive scanning: despite the magnitude of the shift is the same, and the ΔE value show no evident worsening (as reported in table 8), the shift to higher potential indicates a sloppier kinetics of the methanol oxidation reaction, i.e. a higher overpotential is needed for the reaction to start.

The values of the MOR performance indexes for the AN-TiN60/Pt32-50#2, both pristine and cycled, are reported and compared in table 8.

	ΔE_{avg}	ΔE_{max}	ΔE_{min}	$i_{ratio,avg}$	$i_{ratio,max}$	$i_{ratio,min}$
	[V]	[V]	[V]	[-]	[-]	[-]
Pristine AN-TiN60/Pt32-50#2	**0,143**	0,146	0,140	**2,177**	2,240	2,110
Cycled AN-TiN60/Pt32-50#2	**0,134**	0,142	0,112	**1,712**	1,869	1,4733

Table 8: MOR performance indexes for AN-TiN60/Pt32-50#2

From the numerical data, the following considerations can be done:

- ΔE is not affected by the cyclic voltammograms: its value before and after extensive cycling decreases by 6%, but the magnitude of this variation is very small and negligible. It is also noted that despite the potential separation between the two peaks remains almost constant through cycling, both peaks shifts towards higher potential, as previously noted: this phenomenon is related to a worse reaction kinetics after cycling;
- The i_{ratio} also decreases with cycling, with a more substantial variation observed (-21,4%): this decrease is observed despite the current density for the forward peak remains almost constant through cycling. This means that the lower i_{ratio} observed is caused by a higher current density for the backwards peak, i.e. by a reduced ability of the catalyst to free the Pt sites covered by the inactive –OH surface layer, and ultimately by a reduced activity of the catalyst.

Finally, the AN-TiN60/Pt32-50#2 values are compared with the ones reported in literature for commercial catalysts, in order to highlight how the presence of TiN modifies the performance of platinum towards MOR.

	ΔE [mV]	i_{ratio}
Pristine AN-TiN60/Pt32-50#2	143	2,177
Cycled AN-TiN60/Pt32-50#2	134	1,712
E-TEK	200	1,040 [51]
Pure Pt	200 (@25 mV/s)	1 [52]
PtRu/C	200	2,762 [51]
Pt/TiN [24]	70 ± 5	1,26
Pt/TiN [53]	~200	~1,05

Table 9: MOR performance comparison between AN-TiN60/Pt32-50#2 and reference catalysts

From the analysis of the results reported in the table, it is possible to infer that the presence of the TiN support somehow enhances the catalytic performance of Pt towards MOR. Regarding the iratio value, the fabricated TiN/Pt catalyst exhibits a better behavior than the ones reported

in the literature for carbon supported Pt. Moreover it shows a ΔE value lower, and therefore better, than commercial catalysts for DMFC (indicating an enhanced reaction kinetics for MOR) and consistent with the results reported in other studies. Extended CV testing negatively affects the behavior of the catalyst, as expected, but even after the electrochemical testing, the catalyst shows a good behavior.

Conclusions

In this work we fabricated, characterized and optimized a novel support catalyst based on nanostructured, hierarchical titanium nitride scaffolds grown by means of PLD. To achieve this, the following steps are adopted:

- The operating conditions for the scaffold deposition are investigated and optimized: the process gas pressure in the vacuum chamber is varied in order to obtain different scaffold morphologies. An SEM analysis has been carried out to individuate the best option in terms of porosity, which has to be the optimum between high surface area and mechanical stability.

  We individuated the best results for nitrogen pressure of 50 and 60 Pa.

- The chosen samples are physically and electrochemically characterized, in order to evaluate their chemical stability in the reaction environment.

  We show that TiN scaffolds are stable in acidic conditions after annealing in vacuum at 500°C for 4 hours, and confirm that the support is inactive towards MOR.

- A deposition process in order to functionalize the scaffold with active catalytic metal has been developed and optimized. We show that DC sputtering is not effective since the active material is submerged into the nanotrees and does not show activity at all. On the other hand, pulsed electrodeposition seems to be a more suitable way to fabricate the catalyst: it is shown that with an optimized recipe (consisting in a total charge of 32 C/cm^2 and an on/off time of 50/500ms) we achieve an active area as high as 10-14 m^2/g_{Pt}.

- The optimized catalyst has been tested in 0.5M H_2SO_4 + 1M CH_3OH solution in order to evaluate its performances towards MOR. An extended voltammetric analysis has been carried out, showing a good performance according to the literature. In particular, we show that catalyst exhibits a good resistance to extensive electrochemical testing, maintaining an outstanding activity towards the MOR: the ΔE value for the fabricated catalyst is ∼140 mV and the i_{ratio} ranges from 2,18 to 1,71, while the same parameters for an E-TEK catalyst are 200 mV and 1,04. This indicates an enhanced performance of our catalyst and an increased activity towards the MOR and the removal of the reaction intermediates formed. Moreover, in agreement with the results, it is possible to infer that such a scaffold is active towards the oxidation of MOR intermediates, making it a possible candidate to replace the ruthenium co-catalyst, thus solving the Ru crossover issue and decreasing the cost of the electrode.

The morphology change affecting the scaffold during electrodeposition catalyst is still unclear and has to be further investigated, once it's possible to have precise information about the nanotrees' crystallinity and composition, to date not possible due to the huge clusters on the film.

Despite these outstanding results, some criticalities has yet to be solved. First of all the process has to get rid of every possible contamination by external agents (i.e. carbon and, as much as possible, oxygen). Secondly, the defects introduced by the anomalous ablation of the target during deposition could be eliminated through a fine-tuning of the device.

The implications of the results show how PLD could be used to obtain catalysts for fuel cells. The technique holds promises for fabrication of efficient DMFC electrodes, and the combination of the photocatalytic properties of titanium (oxy)nitride and nanotree-like shape of the scaffold with high light harvesting performances can lead to high-performance photocatalysts.

Table of figures

Figure 1: Schematics of a PEMFC 16
Figure 2: Schematics of a DMFC 18
Figure 3: PEMFC and DMFC polarization & power density curves. Modified image. Original from [1] 19
Figure 4: Impedances model for reaction overpotentials. From [2] 22
Figure 5: Current-overpotential equation 27
Figure 6: Polarization curve for a DMFC. The influence of different catalyst composition is compared. From [3] 29
Figure 7: Illustration of a typical PLD vacuum chamber [28] 40
Figure 8: Pressure/morphology relationship for PLD films [28] 42
Figure 9: Pulsed Laser Deposition of the TiN scaffold 43
Figure 10: Phenomena occurring on a target subjected to ion bombardment [33] 44
Figure 11: DC magnetron sputtering system 45
Figure 12: DC magnetron sputtering deposition. Cropped image. Original from: https://en.wikipedia.org/wiki/Sputter_deposition#/media/File:Magnetron_sputtering_source.jpg . CC BY-SA 3.0 (last consultation: 05/07/2016) 45
Figure 13: Waveform for a pulsed electrodeposition technique 47
Figure 14 Two-electrode (left) and three-electrode (right) cell [2] 48
Figure 15: Potential sweep (left) & resulting current/potential curve (right) during a LSV experiment 49
Figure 16: Potential-time signal for a CV experiment [36] 50
Figure 17: Typical form of a CV scan for a redox couple 51
Figure 18: Typical CV plot for a Pt electrode in H2SO4 [37]**.** The effect of repeated scans (increasing numbers for the plots) is highlighted. 52
Figure 19: CV in H_2SO_4 for a Pt catalyst. The hydrogen desorption area for ECSA calculation is highlighted in cyan 53
Figure 20: schematics of an XRD experimental setup 54
Figure 21: Energy states involved in Raman scattering 56
Figure 22: SEM top views for the as deposited TiN samples. A: AD-TiN 30 Pa, B: AD-TiN 40 Pa, C: AD-TiN 50 Pa, D: AD-TiN 60 Pa, E: AD-TiN 80 Pa 60
Figure 23: SEM top views for the annealed TiN samples. A: AN-TiN30, B: AN- TiN40, C: AN-TiN50, D: AN-TiN60, E: AN-TiN80 61
Figure 24: SEM cross-section for A: AD-TiN50, B: AN-TiN50, C: AD-TiN60, D: AN-TiN60 63
Figure 25: Raman spectra for as deposited (left) and annealed (right) TiN50 & TiN60. Anatase reference plotted 64
Figure 26: Raman spectra for TiN50 (left) and TiN60 (right). Anatase reference plotted 64
Figure 27: XRD spectra comparison for TiN50 and TiN60. TiN reference XRD peaks are reported. 66
Figure 28 Left: SEM top view of droplets deposited on top of the TiN film. Right: close-up of a droplet crushing the TiN film 67
Figure 29: CV comparison for AD-TiN50 (left) and AD-TiN60 (right). Electrolyte: 0.5 M H_2SO_4. Scan rate: 150 mV/s 68
Figure 30: CV comparison for AN-TiN50 (left) and AN-TiN60 (right). Electrolyte: 0.5 M H_2SO_4. Scan rate: 150 mV/s 69
Figure 31: Comparison between as deposited and annealed TiN film. Left: AD-TiN50 vs AN-TiN50. Right: AD-TiN60 vs AN-TiN60. Electrolyte: 0.5 M H_2SO_4. Scan rate: 150 mV/s 70

Figure 32: CV plot for AD-TiN50 and AN-TiN50. Scan rate: 150 mV/s. Electrolyte: 0.5 M H_2SO_4+ 1 M CH_3OH 71
Figure 33: 110th CV scan for AN-TiN50 and AN-TiN60. Scan rate: 150 mV/s. Electrolyte: 0.5 M H_2SO_4 72
Figure 34: HR-SEM image of AD-TiN50 sample after CV scans in 0.5 M H_2SO_4 73
Figure 35: HR-SEM image of AN-TiN50 sample after CV scans in 0.5 M H_2SO_4 73
Figure 36: CV plots for PtRu-GC (left) and PtRu-FTO (right). Scan rate: 150 mV/s. Electrolyte: 0.5 M H_2SO_4 + 1 M CH_3OH 76
Figure 37: LSV for PtRu-GC (red line) and PtRu-FTO (black line). Scan rate: 10 mV/s. Electrolyte: 0.5 M H_2SO_4 + 1 M CH_3OH 77
Figure 38: HR-SEM cross-section for AD-TiN/PtRu (top) and AN-TiN/PtRu (bottom) 78
Figure 39: Cv plots for AD-TiN/PtRu (left) and AN-TiN/PtRu (right). Scan rate: 150 mV/s. Electrolyte: 0.5 M H_2SO_4 + 1 M CH_3OH 79
Figure 40: CV comparison between the as deposited (left) and annealed (right) TiN vs. TiN/PtRu. Scan rate: 150 mV/s. Electrolyte: 0.5 M H2SO4 + 1 M CH3OH 79
Figure 41: current pulses for the reference electrodeposition recipe 81
Figure 42: CV scans (left: 10th cycle, right: 60th and 110th cycle) for AD-TiN50/Pt8-50. Scan rate: 150 mV/s. Electrolyte: 0.5 M H_2SO_4 82
Figure 43: CV plots for AN-TiN/Pt16-50 catalyst. Electrolyte: 0.5 M H_2SO_4. Scan rate: 150 mV/s. The catalyst features are highlighted. 84
Figure 44: CV plots for different deposited charges: 8 C/cm^2 (top left), 16 C/cm^2 (top right), 32 C/cm^2 (bottom left), 64 C/cm^2 (bottom right). Scan rate: 150 mV/s. Electrolyte solution: 0.5 M H_2SO_4. 86
Figure 45: ECSA variation during CV scans for the four catalyst 88
Figure 46: HR-SEM top view for AN-TiN50/Pt16-100 after CV scans 89
Figure 47: TOP: HR-SEM top view for AN-TiN50/Pt64-100 before CV. BOTTOM LEFT: higher magnification, highlighting Pt nanoclusters. BOTTOM RIGHT: higher magnification, highlighting Pt nanoparticle 90
Figure 48 TOP LEFT: SEM top view of AN-TiN50. TOP RIGHT: SEM top view of AN-TiN60. BOTTOM LEFT: CVs for AN-TiN50. BOTTOM RIGHT: CVs for AN-TiN60. Electrolyte: 0.5 M H_2SO_4. Scan rate: 150 mV/s 93
Figure 49: Top: CV plots for AN-TiN50/Pt32-100 and AN-TiN60/Pt32-100. Bottom left: 110th scan comparison for the two catalyst. Bottom right: ECSA comparison 94
Figure 50: CV plots for AN-TiN60/Pt32-100 (left) and AN-TiN60/Pt32-50 (right). Electrolyte: 0.5 M H_2SO_4. Scan rate: 150 mV/s 96
Figure 51: 110th CV scan comparison for AN-TiN60/Pt32-100 and AN-TiN60/Pt32-50 96
Figure 52: ECSA evolution during cycling for AN-TiN60/Pt32-50 (left) and AN-TiN60/Pt32-100 (right). Error bars are included. 97
Figure 53: ECSA comparison for AN-TiN60/Pt32-50 and AN-TiN60/Pt32-100 97
Figure 54: HR-SEM top view images of pristine AN-TiN60/Pt32-50 catalyst at different magnifications 102
Figure 55: XRD spectrum of the pristine AN-TiN60/Pt32-50 catalyst 103
Figure 56: CV plots for the two AN-TiN60/Pt32-50 catalysts. Electrolyte: 0.5 M H_2SO_4 (left), 0.5 M H_2SO_4 + 1 M CH_3OH (right). Scan rate: 150 mv/s 104
Figure 57: Pristine AN-TiN60/Pt32-50 ECSA evolution. Error bars due to faradaic efficiency of electrodeposition are included 105

Figure 58: ΔE and I_{ratio} for the pristine AN-TiN60/Pt32-50#2 catalyst (left) and CV plot in 0.5 M H_2SO_4 + 1 M CH_3OH (right). Scan rate: 50 mV/s 105
Figure 59: XRD spectra for AN-TiN60/Pt32-50#1 (left) and AN-TiN60/Pt32-50#2 (right) 106
Figure 60: CV plots for AN-TiN60/Pt32-50#2. Electrolyte: 0.5 M H_2SO_4. Scan rate: 150 mV/s..... 107
Figure 61 LEFT: Comparison for the last CV scan for AN-TiN60/Pt32-50#1 and #2. RIGHT: ECSA evolution of AN-TiN60/Pt32-50#1 and #2..... 108
Figure 62 LEFT: XRD spectrum for cycled AN-TiN60/Pt32-50#2. RIGHT: XRD spectra comparison for AN-TiN60/Pt32-50#2, before and after the second CV test in 0.5 M H_2SO_4..... 109
Figure 63 LEFT: CV plot for the cycled AN-TiN60/Pt32-50#2. RIGHT: CV comparison between pristine and cycled AN-TiN60/Pt32-50#2. Electrolyte: 0.5 M H_2SO_4 + 1 M CH_3OH. Scan rate: 50 mV/s. 110
Figure 64: ΔE and I_{ratio} for the cycled AN-TiN60/Pt32-50#2 catalyst..... 110

Appendix

A.1 - Instruments & Materials

Pulsed Laser Deposition is performed with a pulsed KrF excimer laser, Coherent COMPexPro 205 F. For DC sputtering, a Mantis CUSP DC magnetron sputter is employed.

X-Ray Diffraction analysis is carried out with a Bruker D8 Advance system. All electrochemical measurements are performed with a Metrohm-Autolab Multi Autolab M204: the uncertainty for current measurements is the 0,2% of the recorded value, with a range of $\pm$1,2 A, while for the voltage measurement the uncertainty is composed of a fixed term of 2 mV, and a variable term equal to 0,2% of the recorded value, with a range of $\pm$10 V.

As substrates, FTO glass (Dyesol, 15 Ω/sq) and glassy carbon (Tokai Carbon) are used.

All chemicals are purchased from Sigma-Aldrich: H_2SO_4 (ACS Reagent 95,0%-98,0%), CH_3OH (ACS reagent, reag. ISO, reag. Ph. Eur., ≥99,8%), $H_2PtCl_6{\cdot}6H_2O$ (ACS reagent, ≥37.50% Pt basis)

For electrochemical measurements, a Pt wire has been employed as counter electrode, while an Ag/AgCl electrode has been employed as reference electrode.

A.2 - ECSA Calculation Method

In section 2.2.4, the following expression for the ECSA calculation is shown:

$$ECSA = \frac{Q_H}{q_h \cdot m_{Pt}}$$

Operatively, the calculation of the value is performed through the following formula:

$$ECSA = \frac{\int_{0.05\,V}^{0.40\,V} i - i_{double\ layer}\, dV}{m_{Pt} \cdot q_h \cdot Scan\ Rate}$$

As already stated in the corresponding section, q_h =2,1·10^{-4} C/cm^2, while the platinum loading mPt is calculated with the formula already discussed in section 2.1.6. and here reported:

$$m_{deposited} = \frac{Q_{deposited}}{F \cdot EPI} \cdot MM_{metal} \cdot \eta_{faradaic}$$

A.3 - Lattice Strain Calculation Method

The procedure for the Pt lattice strain calculation is articulated as follows, according to [54], [55]:

I. The observed width at half height for the Pt peaks of the recorded XRD spectra, named β_{ob}, are calculated;

II. β_{ob} is composed of two terms: $\beta_{ob}=\beta_{in}+\beta_{re}$. β_{in} represents the broadening of the XRD peak due to the instrument, and is considered negligible for the analysis carried out in this work. The other term, β_{re}, on the other hand is the broadening due to the particle size and the strain;

III. β_{re} is also composed of two terms, one connected to the real particle size and the other to the strain. This relationship is expressed by the following equation:

$$\beta_{re} = \beta_{particle} + \beta_{strain} = \beta_{particle} + \eta \, tan \, \theta$$

Where η is the lattice strain (in %);

IV. Introducing the Scherrer equation, $\beta_{particle}$ is expressed as:

$$\beta_{particle} = \frac{K \, \lambda}{D_{grain} \, cos \, \theta} \rightarrow \quad \beta_{re} \, cos \, \theta = \frac{K \, \lambda}{D_{grain}} + sin \, \theta$$

Where K is the dimensionless crystallite shape factor, a costant whose value ranges from 0,84 to 1: in this work it is considered k=0,9. λ is, instead, the wavelength of the incident x-ray radiation;

V. Finally, βre cos θ is plotted against sin θ: the slope of curve is the lattice strain η.

Legend and Acronyms

The various samples analyzed in this thesis have been named according to the following method:

- A suffix **AD** or **AN**, to indicate if the TiN support is, respectively, as deposited or annealed;
- The formula TiN is followed by a **number**, indicated the deposition pressure of N_2 used for fabricating the support (in Pa);
- For the support+catalyst material, the Pt formula is followed by **two numbers**, separated by a dash: the first number indicates the total deposited Pt charge (in C/cm^2), while the second number indicates the current pulse on-time during electrodeposition (in ms).

Therefore, a sample named AN-TiN60/Pt16-100 indicates an annealed TiN support, deposited with a nitrogen pressure of 60 Pa, and loaded with a total charge of 16 C/cm^2 Pt, electrodeposited with a current on-time of 100 ms.

The following acronyms have been used, and their meaning is shown below:

- CV: Cyclic Voltammetry;
- DMFC: Direct Methanol Fuel Cell;
- ECSA: Electro-Chemical Surface Area;
- LSV: Linear Sweep Voltammetry;
- MOR: Methanol Oxidation Reaction;
- PEMFC: Polymer Electrolyte Membrane Fuel Cell;
- PLD: Pulsed Laser Deposition;
- SEM: Scanning Electron Microscope;
- XRD: X-Ray Diffraction.

References

[1] A. Halme, J. Selkainaho, T. Noponen, A. Kohonen, «An alternative concept for DMFC - Combined electrolyzer and H2 PEMFC,» *International Journal of Hydrogen Energy,* vol. 41, n. 4, pp. 2154-2164, 2016.

[2] A. J. Bard and L. R. Faulkner, Electrochemical Methods: Fundamentals and Applications, John Wiley & Sons, Inc., 2001.

[3] Z.-G. Shao, F. Zhu, W.-F. Lin, P. Christensen, H. Zhang, «PtRu/Ti anodes with carying Pt:Ru ratio prepared by electrodeposition for the direct methanol fuel cell,» *Physical Chemistry Chemical Physics,* vol. 8, pp. 2720-2726, 2006.

[4] A. Chen and P. Holt-Hindle, "Platinum-Based Nanostructured Materials: Synthesis, Properties, and Applications," *Chemical Reviews,* vol. 110, no. 6, pp. 3767-3804, 2010.

[5] T. Iwasita, «Electrocatalysis of methanol oxidation,» *Electrochimica Acta,* vol. 47, pp. 3663-3674, 2002.

[6] W. Lin, M. Zei, M. Eiswirth, G. Ertl, T. Iwasita, W. Vielstich, «Electrocatalytic Activity of Ru-Modified Pt(111) Electrodes toward CO Oxidation,» *The Journal of Physical Chemistry B,* vol. 1033, n. 33, pp. 6968-6977, 1999.

[7] H. Liu, C. Song, L. Zhang, J. Zhang, H. Wang, D. P. Wilkinson, «A review of anode catalysis in the direct methanol fuel cell,» *Journal of Power Sources,* vol. 155, n. 2, pp. 95-110, 2006.

[8] K.-W. Park, J.-H. Choi, B.-K. Kwon, S.-A. Lee, Y.-E. Sung, H.-Y. Ha, S.-A. Hong, H. Kim, A. Wieckowski, «Chemical and Electronic Effects of Ni in Pt/Ni and Pt/Ru/Ni Alloy Nanoparticles in Methanol Electrooxidation,» *The Journal of Physical Chemistry B,* vol. 106, n. 8, pp. 1869-1877, 2002.

[9] F. Cheng, Y. Su, J. Liang, Z. Tao, J. Chen, «MnO2-Based Nanostructures as catalysts for electrochemical oxygen reduction in alkaline media,» *Chemistry of Materials,* vol. 22, n. 3, pp. 898-905, 2010.

[10] H. Xu, X. Hou, «Synergistic effect of CeO2 modified Pt/C electrocatalysts on the performance of PEM fuel cells,» *International Journal of Hydrogen Energy,* vol. 32, n. 17, pp. 4397-4401, 2007.

[11] C. Xu, R. Zeng, P. K. Shen, Z. Wei, «Synergistic effect of CeO2 modified Pt/C catalysts on the alcohols oxidation,» *Electrochimica Acta,* vol. 51, n. 6, pp. 1031-1035, 2005.

[12] J. E. Benson, H. Kohn, M. Boudart, «On the reduction of tungsten trioxide accelerated by platinum and water,» *Journal of Catalysis,* vol. 5, n. 2, pp. 307-313, 1966.

[13] P. Shen, K. Chen, A. C. Tseung, «Co-deposited Pt-WO3 electrodes. Part 1 - Methanol oxidation and in situ FTIR studies,» *Journal of the Chemical Society, Faraday Transactions,* vol. 90, pp. 3089-3096, 1994.

[14] V. Baglio, A. Di Blasi, A. Aricò, V. Antonucci, P. Antonucci, F. Serraino Fiory, S. Licoccia, E. Traversa, «Influence of TiO2 nanometric filler on the behaviour of a composite membrane for applications in direct methanol fuel cells,» *Journal of New Materials for Electrochemical Systems,* vol. 7, pp. 275-280, 2004.

[15] C.-C. Yang, W.-C. Chien and Y. J. Li, "Direct methanol fuel cell based on poly(vinyl alcohol)/titanium oxide nanotubes/poly(styrene sulfonic acid) (PVA/nt-TiO2/PSSA) composite polymer membrane," *Jounral of Power Sources,* vol. 195, no. 11, pp. 3407-3415, 2010.

[16] P. Kolla, A. Smirnova, «Methanol oxidation on hybrid catalysts: PtRu/C nanostructures promoted with cerium and titanium oxides,» *International Journal of Hydrogen Energy,* vol. 38, n. 35, pp. 15152-15159, 2013.

[17] K. Drew, G. Girishkumar, K. Vinodgopal, P. V. Kamat, «Boosting Fuel Cell Performance with a Semiconductor Photocatalyst: TiO2/Pt−Ru Hybrid Catalyst for Methanol Oxidation,» *The Journal of Physical Chemistry B,* vol. 109, n. 24, pp. 11851-11857, 2005.

[18] D. V. Arulmani, J. I. Eastcott, S. G. Mavilla, E. B. Easton, «Photo-enhanced activity of Pt and Pt-Ru catalysts towards the electro-oxidation of methanol,» *Journal of Power Sources,* vol. 247, pp. 890-895, 2014.

[19] J. H. Park, S. Kim, A. J. Bard, «Novel Carbon-Doped TiO2 Nanotube Arrays with high Aspect Ratios for Efficient Solar Water Splitting,» *Nano Letters,* vol. 6, n. 1, pp. 24-28, 2006.

[20] C. Xu, Y. Shaban, W. Ingler Jr., S. Khan, «Nanotube enhanced photoresponse of carbon modified (CM)-n-TiO2 for efficient water splitting,» *Solar Energy Materials and Solar Cells,* vol. 91, n. 10, pp. 938-943, 2007.

[21] X. Chen, P. Yu e S. Mao, «Increasing Solar Absorption for Photocatalysis with Black Hydrogenated Titanium Dioxide Nanocrystals,» *Science,* vol. 331, n. 6018, pp. 746-750, 2011.

[22] A.-M. Alexander, J. Hargreaves, «Alternative catalytic materials: carbides, nitrides, phosphides and amorphous boron alloys,» *Chemical Society Reviews,* vol. 39, pp. 4388-4401, 2010.

[23] B. Avasarala, P. Haldar, «Electrochemical oxidation behavior of titanium nitride based electrocatalysts under PEM fuel cell conditions,» *Electrochimica Acta,* vol. 55, n. 28, pp. 9024-9034, 2010.

[24] M. Musthafa, S. Sampath, «High performance platinized titanium nitride catalyst for methanol oxidation,» *Chemical Communications,* n. 1, pp. 67-69, 2008.

[25] M. Yang, Z. Cui, F. DiSalvo, «Mesoporous titanium nitride supported Pt nanoparticles as high performance catalysts for methanol electrooxidation,» *Physical Chemistry Chemical Physics,* vol. 15, pp. 1088-1092, 2013.

[26] M. Ottakam Thotiyl, T. Ravikumar, S. Sampath, «Platinum particles supported on titanium nitride: an efficient electrode material for the oxidation of methanol in alkaline media,» *Journal of Materials Chemistry,* vol. 20, pp. 10643-10651, 2010.

[27] K. Kakinuma, Y. Wakasugi, M. Uchida, T. Kamino, H. Uchida, S. Deki, M. Watanabe, «Preparation of titanium nitride-supported platinum catalysts with well controlled morphology and their properties relevant to polymer electrolyte fuel cells,» *Electrochimica Acta,* vol. 77, pp. 279-284, 2012.

[28] L. Passoni, «Titanium dioxide hierarchical nanostructures for photonic applications», PhD dissertation, Politecnico di Milano, 2015.

[29] H.-U. Krebs, M. Weisheit, J. Faupel, E. Süske, T. Scharf, C. Fuhse, M. Störmer, K. Sturm, M. Seibt, H. Kijewski, D. Nelke, E. Panchenko, M. Bubak, «Pulsed Laser Deposition (PLD) -- A Versatile Thin Film Technique,» in *Advances in Solid State Physics*, Springer Berlin Heidelberg, 2003, pp. 505-518.

[30] J. Schou, «Physical aspects of the pulsed laser deposition technique: The stoichiometric transfer of material from target to film,» *Applied Surface Science,* vol. 255, n. 10, pp. 5191-5198, 2009.

[31] D. Lowndes, D. Geohegan, A. Puretzky, D. Norton, C. Rouleau, «Synthesis of Novel Thin-Film Materials by Pulsed Laser Deposition,» *Science,* vol. 273, n. 5277, pp. 898-903, 1996.

[32] A. Baserga, V. Russo, F. Di Fonzo, A. Bailini, D. Cattaneo, C. Casari, A. Li Bassi, «Nanostructured tungsten oxide with controlled properties: Synthesis and Raman characterization,» *Thin Solid Films,* vol. 515, n. 16, pp. 6465-6469, 2007.

[33] A. L. Gobbi, P. Nascente, «D.C. Sputtering,» in *Encyclopedia of Tribology*, Springer US, 2013, pp. 699-706.

[34] M. Chandrasekar, M. Pushpavanam, «Pulse and pulse reverse plating—Conceptual, advantages and applications,» *Electrochimica Acta,* vol. 53, n. 8, pp. 3313-3322, 2008.

[35] Y.-C. Hsieh, Y.-J. Lu, P.-W. Wu, Y.-M. Chang, Y.-F. Chiu, «Galvanostatic Pulse Plating of PtRu Nanoparticles for Direct Methanol Fuel Cells,» *ECS Transactions,* vol. 16, n. 2, pp. 473-481, 2008.

[36] X.-Z. Yuan, C. Song, H. Wang, J. Zhang, Electrochemical Impedance Spectroscopy in PEM Fuel Cells - Fundamentals and Applications, Spinger-Verlag London Limited, 2010.

[37] J. O. Bockris, A. K. N. Reddy, M. Gamboa-Aldeco, Modern Electrochemistry 2A - Fundamentals of Electrodics, New York: Kluwer Academic/Plenum Publishers, 2000.

[38] S. Srinivasan, Fuel Cells - From Fundamentals to Applications, Springer US, 2006.

[39] A. Monshi, M. R. Foroughi, M. R. Monshi, «Modified Scherrer Equation to Estimate More Accurately Nano-Crystallite Size using XRD,» *World Journal of Nano Science and Engineering,* vol. 2, pp. 154-160, 2012.

[40] L. Passoni, L. Criant, F. Fumagalli, F. Scotognella, G. Lanzani, F. Di Fonzo, «Self-Assembled Hierarchical Nanostructures for High-Efficiency Porous Photonic Crystals,» *ACS NANO,* vol. 8, n. 12, pp. 12167-12174, 2014.

[41] H. Du, Y. Xie, C. Xia, W. Wang, F. Tian, «Electrochemical capacitance of polypyrrole-titanium nitride and polypyrrole-titania nanotube hybrids,» *New Journal of Chemistry,* vol. 38, pp. 1284-1293, 2014.

[42] J. Yoo, H. Yoo, H. K. H. Jung, S. Bang, J. Choi, H. Suh, J.-H. Lee, J.-G. Kim, N.-H. Hur, «Titanium oxynitride microspheres with the rock-salt structure for use as visibile-light photocatalysts,» *Journal of Materials Chemistry A,* vol. 4, pp. 869-876, 2016.

[43] L. Passoni, G. Bonvini, A. Luzio, A. Facibeni, C. Bottani, F. Di Fonzo, «Multiscale Effect of Hierarchical Self-Assembled Nanostructures on Superhydrophobic Surface,» *Langmuir,* vol. 30, n. 45, pp. 13581-13587, 2014.

[44] J. Tang, K. Jensen, M. Waje, W. Li, P. Larsen, K. Pauley, Z. Chen, P. Ramesh, M. Itkis, Y. Yan, R. Haddon, «High Performance Hydrogen Fuel Cells with Ultralow Pt loading Carbon Nanotube Thin Film Catalysts,» *The Journal of Physical Chemistry C,* vol. 111, n. 48, pp. 17901-17904, 2007.

[45] K. Yasuda, A. Taniguchi, T. Akita, T. Ioroi, Z. Siroma, «Platinum dissolution and deposition in the polymer electrolyte membrane of a PEM fuel cell as studied by potential cycling,» *Physical Chemistry Chemical Physics,* vol. 8, pp. 746-752, 2005.

[46] H. Villullas, F. Mattos-Costa, L. Bulhoes, «Electrochemical Oxidation of Methanol on Pt Nanoparticles Dispersed on RuO2,» *The Journal of Physical Chemistry B,* vol. 108, pp. 12898-12903, 2004.

[47] Y. Li, W. Gao, L. Ci, C. Wang, P. Ajayan, «Catalytic performance of Pt nanoparticles on reduced graphene oxide for methanol electro-oxidation,» *Carbon,* vol. 48, n. 4, pp. 1124-1130, 2010.

[48] V. Raghuveer, A. Manthiram, «Mesoporous Carbons with Controlled Porosity as an Electrocatalytic Support for Methanol Oxidation,» *Journal of the Electrochemical Society,* vol. 152, n. 8, pp. A1504-A1510, 2005.

[49] R. Manoharan, J. Goodenough, «Methanol Oxidation in Acid on Ordered NiTi,» *Journal of Materials Chemistry,* vol. 2, n. 8, pp. 875-887, 1992.

[50] A. Hofstead-Duffy, D.-J. Chen, S.-G. Sun, Y.-J. Tong, «Origin of the current peak of negative scan in the cyclic voltammetry of methanol electro-oxidation on Pt-based electrocatalysts: a

revisit to the current ratio criterion,» *Journal of Materials Chemistry,* vol. 22, pp. 5205-5208, 2012.

[51] D. Y. Chung, K.-J. Lee, Y.-E. Sung, «Methanol electro-oxidation on Pt surface: Revisiting the Cyclic Voltammetry Interpretation,» *The Journal of Physical Chemistry C,* vol. 120, n. 17, pp. 9028-9035, 2016.

[52] T. Deivara, J. Lee, «Preparation of carbon-supported PtRu nanoparticles for direct methanol fuel cell applications - a comparative study,» *Journal of Power Sources,* vol. 142, pp. 43-49, 2005.

[53] M. Yang, Z. Cui, F. DiSalvo, «Mesoporous titanium nitride supported Pt nanoparticles as high performance catalysts for methanol electrooxidation,» *Physical Chemistry Chemical Physics,* vol. 15, pp. 1088-1092, 2012.

[54] C. Suryanarayana, M. Norton, in *X-Ray Diffraction - A Practical Approach*, New York, Plenum Press, 1998, pp. 207-221.

[55] B. Cullity, S. Stock, in *Elements of X-ray Diffraction, 3rd Edition*, Prentice-Hall, 2001, pp. 167-176;385-402;697.